HARVARD UNIVERSITY
Graduate School of Arts and Sciences

DISSERTATION ACCEPTANCE CERTIFICATE

The undersigned, appointed by the

Department of Physics

have examined a dissertation entitled

Progress Toward a Single-Electron Qubit in an Optimized Planar Penning Trap

presented by Melissa Ann Wessels

candidate for the degree of Doctor of Philosophy and hereby certify that it is worthy of acceptance.

Signature _____

Typed name: Professor Gerald Gabrielse, Chair

Signature _____

Typed name: Professor Masahiro Morii

Signature _____

Typed name: Professor Isaac Silvera

Date: July 25, 2019

Progress Toward a Single-Electron Qubit in an Optimized Planar Penning Trap

A thesis presented

by

Melissa Ann Wessels

to

The Department of Physics

in partial fulfillment of the requirements

for the degree of

Doctor of Philosophy

in the subject of

Physics

Harvard University

Cambridge, Massachusetts

July 2019

Thesis advisor

Gerald Gabrielse

Author

Melissa Ann Wessels

Progress Toward a Single-Electron Qubit in an Optimized Planar Penning Trap

Abstract

This thesis summarizes two ongoing experiments. The primary focus is on progress towards realizing a single-electron qubit in a scalable, planar Penning trap geometry. Two simulataneously trapped electrons were observed, significant progress over previous attempts by others. The second topic is a review of work leading up to and following our laboratory's first production of cold antihydrogen atoms in 2002.

Contents

List of Figures

List of Tables

Papers and Publications

1. *Aperture Method to Determine the Density and Geometry of Anti-Particle Plasmas*
   P. Oxley, N.S. Bowden, R. Parrott, A. Speck, C. Storry, J.N. Tan, M. Wessels, G. Gabrielse, D. Grzonka, W. Oelert, G. Schepers, T. Sefzick, J. Walz, H. Pittner, T.W. Hänsch, E.A. Hessels, Phys. Lett. B **595**, 60 (2004).

2. *Observations of Cold Antihydrogen*
   J.N. Tan, N.S. Bowden, G. Gabrielse, P. Oxley, A. Speck, C.H. Storry, M. Wessels, D. Grzonka, W. Oelert, G. Schepers, T. Sefzick, J. Walz, H. Pittner, T.W. Hänsch, E.A. Hessels, Nuclear Instruments and Methods in Physics Research B **214**, 22 (2004).

3. *Driven Production of Cold Antihydrogen and the First Measured Distribution of Antihydrogen States*
   G. Gabrielse, N.S. Bowden, P. Oxley, A. Speck, C.H. Storry, J.N. Tan, M. Wessels, D. Grzonka, W. Oelert, G. Schepers, T. Sefzick, J. Walz, H. Pittner, T.W. Hänsch, E.A. Hessels, Phys. Rev. Lett. **89**, 233401 (2002).

4. *Background-Free Observation of Cold Antihydrogen and a Field-Ionization Analysis of Its States*
   G. Gabrielse, N.S. Bowden, P. Oxley, A. Speck, C.H. Storry, J.N. Tan, M. Wessels, D. Grzonka, W. Oelert, G. Schepers, T. Sefzick, J. Walz, H. Pittner, T.W. Hänsch, E.A. Hessels, Phys. Rev. Lett.**89**, 213401 (2002).

5. *Stacking of Cold Antiprotons*
   G. Gabrielse, N.S. Bowden, P. Oxley, A. Speck, C.H. Storry, J.N. Tan, M. Wessels, D. Grzonka, W. Oelert, G. Schepers, T. Sefzick, J. Walz, H. Pittner, T.W. Hänsch, E.A. Hessels, Phys. Lett. B **548**, 140 (2002).

6. *Cold Antihydrogen and CPT*
   G. Gabrielse, J.N. Tan, N.S. Bowden, P. Oxley, C.H. Storry, M. Wessels, A. Speck, J. Estrada, P. Yesley, D. Grzonka, W. Oelert, G. Schepers, T. Sefzick, J. Walz, In *Proceedings of the Second Meeting on CPT and Lorentz Symmetry*, edited by V. Alan Kostelecky, World Scientific Publishing Co Pte. Ltd., Singapore, 225-234 (2002).

7. *Cold Antimatter Plasmas, and Aspirations for Cold Antihydrogen*
   G. Gabrielse, J.N. Tan, N.S. Bowden, P. Oxley, C.H. Storry, M. Wessels, A. Speck, J. Estrada, P. Yesley, T. Squires, D. Grzonka, W. Oelert, G. Schepers, T. Sefzick, J. Walz, In *Non-Neutral Plasma Physics IV* (AIP Conference Proceedings, volume 606), edited by F. Anderegg, L. Schweikhard, C.F. Driscoll, American Institute of Physics, Melville, NY, 51-62 (2002).

8. *First Positron Cooling of Antiprotons*
   G. Gabrielse, J. Estrada, J.N. Tan, P. Yesley, N.S. Bowden, P. Oxley, T. Roach, C.H. Storry, M. Wessels, J. Tan, D. Grzonka, W. Oelert, G. Schepers, T. Sefzick, W. Bruenlich, M. Carngelli, H. Fuhrmann, R. King, R. Ursin, H. Zmeskal, H. Kalinowsky, C. Wesdorp, Phys. Lett. B **507**, 1 (2001).

Acknowledgments

I am grateful to Professor Gerald Gabrielse for giving me the opportunity to do this interesting and exciting work, and for his guidance along the way. I am also grateful to have had the opportunity to serve as a teaching fellow for his course "Reality Physics" and to have learned from his example as an educator.

I would like to thank Professors Masahiro Morii and Isaac Silvera for serving on my dissertation committee and for their supportive and helpful conversations during this work.

I would like to thank the students and post-doctoral fellow with whom I worked closely on the planar trap experiment for their generosity, insight, and comaraderie, especially Elise Novitski, Ron Alexander, Sam Fayer, Tom Myers, and Xing Fan. For similar comaradie and support during my work on the antihydrogen experiment, I would like to thank Paul Oxley, Nathaniel Bowden, John Estrada, Peter Yesley, and Andrew Speck. I also benefited from daily conversations with graduate students in the larger laboratory community, namely Mason Marshall, Cris Panda, Andra Ionescu, Geev Nahal, Cole Meisenhelder, and Daniel Ang, as well as Brian Odom, Brian D'Urso, and Tanya Zelevinsky.

I am grateful to the physics department staff for their assistance and support. I am especially grateful to Stan Cotreau for his guidance and good cheer in the machine shop, and to Jim MacArthur for many helpful conversations in the electronic instruments design lab. I also want to recognize the support of our administrative assistants, Jan Ragusa and Patricia McGarry. I would like to extend a special thanks to Jacob Barandes and Lisa Cacciabaudo for their kind and steadfast support.

I am thankful to Tracey Newman for the caring support I have received in the

department of financial aid. I am grateful to the Mark and Catherine Winkler Scholarship Fund and their commitment to student-parents; their support made it possible for me to complete this work.

Finally, I would like to thank my friends and family–with a special thanks to my son, William–for their always-present love, support, good humor, and understanding.

Chapter 1

Introduction

1.1 Overview

This thesis describes experimental efforts on two ongoing experiments. The primary focus is on recent progress toward realizing a single-electron qubit in a scalable, planar Penning trap geometry. This work was completed after returning from an interruption in my Ph.D. studies. The second topic is a review of earlier work performed during the time leading up to and following our laboratory's first production of cold antihydrogen atoms in 2002.

The substantial success in our laboratory with trapping, detecting, and manipulating single electrons in cylindrical Penning traps motivated the first explorations in the literature of a one-electron qubit in a Penning trap. Achievements, such as quantum-nondemolition (QND) measurements of one-quantum transitions, ground state initialization with the suppression of thermally-driven spontaneous transitions, and long trapping and coherence times [4], suggested that a Penning trap qubit mer-

its exploration. However, the geometry of the cylindrical Penning trap that has met with so much success in our laboratory fails to meet the quantum computing hardware requirement of scalability. If a practical Penning trap qubit is to be achieved, a new Penning trap geometry is in order.

As a solution, a two-dimensional planar Penning trap was proposed in the literature [1, 5, 6], with the future vision of an array of planar Penning traps capable of miniaturization fabricated on the same chip. Early efforts in Mainz and Ulm, Germany to build and demonstrate such a trap failed to produce an adequately harmonic trapping potential. Their claim was that a "genuinely harmonic" potential cannot be achieved with any planar Penning trap design due to a lack of reflection symmetry, and that it is thus "impossible" to observe a single electron in a planar Penning trap [7].

Theoretical studies in our laboratory prompted by this pessimism suggested otherwise [3, 8]. Decades of experience in Penning trap design was brought to bear with results that encourage optimism. Both an optimized planar Penning trap design and an anharmonicity compensaton scheme were proposed to contend with the anharmonicities that troubled efforts by others. A planar Penning trap was constructed in our laboratory according to the new optimized design [9]. The trapping of many-electron clouds was demonstrated as well as the anharmonicity tuning of the trap.

This thesis presents improvements to the apparatus in an effort to realize one trapped electron. The planar electrodes are resurfaced by polishing and gold electroplating to prevent the rapid oxidation observed during previous efforts. A single electron in a planar trap is confined within 2 mm of the planar surface and subject

to instabilities caused by possible surface patch potential structure. Furthermore, the detection electronics are rebuilt and a new design described for a second-stage cryogenic amplifier to improve detection stability and sensitivity. Data are presented, showing that two simulatneously trapped electrons are observed, significant progress over previous attempts at Mainz and Ulm.

This chapter discusses the larger motivations for a planar Penning trap qubit and the merits that drive its pursuit. Chapter 2 discusses Penning trap design and the innovations in our laboratory that have met with much success. A summary is presented of the design of an optimized planar Penning trap geometry and the anharmonicity compensation scheme invented in our laboratory to confront the difficulties the group at Ulm claimed to be insurmountable. Chapter 3 describes the fabrication of our optimized planar Penning trap and its supporting apparatus. New modifications to the trap electrodes and the detection electronics to improve trap stability and detection sensitivity are reported here for the first time. Chapter 4 describes the operation of the optimized planar Penning trap, and Chapter 5 reports the first data describing the measured axial linewidths of small clouds of electrons confined in our optimized trap and shows that the linewidths are quantized by the single-electron linewidth, with the smallest confined cloud being that of 2 electrons. This result, substantially fewer than the 100-1000 electrons trapped at Mainz and Ulm, demonstrates significant progress.

In Chapter 6, the design and development of a second-generation ATRAP apparatus for the production and trapping of cold antihydrogen atoms is presented, work completed during the years 1999 to 2003. The goal of the ATRAP experiment, operated at the Antiproton Decelerator (AD) at the European high-energy particle physics

laboratory CERN, is to test physics' fundamental theories by conducting precision measurements with trapped antihydrogen atoms. Precision spectroscopy of trapped antihydrogen atoms could yield the most precise test of CPT symmetry in a lepton-baryon system [10]. Gravitation studies with cold trapped antihydrogen atoms have also been proposed [11].

With the first-generation ATRAP apparatus, our group successfully demonstrated the capture [12] and positron cooling of 5.3 MeV antiprotons [13] and the production of cold antihydrogen atoms [14], reporting the first measured distribution of antihydrogen states [15]. In support of these efforts, I undertook the development and fabrication of new detection electronics. Based on new designs [16], the HEMT-based first and second-stage cryogenic amplifiers provided for greater stability and detection sensitivity. Additionally, I built electronics for high-speed voltage switching to enable antiproton capture. I also fabricated new high-stability voltage supplies, developed with Jim MacArthur, for Penning trap electrode biasing.

In the wake of the achievements of this first-generation experiment, I undertook the design and development of a new apparatus that would allow for new capabilities, including increased antihydrogen production, trapping of the neutral antiatoms, and the ability for laser-access for spectroscopy studies. Chapter 6 describes this work, presenting apparatus design innovations and the goals that motivated them.

1.2 Motivation

Since quantum computing was first proposed in the early 1980's [17–20], it has garnered much interest and research attention due to its potential for solving classically

intractable problems. A quantum computer would be able to factor large integers exponentially faster than the best classical algorithms [21], with far-reaching implications for encryption and cybersecurity. A quantum processor would also make the simulation of quantum systems possible [18, 22], in all their considerable complexity, enabling significant advances in knowledge and technology in the fields of physics, chemistry, and biology. Furthermore, tools developed for quantum computing would be directly relevant to the emerging fields of quantum communication, quantum cryptography, and quantum metrology. As an additional incentive, the classical computer industry is on course to reach its limit with the miniaturization of classical systems in the next decades, and any further advancement would require new quantum technology.

A quantum computer is built from a quantum bit, or so-called qubit, the two-state quantum counterpart to the classical bit. The vastly greater capacity of the quantum computer is a result of the quantum mechanical properties of superposition and entanglement. A two-state quantum system is capable of a continuum of states, rather than just two, where all possible states are represented by a linear superposition of the two possible quantum states: $a\,|0\rangle + b\,|1\rangle$. Coupling multiple qubits allows for entangled states, increasing the state space exponentially. Two-state quantum systems used for qubit realization include photon polarization, electron or nuclear spin, and energy level transitions in a real or artificial atom or molecule. The physical implementation of a quantum computer, building the quantum hardware, begins with the realization of a practical qubit and presents significant challenges.

1.2.1 Quantum Computing Hardware

Many schemes have been suggested for realizing the physical implementation of a many-qubit quantum computer. The requirements for such an implementation were first outlined by DiVinzenco in his often-cited work [23].

Requirements and DiVinzenco's Criteria

DiVinzenco outlines five requirements for a quantum computing hardware scheme [23]. (1) First, a "scalable physical system of well-characterized qubits" is required. An ensemble of qubits, each a quantum two-level system as described above, is needed along with the ability to couple each qubit to its neighbors. The system should be "scalable" in the sense that the ensemble can grow in number such that the possible state space increases exponentially without an equivalent cost in resources. Furthermore, the qubits should be "well-characterized" such that their states can be accurately measured.

(2) The second requirement is the ability "to initialize the state of the qubits to a simple fiducial state, such as $|000...\rangle$". Any standard computing process requires that the system be initialized at the start. For a quantum system this is typically achieved either by cooling the system to its ground state, or by carrying out a measurement that prepares the system into a desired state.

(3) The third requirement for realizing a quantum hardware scheme is a qubit with a long quantum state coherence time relative to the combined gate operation and readout time. This is perhaps the most critical requirement: that the quantum system be isolated from decoherence mechanisms in the larger environment, at least

for the length of time required for the computer to carry out its desired operation and measure its result. Some amount of decoherence may be tolerable given quantum error correction (QEC) protocols.

(4) DiVinzenco's fourth requirement is a qubit ensemble capable of carrying out a universal set of quantum logic gates. A universal logic gate is one from which all other logic gates may be formed, each requiring two to three coupled qubits. To carry out the sequence of transformations that specify a quantum algoithm, interactions between qubits must be facilitated and switchable.

(5) The fifth and final requirement outlined by DiVinzenco is the capability of a "qubit-specific measurement". An effective measurement procedure is needed. Strong coupling to the qubit for the sake of measurement can lead to decoherence, whereas weak coupling makes it difficult to determine the qubit state reliably. The measurement procedure's contribution to decoherence and the quality of readout both must be optimized. The ideal measurement would be a quantum non-demolition (QND) one, where the measurement reports the outcome state of a qubit and then leaves the qubit in the outcome state, meeting the initialization requirement for the next operation.

Current Schemes

A number of different physical implementations of a quantum processor that meet various of these requirements have been proposed and studied [22, 24, 25]. Some current qubit schemes under study are photons in waveguide quantum circuits [26], trapped neutral atoms in optical lattices [27], ions in linear traps [28], liquid-state

NMR [29], superconducting circuits [30,31], electron spin qubits in quantum dots [32], and nitrogen-vacancy centers in diamond [33].

Significant strides have been made in just the past decade. Proof-of-principle experiments specific to the problem of quantum simulation have already been realized, demonstrating quantum simulators of tens of coupled qubits with arrays of strongly interacting atoms [34] and with trapped ions [35,36]. However, significant challenges remain across the prospective schemes pertaining to individual qubit control and measurement, minimizing decoherence, and scaling to large numbers of coupled qubits and many-gate operations. A universal quantum computer, one that can solve many different types of problems, is still believed to be decades away from realization.

Given the significant number of schemes still in contention, it is reasonable to consider that there are existing technologies that have not yet been tapped to solve the challenges that remain.

1.2.2 Penning Traps and a One-Electron Qubit

The first explorations in the literature of a one-electron qubit in a Penning trap [37–41] were motivated by the substantial success in our laboratory with resolving one-quantum spin and cyclotron transitions in a single electron in a cylindrical Penning trap [4, 42]. Indeed, our laboratory's achievements, when matched against the necessary criteria for a quantum computing hardware scheme, would suggest that a Penning trap qubit merits exploration.

An electron in a Penning trap is a well-characterized system that presents two possible quantum two-level transition states for building a qubit: a spin-state tran-

sition and a transition between the ground and first excited cyclotron states. The energy level structure is shown in the diagram of Fig. 1.1. The three frequencies, ν_z, ν_m, and ν_c, describe the electron's spatial motion. In the magnetic field of the Penning trap, the electron spin may have one of two orientations, spin up or spin down, giving rise to spin states separated by energy $h\nu_s$, where $\nu_s = g\nu_c/2$.

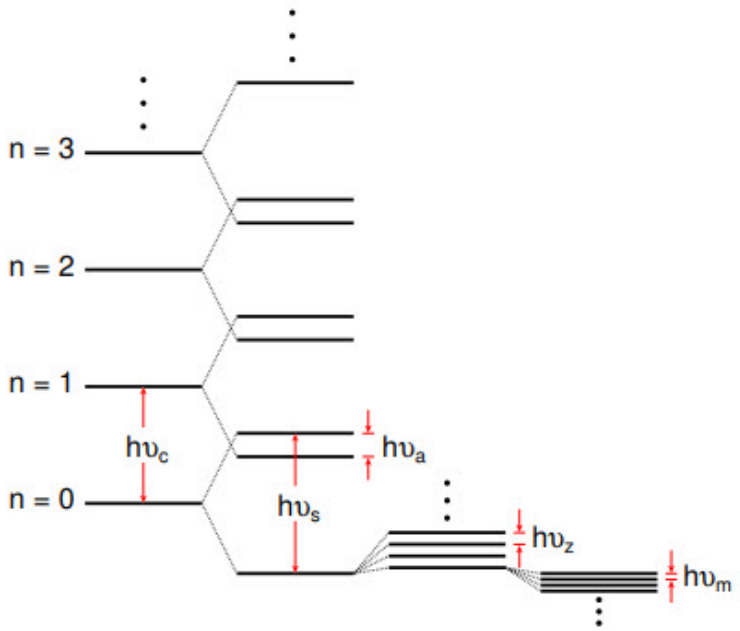

Figure 1.1: Energy level structure of one electron confined in a Penning trap. The three frequencies, ν_z, ν_m, and ν_c, describe the electron's spatial motion. In the magnetic field of the Penning trap, the electron spin may have one of two orientations, spin up or spin down, giving rise to spin states separated by energy $h\nu_s$, where $\nu_s = g\nu_c/2$.

In addition, experiments in our laboratory have shown a suppression of thermal excitation with decreased trap cavity temperature, demonstrating the ability to initialize an array of Penning trap qubits by radiatively cooling them to their ground cyclotron states [4]. Fig. 2.6 illustrates this finding, showing that thermal-photon induced quantum jumps between the lowest cyclotron states of a single electron decrease

in frequency as the trap cavity temperature is lowered.

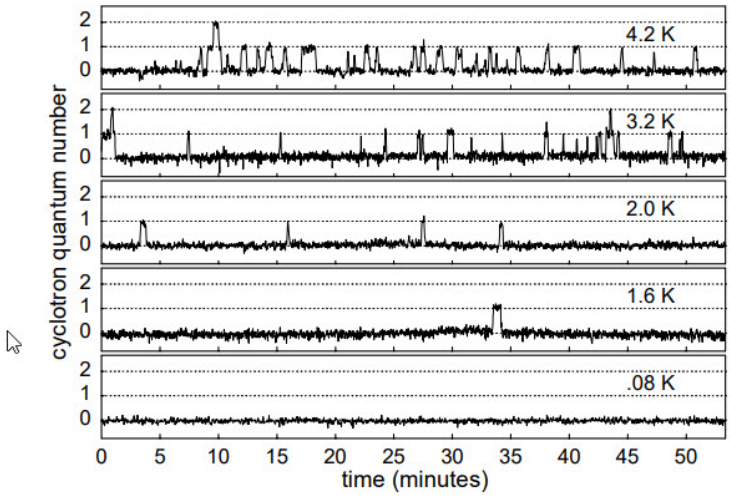

Figure 1.2: Thermal-photon induced quantum jumps between the lowest cyclotron states of a single electron trapped in a cyclindrical Penning trap [4]. Quantum transitions decrease in number over time as the trap cavity temperature is lowered, demonstrating the ability to initialize a Penning trap qubit by radiatively cooling to the ground state.

Perhaps the most attractive feature of a Penning trap qubit is the long coherence times associated with both possible quantum transitions. In the cylindrical Penning trap used in our laboratory for the most precise measurement of the electron magnetic moment, the spin state decay time is calculated to be as long as two years [43]. Cyclotron state decay times as long as 13 seconds have been demonstrated [4], more than a factor of 2 greater than the longest coherence times observed in trapped atom qubits.

The fourth requirement is the ability to couple multiple qubits and facilitate interactions between them. This has been pursued in less detail so far, but a theoretical study of electron-electron entanglement in Penning traps suggests one path toward a two-qubit quantum logic gate in a Penning trap [44].

Finally, robust quantum non-demolition measurement methods have been demonstrated and used to observe single-quantum spin flip and cyclotron state transitions [4]. Fig. 2.5 illustrates these results, showing examples of QND quantum-jump spectroscopy in a Penning trap.

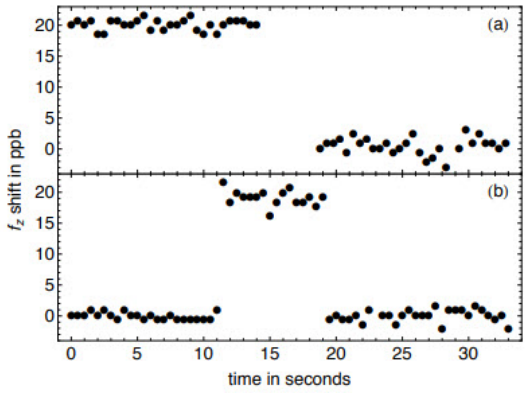

Figure 1.3: (a) QND observation of a spin-flip transition and (b) QND observation of a single-quantum cyclotron transition of a single electron trapped in a cylindrical Penning trap [45].

The one quantum computation requirement that is not met by the three-dimensional cylindrical Penning trap designs readily operated in our laboratory is scalabiltiy. To address this problem, a two-dimensional planar Penning trap design was proposed by Ciaramicoli et al. [1] and Stahl et al. [5]. The proposed scheme is illustrated in Fig. 1.4

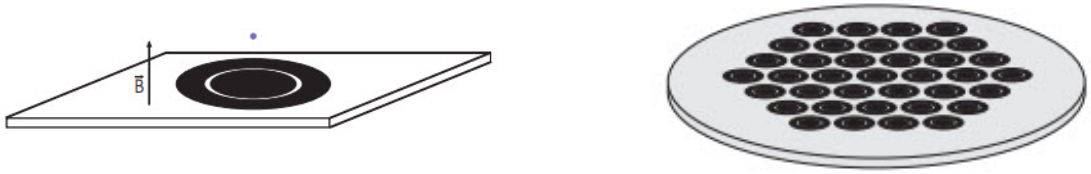

Figure 1.4: At left, a two-dimensional planar Penning trap with electrodes printed on an insulating substrate proposed by Ciaramicoli et al. [1]. At right, an array of such traps on a single substrate is proposed.

Efforts to build and operate the proposed planar Penning trap were carried out first at Mainz [46,47] and then Ulm [7]. While the trapping of 100-1000 electrons was reported, both experiments were limited by anharmonicity in the trapping potential that made the trapping and detection of a single electron unfeasible. In fact, the group at Ulm claimed that a lack of reflection symmetry makes it impossible to achieve a "genuinely harmonic" trapping potential in any planar Penning trap, and that this anharmonicity leads to a broadening of the observed axial linewidth such that it is "impossible" to resolve a single trapped electron in a two-dimensional planar Penning trap [7].

Motivated by this challenge and armed with decades' worth of experience in innovative Penning trap design, a theoretical study of the planar Penning trap was undertaken in our laboratory [3, 8]. The Ulm trap design was indeed shown to be unsuitable. However, an optimized design geometry and an anharmonicity compensation scheme was proposed to contend with the challenges confronted at Mainz and Ulm, as is discussed in Chapter 2. The fabrication of our optimized trap and its supporting apparatus is discussed Chapter 3, with modifications reported for the first time here, and its operation is demonstrated in Chapter 4. In Chapter 5, we present the first data describing the measured axial linewidths of small clouds of electrons in our optimized planar Penning trap and show that the linewidths are quantized by the single-electron linewidth, with the smallest cloud being that of 2 electrons.

Chapter 2

Purpose-Built Penning Traps

The designs of an optimized planar Penning trap and a second-generation ATRAP open-access Penning trap presented here draw on decades of experience in experimentation with Penning traps in our laboratory. A Penning trap is formed by a quadrupole electrostatic potential superimposed on a uniform magnetic field. The various Penning trap design geometries employed in our laboratory differ in the geometry of the electrodes used to produce the quadrupole electrostatic potential. As new experimental goals have presented themselves, new electrode geometries have been developed to meet these goals.

Our laboratory has demonstrated high quality quadrupole potentials with hyperbolic-shaped electrodes, closed-endcap cylindrical electrodes, and with open-access cylindrical electrode. As the geometries progressively deviate from ideal hyperbolas of revolution, optimization methods based on relative electrode dimensions and *in situ* anharmonicity compensation have been developed. These methods are extended to the design of a planar Penning trap geometry here.

This chapter summarizes the progression in Penning trap design and the salient design considerations. It begins with the physics of an ideal Penning trap, then describes the innovations that have built on this ideal, including the open-access cylindrical Penning trap design that has made antihydrogen production and study possible. It describes previous efforts at planar Penning trap design, then culminates with a summary of the design of the optimized planar Penning trap used for our current studies.

2.1 Ideal Penning Traps

The physics of a charged particle in a Penning trap is well understood [48]. An ideal Penning trap is formed by superposing a spatially uniform magnetic field, $B\hat{z}$, and a quadrupole electricstatic potential. The magnetic field serves to confine the charged particle radially in familiar cyclotron motion with angular frequency ω_c, while the quadrupole electrostatic potential, given by

$$V_{ideal} = V_0 \frac{z^2 - \rho^2/2}{2d^2} \tag{2.1}$$

in cylindrical coordinates, provides a restoring force to confine the particle axially. V_0 sets the potential scale, and the characteristic trap dimension d sets the size scale for the trap. For $\rho = 0$, the potential is that of a harmonic oscillator,

$$V(0,z) = V_0 \frac{(z - z_0)^2}{2d^2}, \tag{2.2}$$

and a charged particle of mass, m, and charge, q, will oscillate in simple harmonic motion about the potential minimum at $z = z_0$ at the axial angular frequency

$$\omega_z = \sqrt{\frac{qV_0}{md^2}}, \tag{2.3}$$

for $qV_0 > 0$. The repulsive radial term in the electrostatic potential has two effects: 1) it gives rise to a slow circular $\vec{E}\times\vec{B}$ drift motion, referred to as the magnetron motion, with angular frequency ω_m, and 2) it modifies the cyclotron angular frequency such that $\omega_c = qB/m \rightarrow \omega_c' = \omega_c - \omega_m$. The magnetron frequency is written as

$$\omega_m = 1/2(\omega_c + \sqrt{\omega_c^2 - 2\omega_z^2}) =) \approx \frac{\omega_z^2}{(2\omega_c)}. \tag{2.4}$$

Typically $\omega_m \ll \omega_z \ll \omega_c'$. The electron motions are illustrated in fig. 2.1. The axial

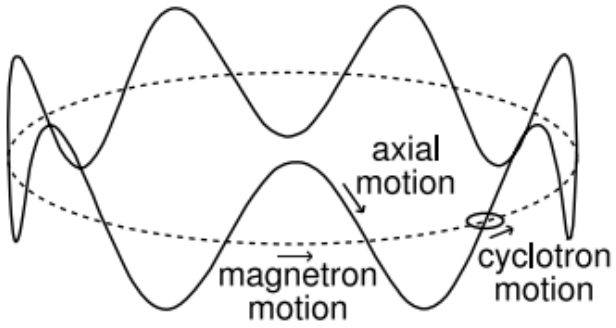

Figure 2.1: Motions of an electron in a Penning trap.

and cyclotron motions are stable; reducing the energy in these motions reduces their amplitude. In contrast, the magnetron motion is unstable. Removing energy from the magnetron motion results in an increasing magnetron radius until the confined particle is lost from the trap. However, the magnetron damping time is long, typically on the order of gigayears, and so the magnetron motion is treated as stable.

In an ideal scheme, the quadrupole potential is produced by electrodes with surfaces that lie along equipotentials of V. Therefore, early Penning traps relied on electrodes that were hyperbolic in shape [49,50]. Fig. 2.2 illustrates the ideal scheme in cross-section. Three electrodes are required, two endcap electrodes and one circular ring electrode, where z_0 and ρ_0 give the distances from the potential minimum to

the electrodes. The characteristic trap dimension is chosen to be $d = 1/2(z_0^2 + \rho_0^2/2)$, such that V_0 is the potential difference between endcap and ring electrodes. In an ideal Penning trap, the electrode surfaces would be infinitely extended and perfectly uniform; however, such a trap cannot be realized in the laboratory.

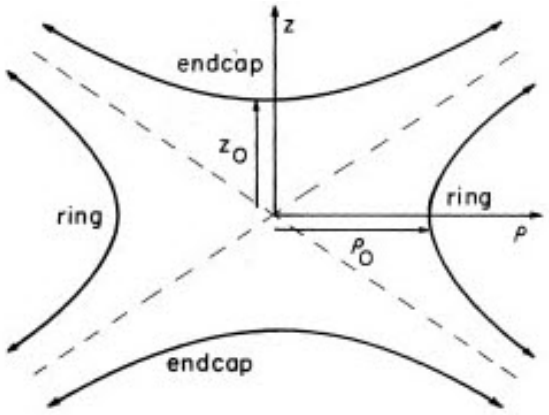

Figure 2.2: In an ideal Penning Trap, the quadrupole potential is formed by biasing infinitely-extended, flawless electrode surfaces of hyperbolic shape [49]. Three electrodes are shown: two endcap electrodes and one circular ring electrode. The quantities z_0 and ρ_0 give the distances from the potential minimum to the electrodes.

2.2 Laboratory Orthogonalized Hyperbolic Penning Traps

In the laboratory, the inherent imperfections of real electrodes lead to modifications to the ideal quadrupole potential. Actual electrodes, subject to laboratory and machining limitations, are not infinitely extended, perfect hyperbolas of revolution. A scale drawing of a laboratory hyperbolic Penning trap is shown on the left in fig.

2.3. Near the center of the trap, where $r/d << 1$, the potential is written as

$$V = V_{ideal} + \frac{1}{2}V_0 \sum_{k=0}^{\infty} C_k \left[\frac{r}{d}\right]^k P_k(cos\theta) \tag{2.5}$$

in spherical coordinates, where the first term on the right is the ideal quadrupole potential and the second term represents the unavoidable modifications, given by a series expansion of powers of r/d multiplied by orders of Legendre polynomials. This departure from an ideal quadrupole potential leads to trap anharmonicity, whereby the axial oscillation frequency is amplitude-dependent. The design challenge, then, is to minimize the leading anharmonic contributions to the potential. Because of the reflection symmetry of the design geometry, the odd values of the potential coefficient, C_k, are neglected. The coefficient C_4 quantifies the leading anharmonic contribution. To address the anharmonicity, two compensation electrodes are added to the trap design, as is shown in fig. 2.3. The anharmonicity is minimized by adjusting the bias voltage on the compensation electrodes while monitoring the effect on the axial motion detection signal. If the electrode design dimensions are chosen carefully, changing the potential on the compensation electrodes changes the anharmonicity only, while changes to the ring and endcap electrodes determine V_0 and ω_z only, and the trap is said to be "orthogonalized." At right in Fig. 2.3 are shown the optimized trap dimensions for orthogonality compared to previous trap designs [49]. Optimization occurs for $\rho_0/z_0 = 1.16$. Anharmonicity compensation is critical to observations of small shifts in the axial frequency of a trapped electron and, therefore, the quantum jump spectroscopy that spurred interest in a Penning trap qubit.

Also pictured in Fig. 2.3 is the field emission point (FEP) that serves as an electron beam source for introducing electrons into the trap. These energetic electrons

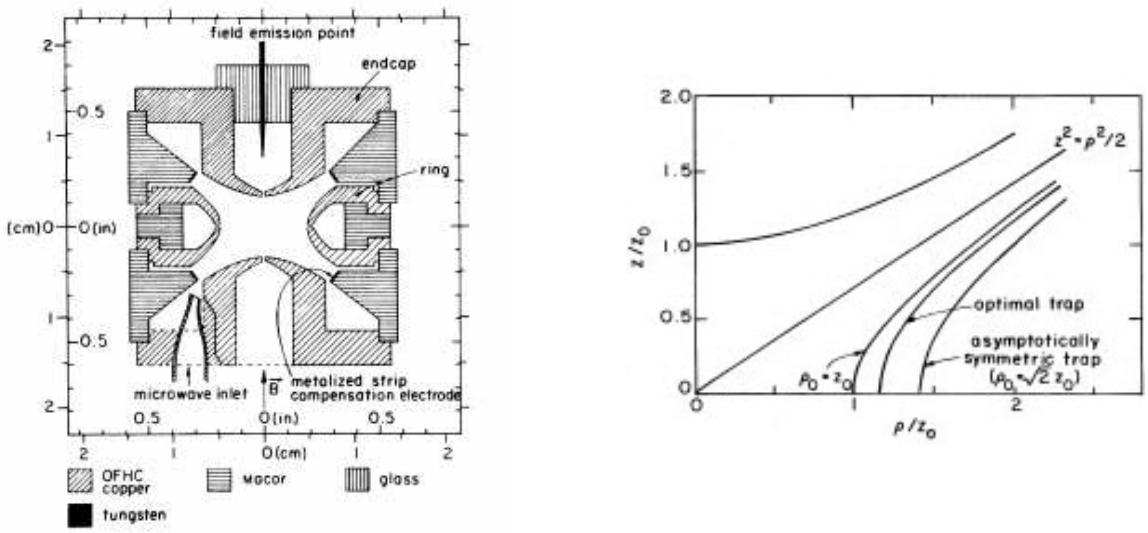

Figure 2.3: At left, a scale drawing of a laboratory Penning trap with hyperbolic electrodes [48]. Compensation electrodes are added for *in situ* tuning of the trapping potential. At right, the optimized geometry for an orthogonalized hyperbolic trap [49]. Optimization occurs for $\rho_0/z_0 = 1.16$.

collide with residual gas atoms in the trap volume and are slowed so that they may be captured. The trapped and oscillating charged particle induces an alternating image current in the electrodes, which is detected by an external circuit. The axial motion is then damped by the effective resistance of this external circuit, as the particle comes into thermal equilibrium. The cyclotron and magnetron motions are damped radiatively. Also shown in fig. 2.3 is a microwave inlet for driving cyclotron transitions.

2.3 Orthogonalized Cylindrical Penning Traps

Cylindrical Penning traps were developed in our laboratory as an innovation on the hyperbolic Penning trap [42,51]. An example of a cylindrical trap is imaged in Fig.

2.4. Machining of electrode surfaces that are hyperbolas of revolution is painstaking and prone to error. Cylindrical Penning trap electrodes, by contrast, are easier to machine and easier to construct to higher precision. The cylindrical design is also simpler to study, requiring standard electrostatic methods. An additional advantage is that the trap volume operates as a high-quality cylindrical microwave cavity and is observed to suppress spontaneous cyclotron transitions, leading to cyclotron coherence times as long as 13 seconds [4].

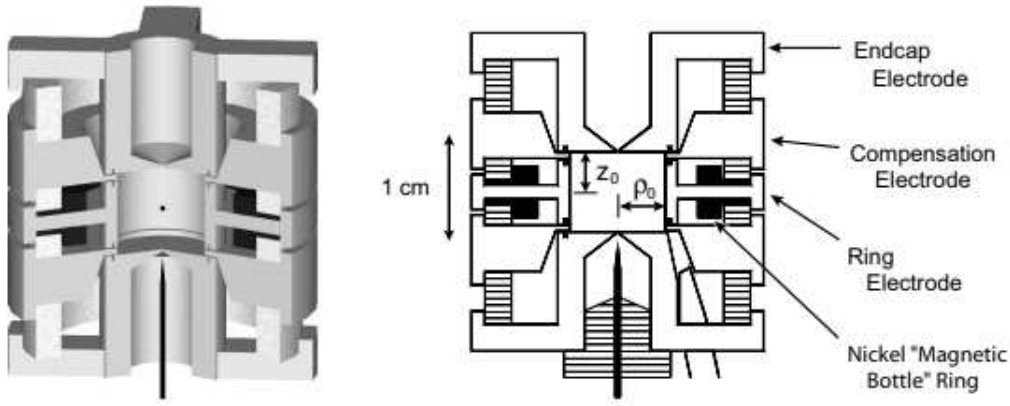

Figure 2.4: Three-dimensional and two-dimensional drawings of a cylindrical Penning trap developed in our laboratory [2].

.

As with hyperbolic Penning traps, cylindrical Penning traps may be built with orthogonalized anharmonicity compensation, given a careful choice of electrode geometry. As before, the potential, for small r/d, is expanded in even powers of r/d multiplied by even orders of Legendre polynomials:

$$V = V_{ideal} + \frac{1}{2}V_0 \sum_{k_{even}=0}^{\infty} C_k \left[\frac{r}{d}\right]^k P_k(cos\theta). \tag{2.6}$$

The coefficients are written as

$$C_k = C_k^{(0)} + D_k\Big(\frac{1}{2} - \frac{V_c}{V_0}\Big), \tag{2.7}$$

where V_c is the voltage applied to the compensation electrodes. The $C_k^{(0)}$ and D_k coefficients, found by standard boundary-value techniques, depend on the electrode geometry only. The trap is orthogonalized by choosing the dimensions z_0, ρ_0, and the compensation electrode height z_c such that D_2 vanishes and C_2 depends only on V_0 and not the compensation voltage, V_c. The axial oscillation frequency is then given by

$$\nu_z \approx \frac{1}{2\pi}\sqrt{\frac{qV_0}{md^2}(1 + C_2)}, \tag{2.8}$$

and depends on V_0 only. C_4 again quantifies the leading anharmonic contribution, where the leading terms describing the amplitude-dependence of the axial frequency are written as

$$\frac{\Delta\nu_z}{\nu_z} = \Big(\frac{3}{4}\Big)\frac{C_4}{1 + C_2}\Big(\frac{A}{d}\Big)^2 + \Big(\frac{15}{16}\Big)\frac{C_6}{1 + C_2}\Big(\frac{A}{d}\Big)^4 + \cdots. \tag{2.9}$$

To minimize the anharmonicity, C_4 is tuned to zero by choosing the electrode voltages such that

$$\frac{V_c}{V_0} = \frac{C_4^{(0)}}{D_4} + \frac{1}{2}. \tag{2.10}$$

Typical parameters for the cylindrical Penning trap shown are given in Table 2.1. The motional frequencies and damping lifetimes, given these parameters, are summarized in Table 2.2, where the frequency $\nu = \omega/2\pi$, and γ is the damping rate. An additional advantage to the cylindrical Penning trap geometry is that the trap operates as a high quality cylindrical microwave cavity and is observed to inhibit spontaneous cyclotron transitions by as much as a factor of 140 [4]. The cyclotron

decay time is controlled by tuning the cyclotron frequency relative to the radiation modes of the trap cavity, giving the 5 s decay time reported rather than the 90 ms free-space value. Decay times as long as 13 seconds have been reported [4].

B	5.36 T
ρ_0	0.4549 cm
z_0	0.3833 cm
z_c	0.0766 cm
V_0	101.4 V
V_c	74 V

Table 2.1: Typical parameters for the orthogonalized hyperbolic trap shown [45].

Motion	Frequency	Damping
magnetron	$\nu_m = 133$ kHz	$\gamma_m^{-1} \approx 4$ Gigayears
axial	$\nu_z = 200$ MHz	$\gamma_z^{-1} \approx 0.2$ seconds
cyclotron	$\nu_c = 150$ GHz	$\gamma_c^{-1} \approx 5$ seconds
spin	$\nu_s = 150.2$ GHz	$\gamma_s^{-1} \approx 2$ years

Table 2.2: Motional frequencies and damping lifetimes for the parameters summarized in Table 2.1 [45].

The addition of "Magnetic Bottle" rings, as pictured in Fig. 2.4, allows the trapped particle's cyclotron and spin states to be detected by coupling to its axial motion [52]. The nickel rings introduce a small quadratic variation in the magnetic field along the central axis:

$$B(z) = B + B_2 z^2, \tag{2.11}$$

where B is the magnitude of the homogeneous trapping field and B_2 is the bottle field. The bottle field alters the axial potential, making it dependent on the trapped parti-

cle's total magnetic moment. A change in the cyclotron state or a spin flip transition results in a shift in the axial oscillation frequency. Monitoring the axial frequency to measure the cyclotron or spin states does not alter the states; the measurement is a quantum non-demolition (QND) measurement.

With a cylindrical Penning trap, quantum jumps have been observed between the lowest cyclotron and spin states of a single trapped electron, as shown in Fig. 2.5, the transitions of interest for constructing a qubit for quantum information studies [4]. It has also been observed that thermal-photon induced quantum jumps between the lowest cyclotron states may be suppressed at sub-Kelvin temperatures as a trapped electron is cooled to its ground cyclotron state, as shown in Fig. 2.6 [4]. Building on these achievements, the cylindrical trap has made possible the most precise measurements of the electron magnetic moment and the fine-structure constant [43].

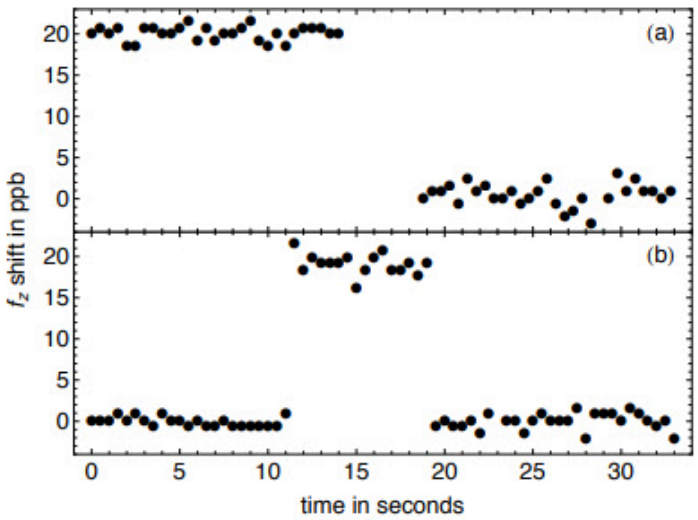

Figure 2.5: (a) QND observation of a spin-flip transition and (b) QND observation of a single-quantum cyclotron transition of a single electron trapped in a cylindrical Penning trap [45]. The cyclotron and spin flip transitions are measured as a shift in the axial oscillation frequency of the trapped particle.

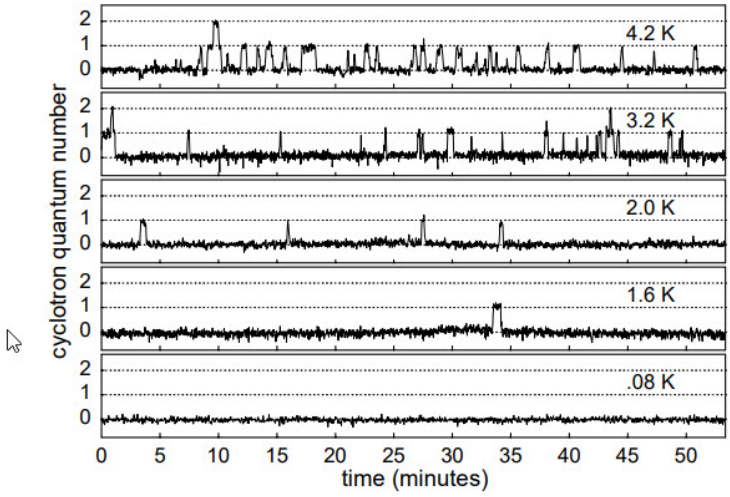

Figure 2.6: Thermal-photon induced quantum jumps between the lowest cyclotron states of a single electron trapped in a cyclindrical Penning trap [4]. Quantum transitions decrease in number over time as the trap cavity temperature is lowered.

2.4 Orthogonalized Open-Access Penning Traps

Our laboratory's efforts toward precision measurements with antiprotons and toward antihydrogen production drove the further innovation of the open-access Penning trap [53]. A drawing of an open-access Penning trap is shown in Fig. 2.7 and consists of a stack of hollow ring electrodes, with dimensions shown, separated by non-conductive spacers. The open endcap electrodes on either end of the trap allow for access for loading antiprotons from a beam, the transfer of particles, such as positrons, from stacked traps, as well as for laser beams for spectroscopic studies.

Orthogonalized anharmonicity compensation is achieved by the same methods described above, given the careful choice of the relative dimensions of the electrodes. Despite the departure from ideal hyperbolic electrode surfaces, a quality quadrupole potential is produced. With such traps, our laboratory has demonstrated the capture

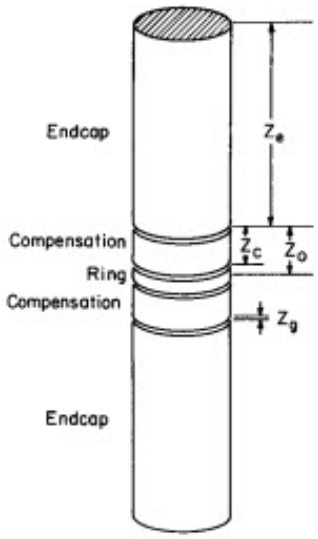

Figure 2.7: Drawing of an open-access Penning trap [53].

.

of antiprotons from a beam [54], positron cooling of antiprotons [13], the production of antihydrogen atoms [14, 15], and a direct measurement of the antiproton magnetic moment [55].

2.5 Scalability and the Planar Penning Trap

The achievements in our laboratory cited above, including QND observations of one-quantum transitions, suppression of spontaneous transitions, and long trapping and coherence times, motivated interest in building one-electron qubits in Penning traps [37–41]. However, the geometry of the cylindrical Penning trap that has met with so much success in our laboratory fails to meet the quantum computing hardware requirement of scalability. If a practical qubit is to be achieved with a single electron in a Penning trap, a new geometry is in order. As a solution, a two-dimensional planar

Penning trap was proposed in the literature [1,5,6], consisting of a central disk-shaped electrode surrounded by one or more concentric ring electrodes as illustrated in Fig. 2.8, with the future vision of an array of scalable planar Penning traps fabricated on the same chip, each containing a one-electron qubit that may be coupled to its neighbors.

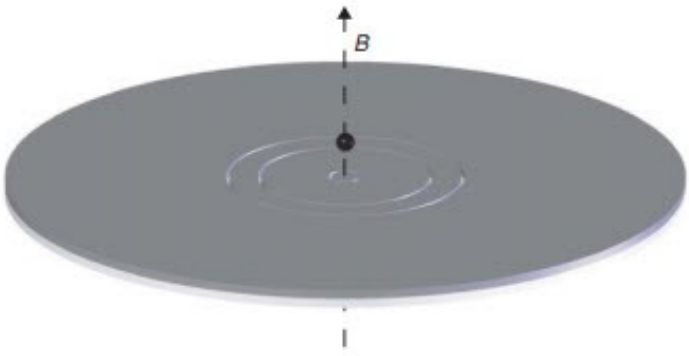

Figure 2.8: A particle confined in a planar Penning trap scheme, consisting of a central disk-shaped electrode with one or more concentric outer ring electrodes. Here, a three-gap trap is shown with two outer ring electrodes and a grounded outer plane.

2.5.1 Previous Efforts at Mainz and Ulm

Prior to our current work, two experimental efforts were undertaken to build a planar Penning trap and demonstrate its feasibility for housing a one-electron qubit, each with limited success. A first planar Penning trap was constructed and demonstrated at room temperature in Mainz, Germany [46,47]. A large number of electrons, from 100 to 1000, were confined and the three center-of-mass motional frequencies measured. Our study of the design asserts that anharmonicity due to sub-optimal electrode geometry resulted in significant broadening of the observed axial linewidth,

such that one-electron resolution would not be possible [3]. Of additional concern is the effect of charges accumulated on the insulating gap surfaces between electrodes, which are insufficiently screened by an inadequate depth-to-width gap ratio. The large number of electrons trapped falls far short of the one electron needed to demonstrate a practical Penning trap qubit.

A subsequent effort was made in Ulm, Germany to trap a single electron in a similar planar Penning trap at temperature $T \leq 100$ mK [7]. Cryogenic temperatures were chosen to avoid axial motional heating, dampen the effects of patch potentials, and increase trapping and coherence times [4,56,57]. The research group's claim, however, is that a lack of reflection symmetry makes it impossible to achieve a "genuinely harmonic" trapping potential in any planar Penning trap, and that this anharmonicity leads to a broadening of the observed axial linewidth such that it is "impossible" to resolve a single trapped electron in a two-dimensional planar trap [7]. Studies conducted in our laboratory suggested otherwise [3].

In the following section, a summary of these studies is given. It was shown that the designs at Mainz and Ulm were indeed unsuitable to producing a harmonic quadrupole potential. Additionally, these studies showed that a careful choice of electrode geometry and bias potentials can successfully produce a quadrupole potential of sufficient quality to trap a single electron, making way for a Penning trap qubit.

2.6 An Optimized Planar Penning Trap Design

The design of a planar Penning trap with the ability to produce a sufficiently harmonic quadropole potential has been presented previously by our laboratory [3,8,

9]. A summary is presented here as it pertains to our present studies.

2.6.1 Electrostatics of a Planar Penning Trap

A quadrupole trapping potential is produced by biasing three concentric ring electrodes, which lie in the $z = 0$ plane, as shown in Fig. 2.9. Each electrode, with radius ρ_i, is biased to potential V_i. The potential beyond the outer electrode is taken to be zero. The gaps between the electrodes are initially taken to be infinitesimal. To derive the potential for $z \geq 0$, the boundary conditions are assumed such that for large z and large ρ, the potential is zero.

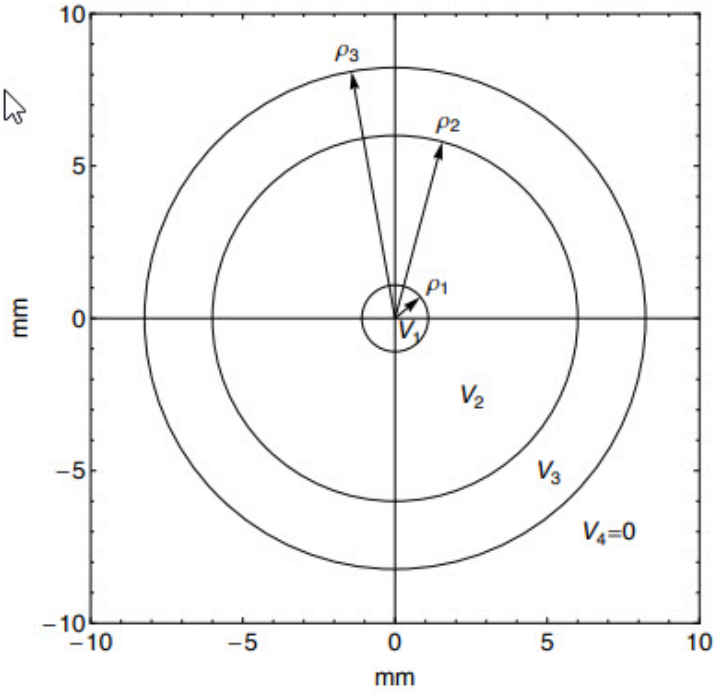

Figure 2.9: The geometry of an optimized planar Penning trap consists of three concentric ring electrodes in the $z = 0$ plane. Each electrode, with radius ρ_i, is biased to potential V_i. [3]

.

It is useful to scale distances in terms of the radius of the central electrode, ρ_1, such that $\tilde{\rho} = \rho/\rho_1$ and $\tilde{z} = z/\rho_1$. Likewise, the trap potential, V, and the electrode bias voltages, V_i, are scaled by V_0, such that $\tilde{V} = V/V_0$ and $\tilde{V}_i = V_i/V_0$. The scaling potential, V_0, will be defined presently.

The trapping potential is given by the linear superposition,

$$V(\tilde{\rho}, \tilde{z}) = \sum_{i=1}^{3} V_i \phi_i(\tilde{\rho}, \tilde{z}), \tag{2.12}$$

of the bias voltages applied, V_i. The functions ϕ_i are solutions to Laplace's equation with the boundary condition that $\phi_i = 1$ on each electrode and is otherwise equal to zero. The ϕ_i potentials are independent of the electrode bias voltages and depend only on the relative electrode geometry. Standard electrostatics methods give the ϕ_i for $\tilde{z} \geq 0$ as integrals over Bessel functions,

$$\phi_i(\tilde{\rho}, \tilde{z}) = \tilde{\rho}_i \int_0^\infty dk e^{k\tilde{z}} J_1(k\tilde{\rho}_i) J_0(k\tilde{\rho}) - \tilde{\rho}_{i-1} \int_0^\infty dk e^{k\tilde{z}} J_1(k\tilde{\rho}_{i-1}) J_0(k\tilde{\rho}), \tag{2.13}$$

with the convention $\tilde{\rho}_0 = 0$. On the $\tilde{\rho} = 0$ axis, the expression reduces to

$$\phi_i(0, \tilde{z}) = \frac{\tilde{z}}{\sqrt{(\tilde{\rho}_{i-1})^2 + \tilde{z}^2}} - \frac{\tilde{z}}{\sqrt{(\tilde{\rho}_i)^2 + \tilde{z}^2}} \tag{2.14}$$

for our boundary conditions.

To characterize the planar Penning trap potential, we focus on expansions of the potential on the $\tilde{\rho} = 0$ axis, as we did in characterizing the cylindrical Penning trap potential above. The potential due to one electrode, ϕ_i, near an expansion point $\tilde{z}_0$ on the axis is written as a Taylor series,

$$\phi_i(0, \tilde{z}) = \frac{1}{2} \sum_{k=0}^{\infty} C_{ki} (\tilde{z} - \tilde{z}_0)^k. \tag{2.15}$$

The expansion coefficients are functions of the relative trap geometry, $\tilde{\rho}_i$, and the location of the expansion point, $\tilde{z}_0$, and are written as

$$C_{ki} = \frac{2}{k!}\Big[\frac{\partial^k \phi_i(0,\tilde{z})}{\partial \tilde{z}^k}\Big]_{\tilde{z}=\tilde{z}_0}. \tag{2.16}$$

The full trap potential is expanded as

$$V(0,\tilde{z}) = \frac{1}{2}V_0 \sum_{k=0}^{\infty} C_k(\tilde{z}-\tilde{z_0})^k. \tag{2.17}$$

The one expansion coefficient needed for $k = 2$ is written as $V_0 C_2$. With no loss of generality, C_2 is chosen such that $C_2 = 1$. V_0 and the expansion coefficients C_k are then defined as

$$V_0 = \sum_{i=1}^{3} C_{2i} V_i, \tag{2.18}$$

$$C_k = \sum_{i=1}^{3} C_{ki} \tilde{V}_i. \tag{2.19}$$

Equation (2.19) serves as a constraint equation that an acceptable set of relative potentials must satisfy:

$$C_2 = \sum_{i=1}^{3} C_{2i} \tilde{V}_i = 1. \tag{2.20}$$

A trap is formed at the expansion point, $\tilde{z}_0$, only if there is a minimum in the potential energy, which is given by $qV(0,\tilde{z})$ for a particle with charge q. The linear gradient must then vanish at this point, which gives the additional constraint

$$C_1 = \sum_{i=1}^{3} C_{1i} \tilde{V}_i = 0. \tag{2.21}$$

Near the minimum, the potential energy takes the form $m\omega_z^2(z-z_0)^2/2$, where m is the mass of the charged particle and ω_z is the axial oscillation frequency. By comparing to the quadratic term in the expansion of the full potential, we write

$$\omega_z^2 = \frac{qV_0}{m\rho_1} \tag{2.22}$$

because of our choice of V_0, in direct correspondence with the ideal case.

2.6.2 Axial Motion and Anharmonicity in a Planar Penning Trap

The observation of a single electron in an optimized Planar Penning trap relies on the detection of the trapped electron's axial oscillation motion. In an ideal trap, with a perfectly harmonic potential, an electron oscillates on axis in harmonic motion about the potential minimum with a frequency ω_z that is independent of the amplitude of the motion. However, an electron trapped in an anharmonic potential will oscillate at a frequency that is dependent on the amplitude of its motion.

Solution of the equation of motion for a trapped electron in a potential described by equation 2.15 gives an expression for the amplitude-dependent axial frequency:

$$\omega_z(\tilde{A}) = \omega_z \left[1 + \sum_{k=2}^{\infty} a_k \tilde{A}^k \right]. \tag{2.23}$$

The amplitude coefficients a_k are functions of the potential expansion coefficients C_k, given by Eq. 2.22. Note that the potential expansion coefficients are in turn functions of the trap electrode radii ρ_i and potentials V_i that we are seeking to optimize. This is very useful. A change in the potential V_i applied to each electrode will change the axial frequency ω_z, and, importantly, it will also change the amplitude dependence of the axial frequency by changing a_2. The anharmonicity is, therefore, tunable.

One concern is the thermal spread in axial frequencies. As described above for cylindrical Penning traps, the axial motion of the trapped electron is detected by coupling to a tuned-circuit amplifier with an effective resistance, R. The axial motion

is damped as the electron comes into thermal equilibrium with the detection circuit. Thermal fluctuations of the electron's axial energy result in a range of oscillation frequencies, $\Delta\omega_z$. In the cyclindrical traps described above, the spread in frequencies is less than the axial damping linewidth, γ_z, making it possible to observe a single electron. However, in planar Penning trap efforts at Mainz and Ulm, measurement resolution was limited by the fact that the thermal spread in frequencies was very much larger than the single-electron linewidth.

As a measure of the thermal broadening of the axial linewidth, we consider the lowest-order term:

$$\frac{\Delta\omega_z}{\omega_z} \approx |a_2| \frac{k_B T_z}{\frac{1}{2} m \omega_z^2 \rho_1^2}. \tag{2.24}$$

Our goal, then, is to choose optimized trap parameters that minimize a_2 and, subsequently, the anharmonicity of the trapping potential. Additionally, we rely on changes in the applied potentials to tune the anharmonicity *in situ*. Fine adjustments to the optimized potentials V_i applied to the electrodes will tune a_2, and in turn the amplitude dependence of the axial frequency and the thermal broadening contribution to the axial linewidth we rely on for detection.

2.6.3 Optimizing the Planar Penning Trap

Optimization proceeded by calculating the two scaled radii, $\tilde{\rho}_2$ and $\tilde{\rho}_3$, the scaled potential minimum, $\tilde{z}_0$, and the three scaled potentials, $\tilde{V}_1$, $\tilde{V}_2$, and $\tilde{V}_3$, that meet the constraints. To form a trap at all requires the electrostatic constraints $C_1 = 0$ and $C_2 = 1$. To make the trap harmonic, it is required that the lower order amplitude coefficients, a_i, vanish as well as the potential expansion coefficients, C_i, on which

they depend. The highest level of optimization is given by the additional constraints of $C_3 = C_4 = C_6 = 0$, which gives $a_2 = a_3 = a_4 = a_5 = 0$. What appear to be nine constraints are only five, because of the interdependence of the coefficients involved. There is one more parameter to choose than there are constraints. The free parameter leads to a range of possible relative geometries, which are indicated by the dashed line in Fig. 2.10.

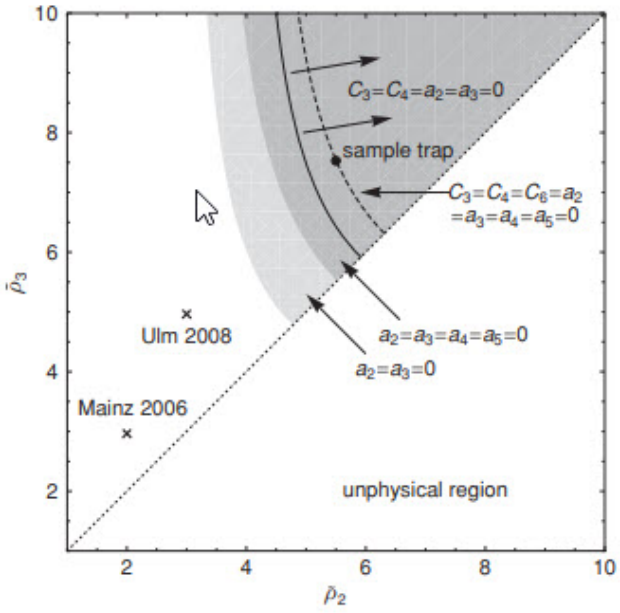

Figure 2.10: Optimized planar Penning trap electrode geometry for various sets of constraints [3]. The relative electrode radii for the planar Penning trap developed for this study are indicated by the sample trap point along the dashed line of possible relative geometries. No optimized traps are possible in the unshaded region, where the traps at Mainz and Ulm are found.

.

The laboratory trap described in the following chapters was built according to the sample trap dimensions indicated by the dot along the dashed line in the figure. The shaded regions indicate parameter configurations optimized for the constraints

shown. No optimized traps are possible in the unshaded region, where the traps at Mainz and Ulm are found, showing that it was unlikely that these could be made to work.

Fig.2.11 shows the possible optimized trap configurations. In plot (a), the possible optimized scaled electrode radii are shown as a function of the scaled distance $\tilde{z_0}$. Optimized configurations are given by only a narrow range of distances $\tilde{z_0}$ from the central electrode to the potential minimum. The sample trap configuration we chose is indicated. In (b), the optimized scaled potentials are shown. And in (c), the potential expansion coefficient C_5 is given, which describes the leading departure from a harmonic potential. No optimized configurations exist for $C_5 = 0$. For our sample trap, $C_5 = -0.011$.

Values for the optimized parameters are summarized in Table 2.3. The axial frequency $f_z = \omega_z/2\pi$ of 64 MHz was chosen for convenience of RF detection. The calculation of the thermal linewidth broadening of $\Delta f_z = 0$ is found for a 5 K thermal distribution of axial energies. The damping width, γ_z, is found for detection on the central electrode with a detection circuit effective resistance of 100 kΩ.

2.6.4 Tuning the Anharmonicity *In Situ*

A planar Penning trap in the laboratory will not meet these calculated specifications. Real electrodes are separated by gaps that are non-negligible. The electrode plane is finite and contained within a conductive enclosure with dimensions given by practical laboratory limits. The electrode dimensions are subject to machining tolerances. These unavoidable imperfections were examined in detail [3]. Estimates

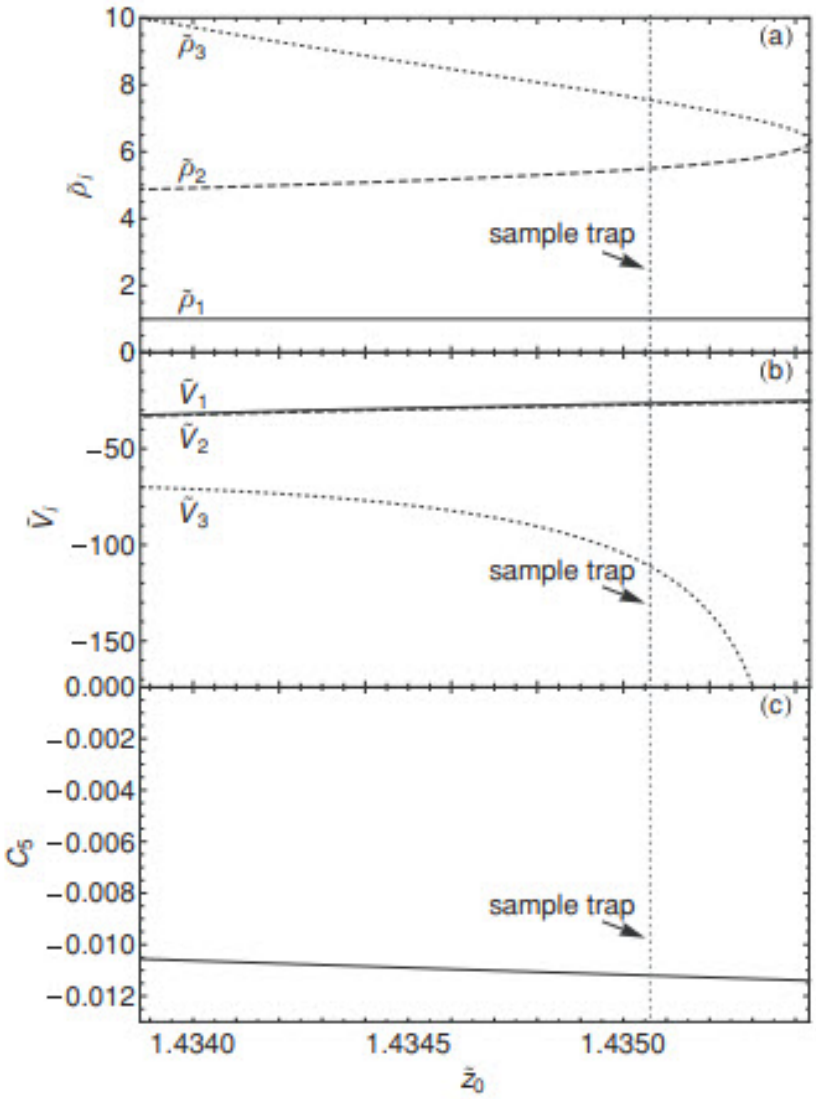

Figure 2.11: The optimized planar Penning trap parameters [3]. (a) The optimized scaled electrode radii as a function of the scaled distance $\tilde{z}_0$. Optimized configurations are given by only a narrow range of distances $\tilde{z}_0$ from the central electrode to the potential minimum. The sample trap configuration is indicated. (b) The optimized scaled potentials. (c) The potential expansion coefficient C_5. No optimized configurations exist for $C_5 = 0$. For the sample trap, $C_5 = -0.011$.

.

Parameter	**Optimized value**
ρ_1	1.0909 mm
ρ_2	6 mm
ρ_3	8.2283 mm
z_0	1.5655 mm
f_z	64 MHz
V_0	-1.0941
V_1	28.9064 V
V_2	29.6361 V
V_3	121.6051
Δf_z	0.0
$\gamma_z/2\pi$	13.16 Hz

Table 2.3: Optimized planar Penning trap parameters. The calculation of the thermal linewidth broadening of $\Delta f_z = 0$ is found for a 5 K thermal distribution of axial energies. The damping width, γ_z, is found for detection on the central electrode with a detection circuit effective resistance of 100 kΩ.

were used to explore the feasibility of adequately tuning away the resultant anharmonicity. The tunability of the optimized trap seemed to be sufficient to overcome these unavoidable imperfections.

Fig. 2.12 illustrates the trapping potential under real boundary conditions in the laboratory. A cross-sectional view of the trap electrodes and equipotentials spaced by V_0 is shown. The equipotentials of an ideal quadrupole, indicated as dashed lines, are shown for comparison near the trap center. The conducting enclosure changes the lower-order C_k and a_k coefficients to non-zero values, which may be compensated for by small changes in the potentials applied to the electrodes.

In situ anharmonicity tuning has been demonstrated with great success in cylindrical Penning traps. As was discussed, the process of tuning a cylindrical Penning trap is greatly simplified by choosing relative electrode dimensions such that the trap is orthogonalized. In an orthogonalized trap, changing the potential on the compensation electrodes changes a_2 only, while changes to the ring and endcap electrodes determines V_0 and ω_z only.

A planar Penning trap cannot be orthogonalized. Changing the potential on each electrode will always change both a_2 and ω_z. It is therefore necessary to adjust all three potentials, V_i, at the same time to tune away the anharmonicity and optimize trap performance. In practice, one potential is stepped, while the other two are calculated such that 1) the axial frequency, ω_z, stays constant and within detectable range, and 2) the distance from the potential minimum to the central electrode, z_0, remains constant. Changes in z_0 would otherwise affect the observed linewidth of the detection signal and confound efforts to tune. Fig. 2.13 illustrates the tunability of

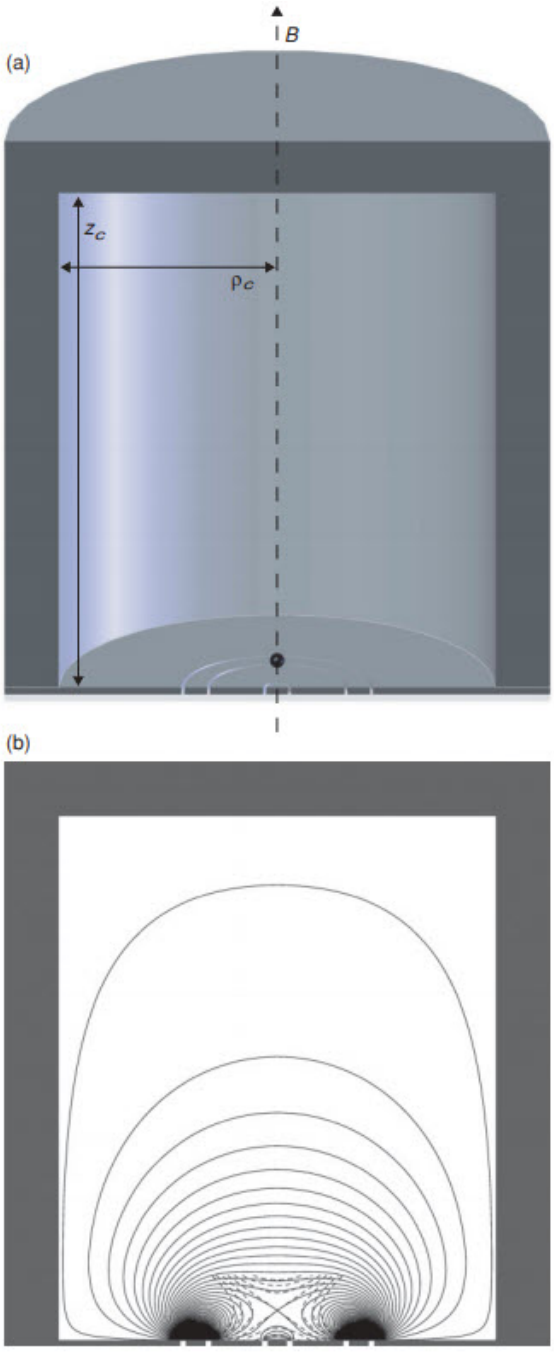

Figure 2.12: (a) The ideal trapping potentials are modified by boundary conditions given by a grounded, capped cylindrical enclosure of radius ρ_c and height z_c. (b) A cross-sectional view of the trap electrodes and equipotentials spaced by V_0 is shown. The equipotentials of an ideal quadrupole, indicated by dashed lines, are shown for comparison near the trap center. Image from [3].

.

the optimized planar Penning trap. Potentials are identified such that $a_2 = 0$ and $a_4 = 0$ both with and without the estimated fabrication imprecision. The constant z_0 contour is shown in blue. A successful path to *in situ* anharmonicity compensation in a laboratory planar Penning trap is indicated.

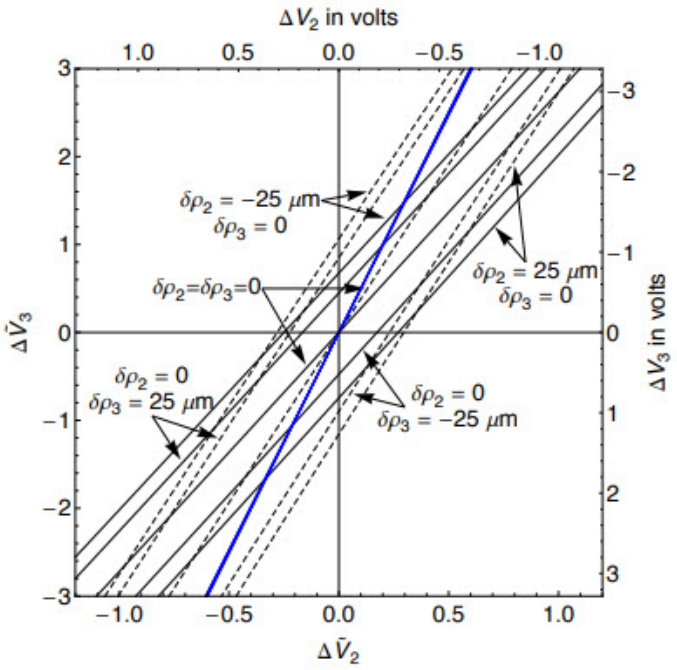

Figure 2.13: The tunability of the optimized planar Penning trap is illustrated [9]. Potentials are identified such that $a_2 = 0$ and $a_4 = 0$ both with and without the estimated fabrication imprecision. The a_2 contours are shown as solid lines. The a_4 contours are shown as dashed lines. The constant z_0 contour is shown in blue. The value of V_1 is determined such that the axial frequency remains constant at 64 MHz.

.

2.6.5 Electron Detection in an Optimized Planar Penning Trap

Observation of a single electron in our optimized planar Penning trap relies on the detection of the image current induced in the nearby electrodes by the electron's axial

oscillatory motion. The small current is coupled to a tuned-circuit amplifier that is resonant at the electron's axial frequency [48,58]. The voltage drop across the effective resistance, R, of the amplifier circuit provides the detection signal that is subsequently amplified. The axial energy of the electron is also dissipated in this resistance as the axial motion is damped and the electron comes into thermal equilibrium with the detection circuit.

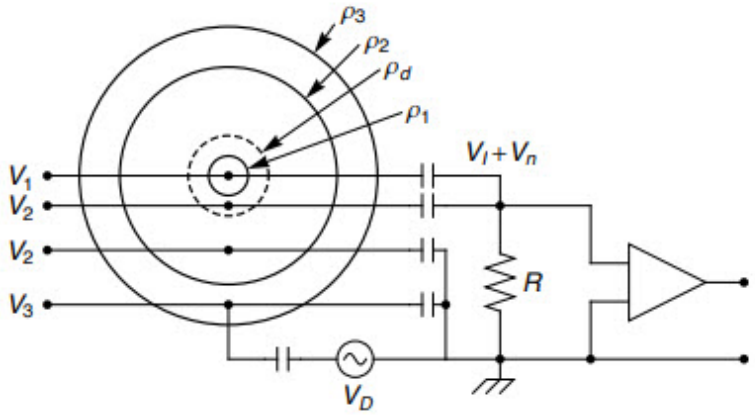

Figure 2.14: The electron detection scheme in a planar Penning trap [9]. The trap electrode radii and bias potentials are indicated, as is the resistance, R, critical to damping and detection. Contributions to the oscillatory voltage are the induced voltage, V_I, induced by the motion of the electron, and the voltage due to thermal Johnson noise in the circuit, V_n. An optional drive, V_D is shown for driving the particle motion. An extra, optional gap is indicated by a dashed circle with radius ρ_d, which may be added to optimize damping and detecton.

.

A simple detection circuit is shown in Fig. 2.14, and the scheme is discussed in detail in Ref. [3]. The trap electrode radii and bias potentials are indicated, as is the resistance critical to damping and detection. An extra, optional gap is indicated by a dashed circle with radius ρ_d, which may be added to optimize damping and

detection. The detection signal consists of the oscillatory voltage induced by the electron's axial motion in the electrodes where $\rho < \rho_d$ and the voltage due to the thermal Johnson noise in the circuit. The instantaneous electric field experienced by an electron oscillating near the potential minimum at z_0 is given by

$$E_i(\tilde{z_0}) \approx -\frac{D_1}{2\rho_1} V_i, \tag{2.25}$$

where potential V_i is applied to electrode with radius ρ_i. The D_1 factor depends on the geometry of the electrode and the distance of the potential minimum from the electrode plane, and is given by

$$D_1 = C_{1d} = \frac{-2(\tilde{\rho_d})^2}{\left[(\tilde{z_0})^2 + (\tilde{\rho_d})^2\right]^{3/2}}, \tag{2.26}$$

where C_{1d} is the potential expansion coefficient defined in Eq 2.16. Maximum coupling of the circuit and the trapped electron occurs for the maximum magnitude of C_{1d} at $\rho_d = \sqrt{2}\tilde{z_0}$. For simplicity, an additional gap is not introduced and detection proceeds on the central electrode alone. Fig. 2.15 shows the electric field coefficient D_1 for detection on the various electrodes of the sample trap as a function of the distance z_0. For detection on the central electrode, with radius ρ_1, the D_1 coefficient reduces to

$$D_1 = C_{11} = \frac{-2}{\left[(\tilde{z_0})^2 + 1\right]^{3/2}} = \frac{-2}{\left[(z_0/\rho_1)^2 + 1\right]^{3/2}}. \tag{2.27}$$

The voltage signal induced by the oscillatory motion of the trapped electron is proportional to the velocity of its axial motion and is written as

$$V_I = \frac{eD_1}{2\rho_1} R\dot{z}, \tag{2.28}$$

in terms of the electric field coefficient and the resistance, R [48]. As discussed, the electron's axial energy is dissipated in the resistance as its axial motion is damped.

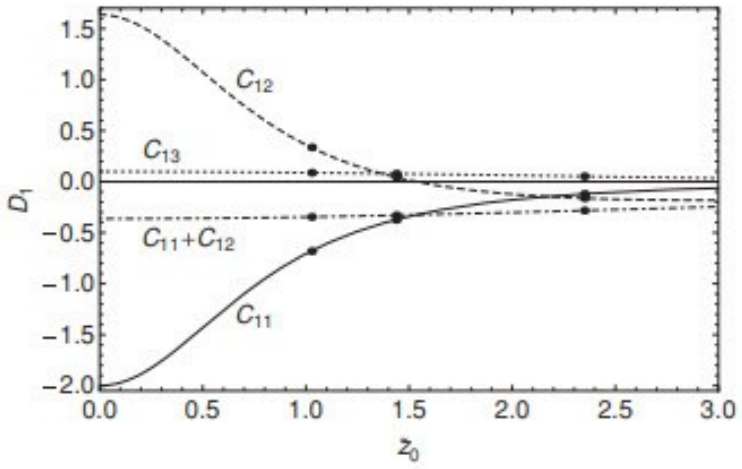

Figure 2.15: The electric field coefficient, D_1, as a function of the distance z_0 for detection and damping on the various electrodes of optimized planar Penning trap.

.

The damping rate of the electron is then written as

$$\gamma_z = \left(\frac{eD_1}{2\rho_1}\right)^2 \frac{R}{m}, \tag{2.29}$$

where e and m are the electron's charge and mass, respectively. In the following chapters, we see that the damping rate is the axial linewidth that is measured and correlated with the number of electrons in the trap. While we have focused in this chapter on minimizing the thermal anharmonicity contribution to the axial linewidth, it is also advantageous to maximize the damping by maximizing the resistance, R, such that $\gamma_z >> \Delta\omega_z/2\pi$.

Chapter 3

The Planar Penning Trap Apparatus

The fabrication of the planar Penning trap experimental apparatus draws on our laboratory's considerable experience with materials and methods suitable to the cryogenic, UHV, and high-magnetic-field environment in which the experiment is conducted, as well as to the RF methods used to detect and manipulate the axial motion of the trapped electron. This chapter describes the fabrication of the planar Penning trap, the vacuum enclosure and dilution refrigerator that ensure an environment conducive to trapping and long lifetimes, the magnet that provides radial confinement, and the electronics that allow for detection of a confined electron.

A fully refurbished experiment is presented, which builds on previous efforts [9], with new modifications to the trap electrodes and the detection electronics to improve trap stability and detection sensitivity. New trap electrodes are prepared, polished and gold-electroplated to an adequate thickness to resist the rapid surface corrosion by oxidation that troubled previous efforts. An electrode gap height-to-width aspect ratio of 1.2 is reported, a value 3.4 times the aspect ratio of the trap operated at Ulm,

which is meant to screen charges on the insulting substrate that may have contributed to the broad spread of frequencies observed there.

A rebuilt first-stage cryogenic tuned-circuit detection amplifier is described. The quality factor Q that quantifies its performance is measured. The previous iteration showed a Q of 1200 at a temperature of 4 K in a test dewar, but only a value of 400 on the experiment at milli-Kelvin temperatures. The new first-stage amplifier Q is measured to be 1700 on the experiment at 100 mK, demonstrating a significant improvement in signal-to-noise.

Also described is a new second-stage cryogenic amplifier. The previous second-stage amplifier relied on positive feedback to attain the needed gain, which compromised its stability and reliability. A new design uses negative feedback for greater stability. Still, a forward gain as high as 25 dB is demonstrated, a factor of 2 improvement over the gain of 12 dB measured with the previous amplifier.

3.1 Planar Electrodes

At the heart of the experiment are the planar Penning trap electrodes that are biased to create the quadrupole trapping potential. Mechanical design and fabrication are described in detail in the following sections.

3.1.1 Materials and Fabrication

Fabrication of the electrodes begins with a double-clad copper-on-alumina substrate, prepared by Curamik Electronics. The 2" $\times$ 2" $\times$ 0.25" aluminum oxide ceramic wafer was chosen for its nonmagnetic properties, its low loss at RF (dielectric

constant 10), and its high resistivity ($10^{13}\Omega * cm$), meeting the requirements for high leakage resistance between electrode surfaces. The 96% alumina samples are sourced from CeramTec AG and made from Rubalit®7085; the remaining composition is $3.2\%SiO_2$, $1.2\%MgO$, and $< 1\%CaO$. The copper cladding, bonded to each side of the alumina substrate, is made of 0.008" thick OFE copper foil. OFE copper, 99.99% pure, with $\leq 10ppm$ nickel and iron concentration, has been used routinely in our lab as an electrode material for its nonmagnetic properties, high electrical and thermal conductivity, affordability, and ease of use. To fabricate the substrate, the copper is direct-bonded to the alumina as the materials are heated to a temperature above the copper-oxygen eutectic melting point of 1065^oC in an oxygen furnace atmosphere. There is no additional adhesive layer.

The boundaries of the electrodes are formed by laser-etching. The etching was performed by Gateway Laser, Inc with a specified kerf width of $50^{+25} - 0$ μm (2^{+1}_{-0}), where the kerf is the width of the material removed by the cutting process. The fabricated planar Penning Trap substrate with well-defined electrodes and electrical connections is pictured in Fig. 3.1. A number of factors contribute to the choice of laser-etching as a fabrication method and to the specified width of the groove that determines the individual electrode boundaries [9]. The electrostatic requirements for the quadrupole trapping field dictate a gap width as small as possible. At the same time, good electrical isolation requires a large leakage resistance between electrode surfaces and suppressed arcing. Also, a wider gap and larger leakage resistance (and smaller capacitance) is directly relevant to electron detection and adequate signal-to-noise. Additionally, the gap depth-to-width ratio must be greater than one in order

to screen the potential effect of stray charges on the alumina insulator between the electrode surfaces. Finally, there is the practical matter of machining limitations. Traditional lithography methods used to make conventional printed circuit boards are not compatible with the gap depth-to-width aspect ratio needed. Laser-etching capabilities allow for the most satisfactory balancing of the above considerations: a sufficient gap aspect ratio for the narrowest width obtainable that ensures a large leakage resistance between electrodes and robust electron detection. Leakage resistance and capacitance is measured after electrode surface preparation and is reported in the following section.

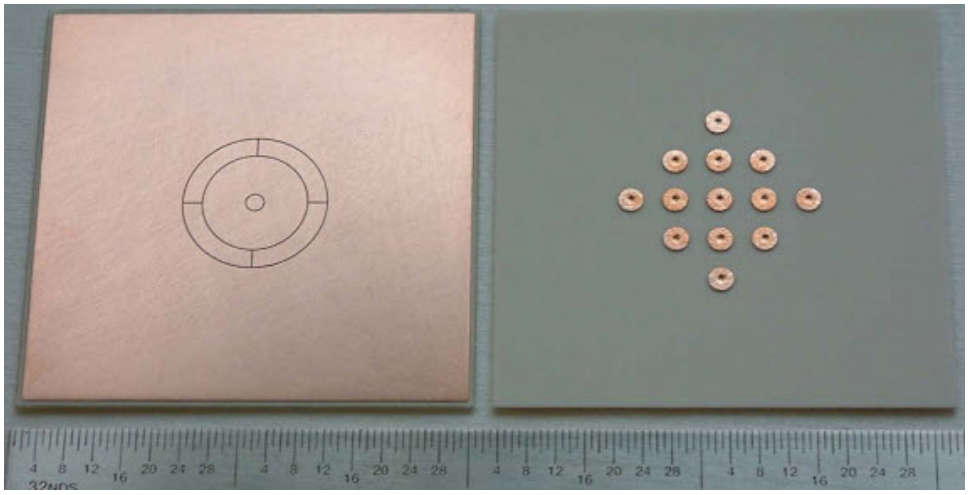

Figure 3.1: Photograph of the planar Penning Trap substrate. Copper and alumina layers are joined by direct-bonding, and electrodes and electrical contact pads are formed by laser-etching.

During etching, the laser penetrates the copper layer and enters the ceramic substrate. It is not possible to achieve perfectly vertical sidewalls on the boundary grooves; efforts were made by the machinist to assure that the bottom of the groove met the specified kerf width. The boundary dimensions are measured from the center of the central electrode to the center of the corresponding gap with a compound

microscope and CCD camera, with the uncertainty in measurement due to identifying the edge of the boundary by eye. Table 3.1 summarizes and compares the ideal, desired dimensions and the measured, as-built dimensions.

Electrode radius	**Desired**	**Measured**
ρ_1	1.091 mm	1.05 ± 0.02 mm
ρ_2	6.000 mm	6.04 ± 0.04 mm
ρ_3	8.228 mm	8.19 ± 0.05 mm

Table 3.1: A comparison of specified electrode radii and the measured, as-built dimensions. Dimensions are measured with a compound microscope and CCD camera, with the uncertainty in measurement due to identifying the electrode boundary edge by eye. The limited microscope field makes the larger radii more difficult to measure.

The hermetic filled vias pictured in Fig. 3.1 allow for direct electrical connection with the bottom copper layer for electrode biasing. Prior to direct-bonding the copper and alumina layers, thirteen 1.0 mm holes are drilled in the alumina substrate where potential electrical connections may be made: one at the center and four equally spaced on each of the outer electrodes. The vias are formed immediately after the direct bonding process, while the copper layers are still soft. The soft copper layers are brought together through the holes in the alumina substrate by pressing a graphite tip on the bottom layer, pushing it through the hole, and onto the top layer. The bottom layer is subsequently etched, as pictured, leaving thirteen 3.0 mm diameter contact pads for electrical connection.

3.1.2 Refurbishing the Electrode Surface Finish

Surface fields that may alter the applied quadrupole trapping potential are minimized by careful electrode surface preparation. Regions of fixed surface potential, or so-called patch potentials, may arise due to the polycrystalline structure of the conductor or the presence of adsorbed elements [59]. To minimize these effects, the surfaces of the electrodes are polished to a mirror-like finish and then plated with gold. Gold, known for its lack of chemical reactivity, resists the surface reactions that promote surface potential structure, while also resisting the longer-time-scale corrosion by oxidation to which copper is susceptible.

During earlier efforts with this apparatus, corrosion of the electrode surfaces proved problematic [9]. First efforts to operate the trap with bare copper electrodes resulted in rapid oxidation with thermal cycling, despite previous experience in our lab with successfully operating solid copper electrodes under vacuum over months to years. A possible culprit is oxide inclusions that may have been introduced by the copper-to-alumina direct-bonding process, which takes place in an oxygen furnace atmosphere. To combat oxidation, a thin layer of gold, 50-100 nm, was applied by electro-plating. However, over several years, the layer proved too thin to prevent copper migration through the gold and subsequent oxidation. It has been shown that copper will migrate through a 100 nm layer of gold within several months [60]. In the present studies, the electrodes have been replaced and surfaced by methods that build on this previous experience. After hand-polishing, the electrodes are electro-plated with a 1 μm layer of gold, consistent with conventional electronics industry specifications, and according to Pucic et.al., able to resists copper migration for several tens

to hundreds of years [60].

Surface polishing is performed by hand using a series of polishing papers with successively smaller grit sizes. The electrode plane is inverted onto the polishing paper, which lies on the flat surface of a granite table. 3M Wetordry polishing paper (alumina on fabric backing) is used. Polishing begins with 9 micron grit paper and proceeds to 3 micron, then 2 micron, and finally 1 micron grit size. The inverted plane is moved by hand in one direction until only markings in that direction appear. The plane is then rotated 90 degrees, and the process is repeated until 1 micron grit paper is reached. Between the different grit size polishing steps, the plane is cleansed in deionized water to remove copper particles and grit loosened during the polishing process that may mar the surface on successive steps.

In preparation for gold electro-plating the polished copper electrode surfaces, the plane is cleaned by conventional laboratory procedure: first by submersion in hexane, then acetone, and finally isopropol alcohol. The gaps between electrodes readily accumulate particulate matter created during the polishing process, which is dislodged by a pressurized stream of the solvent fluids. The gold is deposited by electro-plating using TG-25 RTU plating solution by Technic, Inc., a non-cyanide gold-sulfite formulation with an arsenic brightener. For a plating current of 42 mA, a deposition rate of 0.2 microns/minute is achieved; 5 minutes of plating produces a gold layer of roughly 1 micron. The gold-plated electrode plane is shown in Fig. 3.2, secured within its retaining frame.

Though polished to a surface roughness of roughly 1 micron, the surfaces of the electrodes are not featureless. While it is typical in our laboratory to achieve a

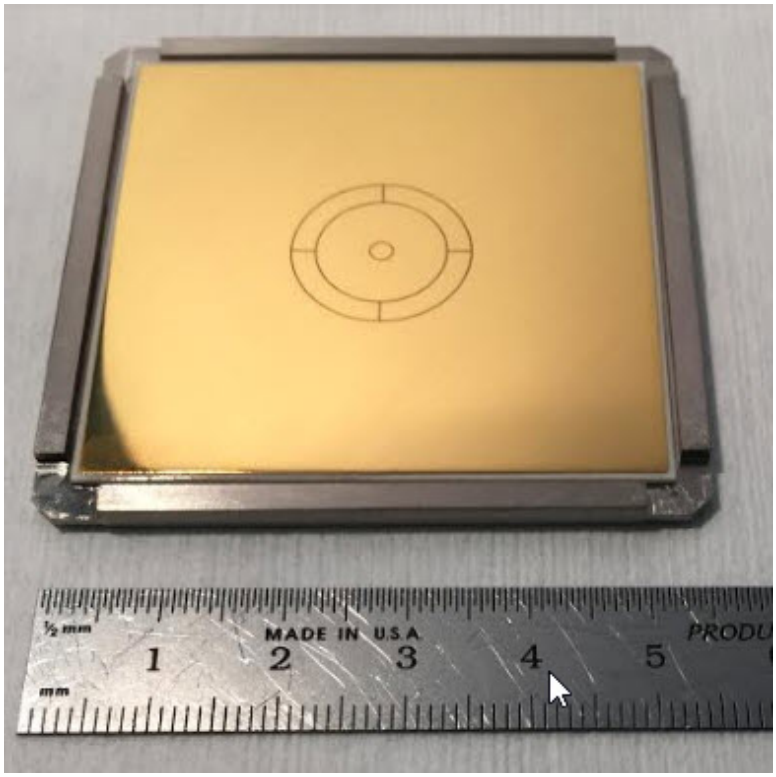

Figure 3.2: Photograph of polished and gold-plated electrode plane secured in titanium retaining frame.

featureless surface on cylindrical electrodes, with a roughness of less than 1 micron, doing so requires the use of sub-micron grit polishing pastes and slurries. These sub-micron polishing products are easily accumulated in the grooves between electrode surfaces and difficult to dislodge, and so were not used here.

In addition to the small polishing scratches still visible by eye, there is observed some deformation of the copper plane above the vias that provide electrical connection on the back side of the plane. The deformation is due to thermal cycling and can be explained by the poorly matched thermal expansion properties of copper and alumina. For temperature transitions from room temperature to 4 K, $\Delta L/L = 0.3\%$ for copper and 0.08% for single-crystal alumina [61]. A photograph of a test plane illustrating an area of deformation is shown in Fig. 3.3. The test plane was thermally cycled from room temperature to 77 K and back to room temperature by dipping in and out of liquid nitrogen prior to imaging. An indentation above the via, roughly the same size as the 3 mm via, is indicated. The areas of deformation are not symmetric on the plane, as the cupping shape of the deformation is randomly concave or convex.

After gold-plating, the leakage resistances between adjacent electrodes are measured to ensure adequate electrical isolation. Leakage resistance is measured with a Kiethley model 6517B electrometer, which applies a test voltage of 400V, larger by nearly a factor of 4 than bias voltages under normal operating conditions, and can detect currents as low as 20 pA. All adjacent electrodes show a leakage resistance of greater than 10 TΩ. The capacitance between electrodes is also measured, using a TEGAM model 252 LCR meter. The capacitance between the central electrode (e1) and the first outer ring electrode (e2) is measured as 2.2 pF with an accuracy

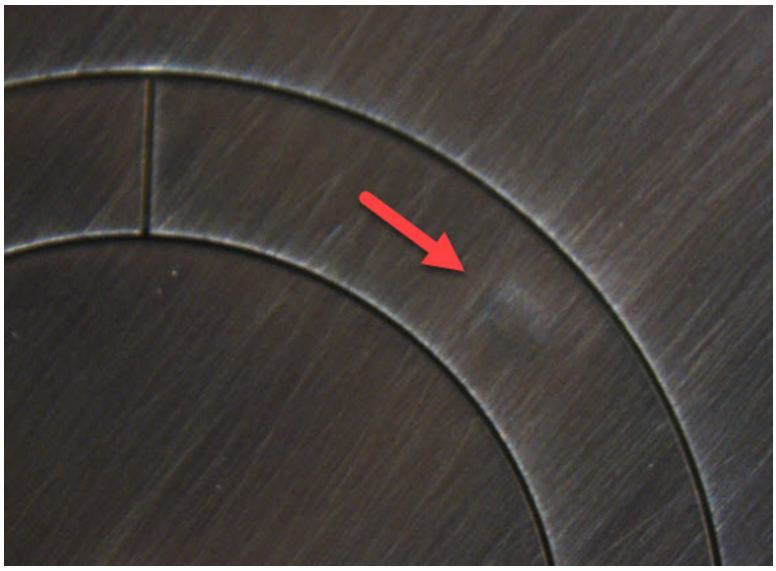

Figure 3.3: Photograph of test plane with area of deformation indicated. The surface of the test plane has not been polished. The test plane was thermally cycled in liquid nitrogen before imaging.

of 0.25%. As required, this is a fraction of the total capacitance relevant to electron detection, which is dominated by the stray capacitance of the circuitry, discussed further in section 6.1.

Finally, the depth-to-width aspect ratio of the gap between electrodes is measured. The final thickness of the alumina-copper-gold substrate that forms the finished electrode plane is measured with a Mitutoyo digital micrometer to be 740 μm with a 1 μm accuracy. The barrel of the micrometer contacts the substrate at the far corner, which is contained within the retaining flange once assembly is complete, so that the crucial center surfaces are not marred. In calculating an aspect ratio, we assume the substrate is uniform in thickness. Subtracting the nominal 635 μm thickness of the alumina layer leaves a gap depth of 105 μm. The width of the gap is measured with a compound optical microscope to be 70 μm at the bottom of the gap and 110 μm

at the top [9]. Using the average width, an aspect ratio of 1.2 is reported. This is 3.4 times the aspect ratio of 0.35 reported for the planar Penning trap operated at Ulm in 2008 [7]. An improved aspect ratio in this work is intended to screen charges on the insulating layer that may have contributed to the broad spread in frequencies observed at Ulm.

3.2 Planar Trap Assembly

The full planar Penning trap assembly is illustrated in Fig. 3.4. The polished and gold-plated electrode plane is attached to a titanium frame, as shown in Fig. 3.2, by a small bead of STYCAST 1266 epoxy in one corner of the exposed alumina on the back side of the substrate. The epoxy is formulated to meet the cryogenic requirements; one small bead is used to prevent the substrate from distorting as it is cooled. The frame is then centered in its titanium retaining flange by eye, using a mounted microscope reticle to view the plane and a translation stage to position it. Once positioned, the sandwich flange is tightened to secure the frame in its centered location. Pressure is applied to the frame rather than the electrode plane to avoid distorting or damaging the substrate. The titanium cylindrical enclosure is press-fitted to the flange as shown. The grounded enclosure is made as large as the experimental space constraints allow, and acts as the electrostatic boundary for the trapping potential. The interior walls of the enclosure are polished to a surface roughness of 1 μm [9]. The field emission point assembly, discussed in the following section, is mounted. Finally, to secure the assembly, three threaded molybdenum rods are used to fasten the upper flange to the lower, electrode flange. At each fastening nut, a hand-wound tungsten spring is

compressed, as pictured; as the assembly is cooled to milliKelvin temperatures, the springs ensure that the assembly remains rigid despite thermal contraction.

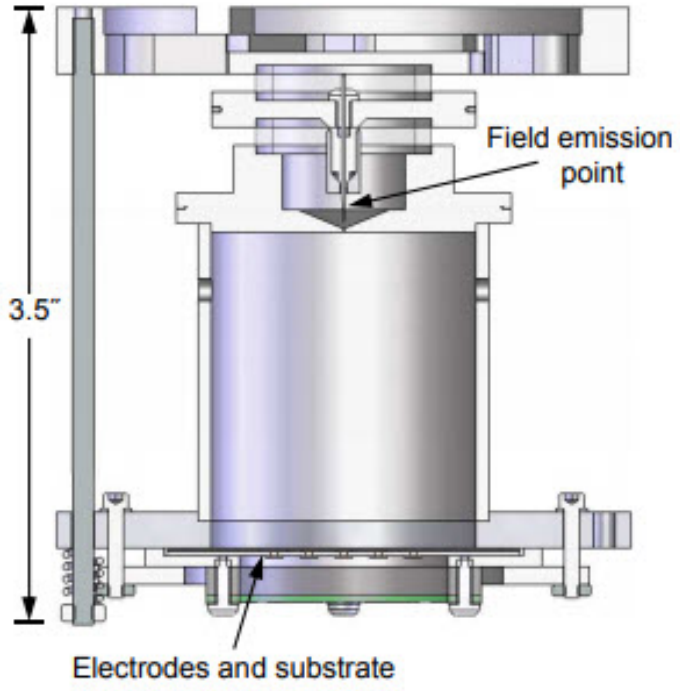

Figure 3.4: Assembly drawing of planar Penning trap. The electrode plane is shown secured within a titanium flange and enclosed by a grounded titanium cylinder. The field emission point is fired to introduce electrons into the trapping region.

The polished and gold-plated electrode plane, secured in the retaining flange, is pictured in Fig. 3.5. The assembled trap is pictured in Fig. 3.6. The trap has been inverted to show the bottom of the electrode plane and electrical connections. Electrical connections are made via high-purity silver straps and lead-tin solder. Silver wires are oven-brazed to all titanium parts to provide for solid RF grounding.

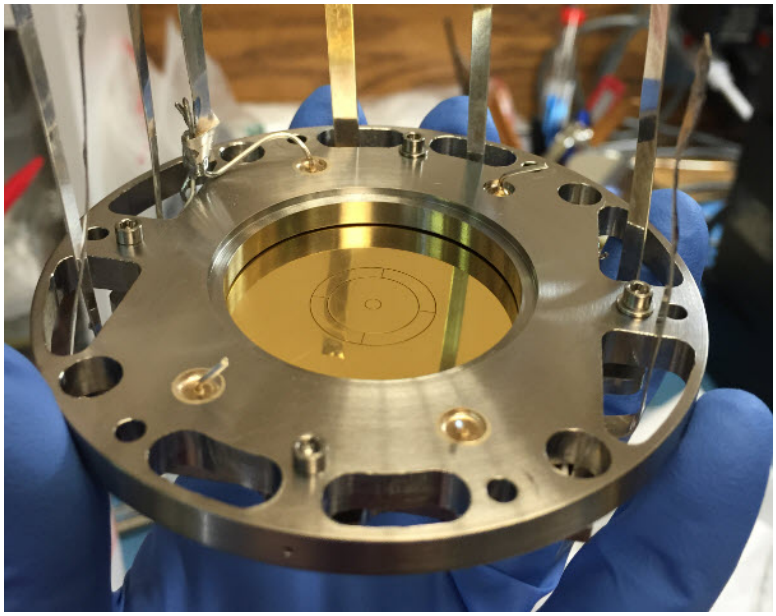

Figure 3.5: Photograph of polished and gold-plated electrode plane secured in titanium retaining flange.

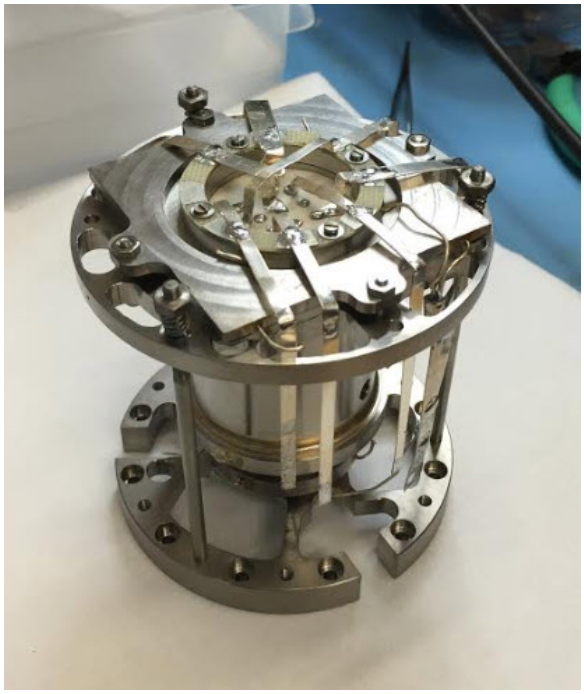

Figure 3.6: Photograph of planar Penning trap assembly. The trap is inverted to show the electrode plane electrical contacts.

3.3 Field Emission Point

The field emission point (FEP), mounted opposite the electrode plane as shown in Fig. 3.4, serves as a reliable electron beam source. It is fabricated by electrochemically etching high-purity tungsten wire to an atomically sharp tip in a sodium hydroxide solution by the lamella drop-off method [16, 62]. A high negative voltage forces energetic electrons from the tip, which follow magnetic field lines toward the electrode plane. Collisions with the plane release adsorbed gas molecules and produce secondary electrons that are collected in the trapping potential. The tungsten tip is secured in a titanium collet, which is in turn secured by a set bolt to the FEP flange. The FEP and its flange are electrically isolated from the rest of the trap assembly by spacers made of alumina.

3.4 Trap Vacuum Enclosure

The planar Penning trap operates in tandem with the cylindrical traps of the lepton magnetic moment experiment, whose goal it is to improve on measurements of the magnetic moments of the electron and positron [63]. An assembly drawing is shown in Fig. 3.7. The planar Penning trap assembly is bolted rigidly to the lepton magnetic moment experiment experiment with titanium screws. The CP-2 titanium trap can serves as the vacuum enclosure for both experiments and is sealed to the pinbase with compressed 2 mm indium wire. The trap can is pumped out through the copper pump-out port at room temperature to a pressure of roughly 10^{-7} torr and then sealed by the pinch-off method. Upon cooling to 100 mK, the vacuum space

is further cryo-pumped to a pressure less than 5×10^{-17} torr, which was measured at 4.2 K for a similar vacuum configuration [64]. Low pressures are required to prevent electron collisions that would limit trap lifetime. The pinbase is a titanium flange containing vacuum-sealed electrical feedthrough pins for electrode and FEP biasing, and RF electron detection. A photograph of the traps prior to enclosure with electrical connections made is shown in Fig. 3.8. Electrical connections are made via high-purity silver straps. The trap can and pinbase bolt to a gold-plated, silver "tripod" extension, whose length positions the traps in the magnetic field and provides space for electronics, such as the cryogenic amplifiers shown and discussed in detail in section 4.6.

3.5 Dilution Refrigerator and Magnet

The silver tripod extension is mounted to the mixing chamber of a $^3He - ^4He$ dilution refrigerator. An illustration of the full apparatus is shown in Fig. 3.9. The inner vacuum chamber (IVC) is assembled and vacuum sealed to house the traps within their trap can and the cryogenic electronics contained within the tripod and the various stages of the dilution refrigerator. The dilution refrigerator and IVC are then inserted into the 4.2 K bore of a liquid helium dewar built to contain a 6 T superconducting magnet, which provides the uniform magnetic field of the Penning trap.

The dilution refrigerator is a custom model JDR-500 fabricated by Janis Research Company, Inc. The dilution refrigerator is designed to achieve temperatures as low as 15 mK with no heat load; our target operating temperature is 100 mK.

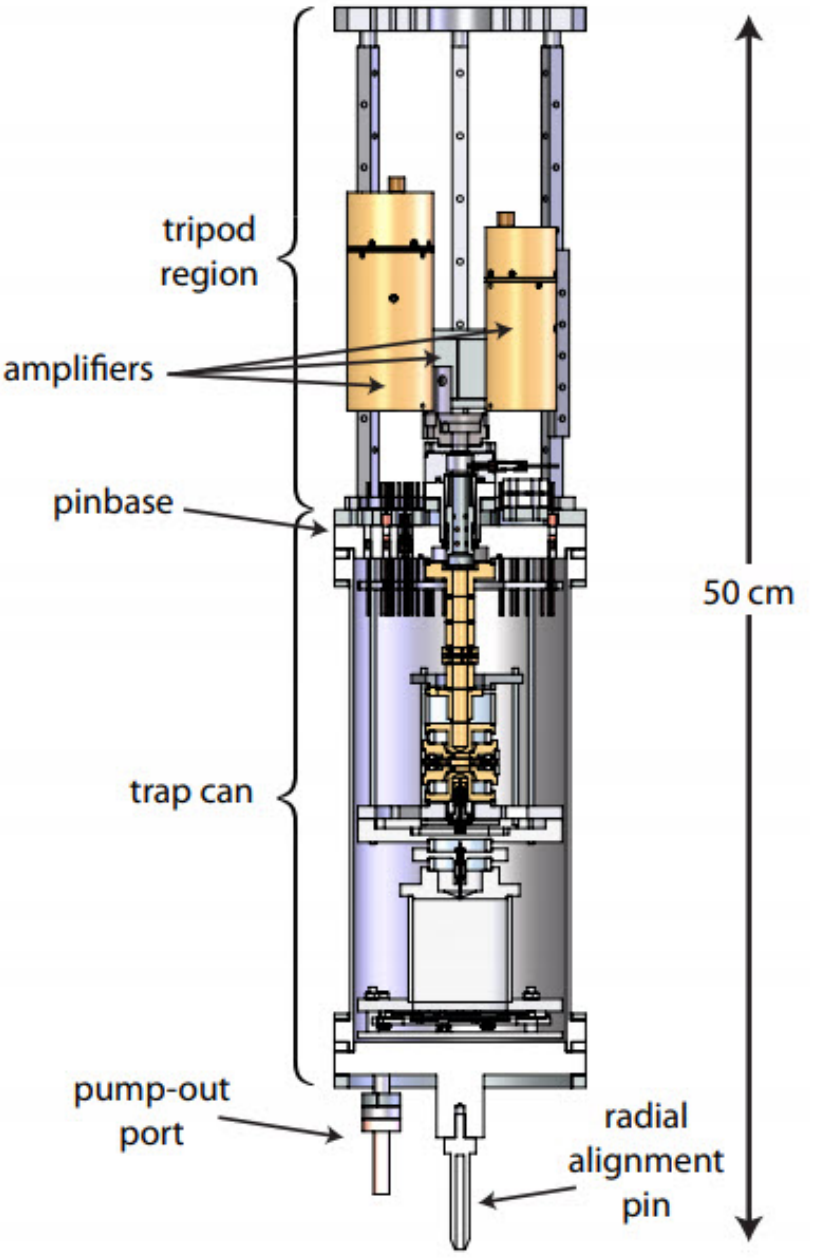

Figure 3.7: Assembly drawing of the planar Penning trap bolted below the cylindrical precision and loading Penning traps of the LeptonCPT experiment. The titanium trap can vacuum enclosure is sealed to the pinbase with compressed indium wire. The gold-plated, silver tripod provides room for electronics, such as the cryogenic amplifiers shown. The tripod bolts to the mixing chamber of a dilution refrigerator.

Figure 3.8: Photograph of planar Penning trap bolted below the LeptonCPT experiment. Electrical connections are made between electrodes and FEPs and the hermetically-sealed electrical feedthroughs of the pinbase via high-purity silver straps.

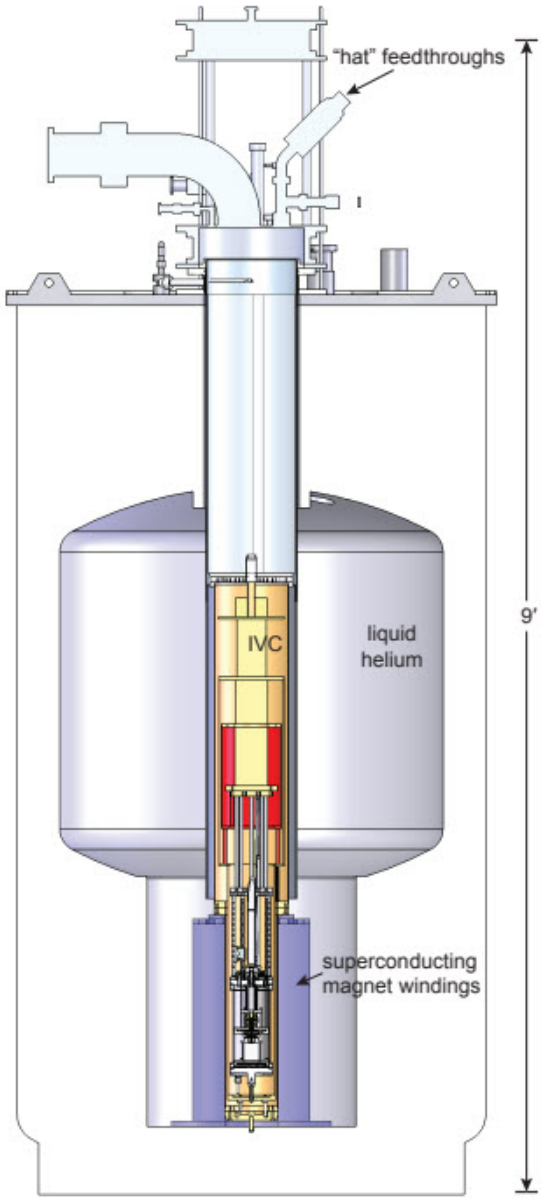

Figure 3.9: Illustration of the full experimental apparatus. The planar Penning trap is mounted to the mixing chamber of a $^3He - ^4He$ dilution refrigerator. An inner vacuum chamber (IVC) contains the trapping experiments and their associated cryogenic electronics. The dilution refrigerator and IVC are inserted into the 4.2 K bore of the liquid helium dewar that houses a 6 T superconductiong magnet.

At 100 mK, the refrigerator has roughly 300 μW of cooling power. To minimize heat load, heat-conductive paths via electrical connections from the room temperature "hat" have been kept to a minimum. DC biasing is made via 0.003" diameter teflon-coated constantan wiring, while AC drives and detection are carried out via microcoax cables with 0.034" diameter stainless steel outer conductor and 0.008" diameter stainless steel inner conductor. Both constantan and stainless steel are chosen for low-thermally-conductive and non-magnetic properties. In addition, both AC and DC wiring are heat-sunk at each temperature stage of the dilution refrigerator. All wires and microcoax cables are wrapped around and epoxied to thermally-anchored copper bobbins at each temperature stage: 4 K plate, 1 K pot, still, intermediate cold plate, and mixing chamber stage. A photograph of the temperature stages of the dilution refrigerator along with the contained electronics is pictured in Fig. 3.10.

The liquid helium dewar, shown in Fig. 3.9, was fabricated by Precision Cryogenic Systems to provide cooling for the superconducting magnet coils while accommodating the dilution refrigerator and traps in the central bore. The 6 T superconducting magnet, also shown, is a Cryomagnetics Inc. model 4983 consisting of a main self-shielding solenoid and twelve additional shim coils. All coils are wound of single-filament, superconducting NbTi wire; once charged, a detachable charging wand is removed, and the magnet is operated in persistent mode. The self-shielding system, developed in our laboratory, improves field stability by using flux conservation to cancel fluctuations in the ambient magnetic field due to external factors, such as ionospheric conditions, solar activity, or proximity to subways [65]. Magnetic field stability is critical to the success of the lepton magnetic moment experiment, for any

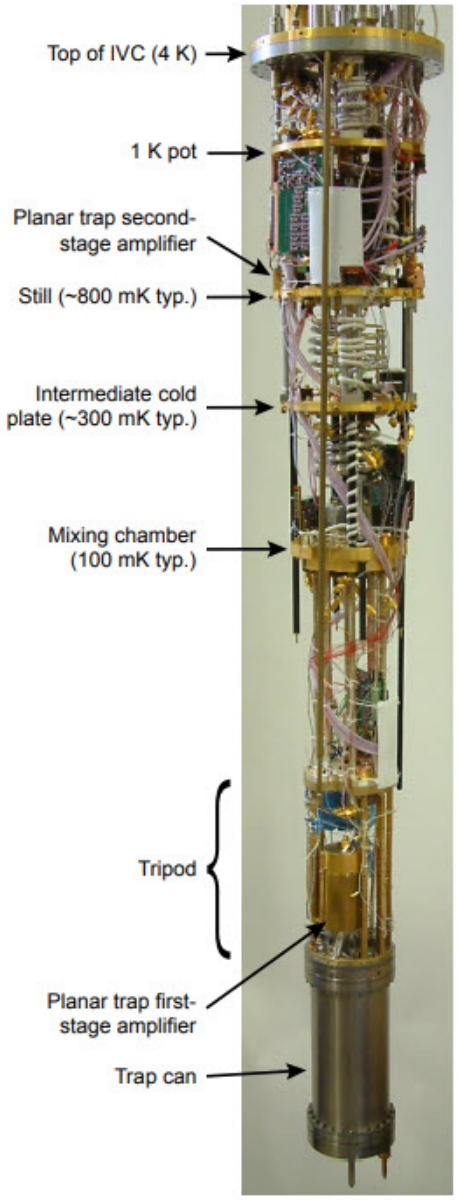

Figure 3.10: Photograph of dilution refrigerator stages contained within the IVC, with temperatures indicated. The first-stage amplifier is housed inside the tripod below the 100 mK mixing chamber stage. The second-stage amplifier is bolted to the 800 mK still plate.

fluctuation in the magnetic field corresponds to a change in the cyclotron frequency. Cryomagnetics has measured the shielding factor to be greater than 1000 [66]. The goal of the present planar Penning trap experiment is to detect only the axial motion of a single electron, not the spin or cyclotron motions, so our magnetic field requirements are not as stringent. The magnetic field serves only to provide radial confinement in the planar Penning trap.

The lepton magnetic moment experiment's precision trap is positioned at the center of the magnetic field because of its strict requirements. The magnet is built such that the field at magnet center can be shimmed to a homogeneity of 1 part in 10^8 over a 1 cm diameter sphere. Radial alignment pins made of PEEK (shown in Figs. 3.7 and 3.9), a thermally-insulating thermoplastic polymer, center the trap can within the IVC; a centering pin on the bottom of the IVC then aligns the experiment radially with the magnet windings. The planar trap experiment, bolted beneath the lepton magnetic moment experiment, is located 4 inches below the magnetic field center. At 4 inches below the field center, the magnetic field is reduced by 3% from 5.18 T to 5.03 T at the planar trap electrodes [9].

3.6 RF Electron Detection Electronics

Detection of an electron in the planar Penning trap relies on the fact that the RF axial oscillatory motion of the confined electron induces an image current in the trap electrodes. This tiny current, on the order of a few hundred femtoamps, is detected by coupling to a tuned circuit [48, 58], which serves as input to several stages of amplifiers. The tuned-circuit scheme is modeled in Fig. 3.11.

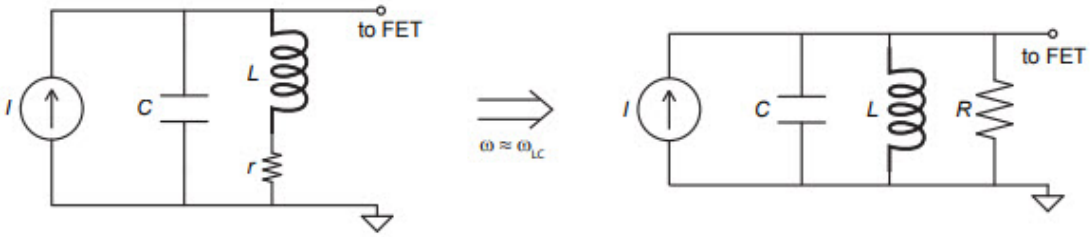

Figure 3.11: Model of tuned-ciruit scheme for electron detection.

The current source with current I models the induced current from the axial motion of the trapped electron as well as the current generated by the thermal Johnson noise in the circuit. The trap capacitance is represented by the capacitor with capacitance C. An inductance, L, is added in parallel with an accompanying residual resistance, r. The value of the inductance is chosen to tune out the trap capacitance such that on resonance, when $\omega_z = 1/\sqrt{LC}$, the inductive reactance cancels the capacitive reactance, and the impedence is fully resistive, given by R. The resistance, R, is related to the trap capacitance and the added inductance by the expression

$$R = L/rC = Q\omega_z L = Q/\omega_z C, \tag{3.1}$$

where Q is the dimensionless quality factor of the tuned circuit.

As discussed in chapter 3, the induced voltage signal is given by

$$V_I = \frac{eD_1}{2\rho_1} R\dot{z}, \tag{3.2}$$

and is proportional to the axial velocity of the oscillating electron, the resistance, R, and the dimensionless factor D_1, which depends on the electrode geometry and z_0.

The induced potential gives rise to a damping force as the electron's axial energy is dissipated in the resistance R, and the trapped electron's axial damping rate is

given by

$$\gamma_z = \left(\frac{eD_1}{2\rho_1}\right)^2 \frac{R}{m} = \left(\frac{eD_1}{2\rho_1}\right)^2 \frac{Q}{m\omega_z C}. \tag{3.3}$$

A high-Q tuned circuit provides for increased R, and, subsequently, improved damping and signal. Of importance in design, then, and to the goal of improving signal-to-noise is to maximize Q while minimizing residual losses and capacitance.

3.6.1 First-Stage Cryogenic Amplifier

The tuned-circuit output is AC-coupled by way of a capacitive divider to a FET-based first-stage amplifier, which resides on the pinbase within the 100 mK tripod stage as pictured in Fig. 3.7. The amplifier schematic is shown in Fig. 3.12. At the heart of the amplifier is a Fujitsu FHX13LG High Electron Mobility Transistor (HEMT). The capacitive divider prevents loading losses by adding to the 100 kΩ input impedance of the HEMT. The values of the capacitors in the divider are kept small to minimize the overall capacitance and maximize Q. Contributions to the capacitance are 1) the capacitance between the central detection electrode and the adjacent, RF grounded electrode, 2) the capacitance of the long silver strap lead from the electrode to the feedthrough pin inside the trap can, as shown in fig. 3.8, 3) the distributed capacitance of the windings of the inductor coil, and 4) the stray capacitance associated with the components on the amplifier circuit board. The trap and lead capacitance is estimated by the amount of capacitance that must be added during amplifier testing on the bench to mock the trap capacitance in order to bring the amplifier resonance to 66 MHz, and is found to be 13.0 ± 0.1 pF. The distributed capacitance of coil and circuit is calculated to be 6.7 ± 0.2 pF, giving a

total capacitance of 19.7 ± 0.3 pF.

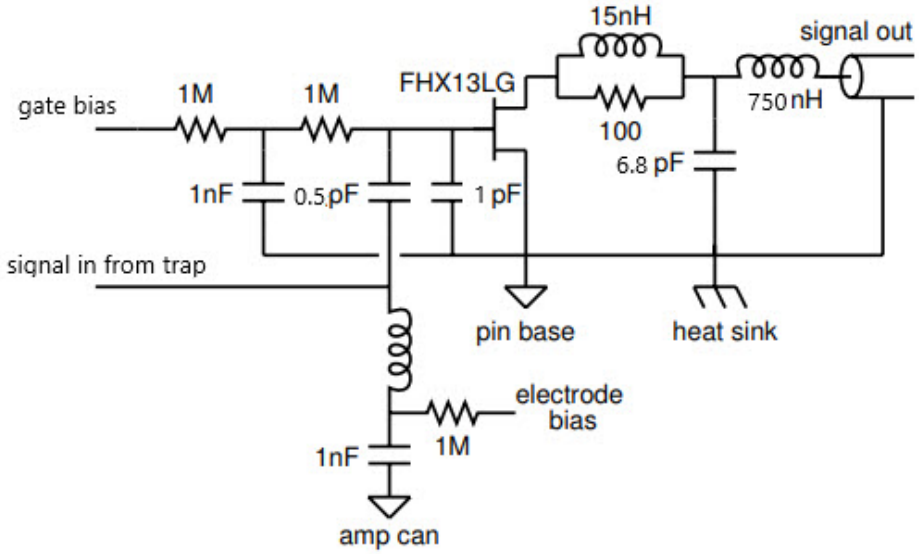

Figure 3.12: Schematic of the first-stage cryogenic amplifier.

The inductor coil in parallel with the trap signal forms the tuned circuit and is hand wound from high-purity silver wire with a 2 mm diameter. Its inductance is chosen to attain a resonant frequency of 64 MHz, convenient for RF detection. At 5.5 turns, 1.25 inches long, with an inner diameter of 0.70 inches, the inductance is measured to be 302 nH. Access is made available for DC biasing the center detection electrode and the HEMT gate. The HEMT drain is DC biased by the same coaxial cable that carries the AC output signal to the next stage of amplification. A suppression circuit at the HEMT drain, consisting of a resistor and inductor in parallel, adds loss at high frequencies and works to prevent oscillations that may render the amplifier unstable. An L-network at the output matches the 1800 Ω output impedance of the HEMT to the 50 Ohm stainless steel coaxial cable for maximum signal transmission.

Figs. 3.13 and 3.14 show the circuit board layout and amplifier construction. The hand-wound inductor is centered in a gold-plated, OFE copper cylindrical enclosure,

designated as the "amp can." The can diameter is maximized for greater Q [67]; the diameter is limited only by the practical matter of space in the tripod region. The circuit board is machine milled from a copper-clad teflon/glass substrate; teflon has a lower dialectric constant and is known to be less lossy at high frequencies than G10. The board is soldered to a copper heat sink, which is bolted directly to the 100 mK tripod stage. As indicated in Fig. 3.13, the HEMT source is in turn soldered directly to the heat sink post. The axial motion of the electron thermalizes with the detection circuit, so adequate heat sinking is crucial for reaching low temperatures. Components are a combination of surface-mount thin metal film resistors, non-magnetic surface-mount inductors, and ATC porcelain microstrip capacitors, and all meet RF and cryogenic requirements.

The amplifier must be carefully tuned to avoid positive feedback that can lead to instabilities and regeneration [16]. This is done by tuning the frequency of the output circuit slightly lower than the frequency of the tuned circuit input, such that the HEMT sees a capacitive rather than an inductive load. Fig. 3.15 shows the reverse reflection off the output network of the amplifier as measured by a network analyzer. The plot, showing gain as a function of frequency, demonstrates good matching at the 64 MHz target axial frequency of the trapped electron, as designed. The input tuned-circuit resonance can be seen to the high frequency side of the output network by several MHz.

Finally, the quality factor Q of the amplifier tuned-circuit is characterized. When there are no electrons present in the trap, the tuned-circuit is driven by the thermal

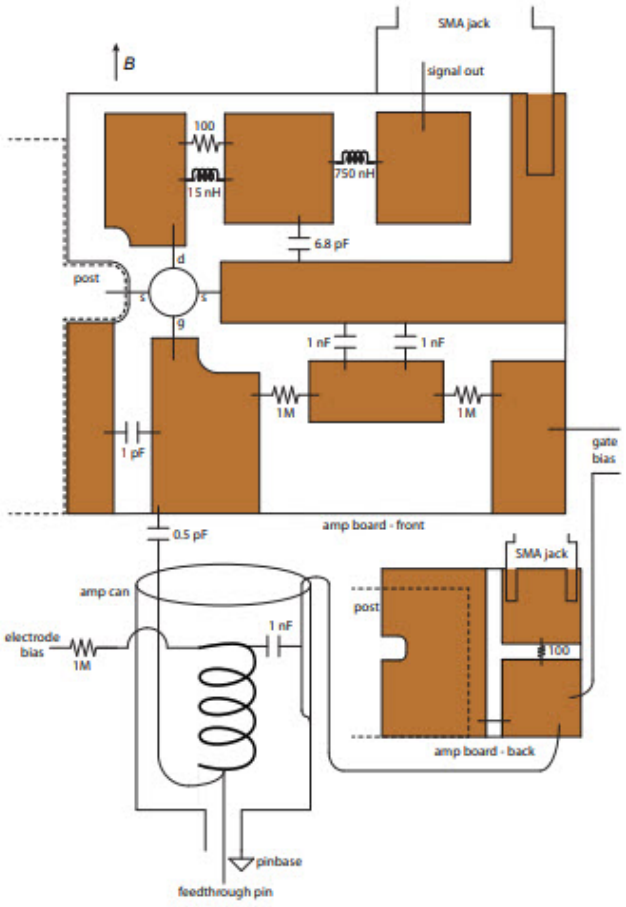

Figure 3.13: First-stage cryogenic amplifier circuit board design.

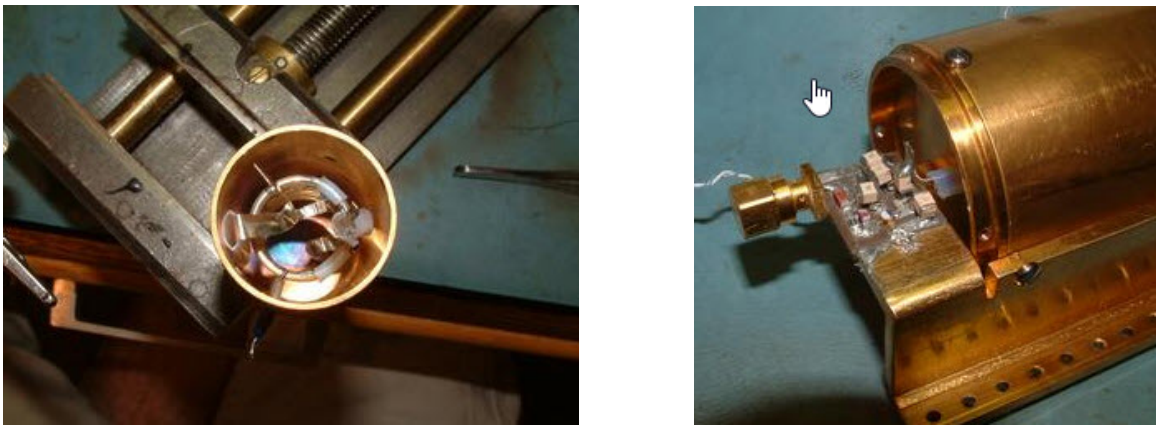

Figure 3.14: Photos of first-stage amplifier construction.

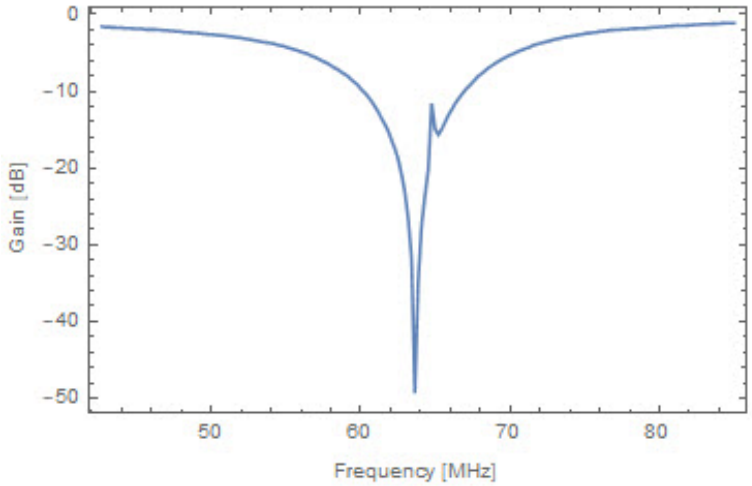

Figure 3.15: Reverse reflection off the output circuit of the first-stage amplifier. The gate is biased to V_g=-0.5 V, and the drain is biased to V_d=1.0 V. The output power is 60 μW.

Johnson noise in the effective resistor, R, producing a voltage given by

$$V_N = \sqrt{4k_B T(\Delta\omega)R}, \tag{3.4}$$

where k_B is the Boltzman constant, T is the temperature of the resonant circuit, and $\Delta\omega$ is the frequency bandwidth. The power dissipated in the circuit impedance, then, is given by $P_{dissipated} = V^2/(ReZ)$, where Z is the complex impedance of the parallel circuit shown in Fig. 3.11. The dissipated power has the form

$$P \propto Re(Z) \approx \frac{R(\Gamma/2)^2}{(\Gamma/2)^2 + (\omega - \omega_{LC})^2}, \tag{3.5}$$

which is the familiar Lorentzian lineshape, where Γ is the full width at half-maximum (FWHM), and the quality factor Q is given by the center frequency divided by the FWHM: $Q = \nu_0/\Gamma$. Note that the Johnson noise signal is proportional to $\sqrt{R}$, and the electron induced signal defined in Eq. 4.2 is proportional to R; therefore, the signal-to-noise relevant to detection goes as $\sqrt{R}$. Large R, and large Q, then, is

critical to good detection, as is consistent with the discussion above.

The Johnson noise resonance of the first-stage, tuned-circuit amplifier at a temperature of 100 mK is shown in Fig. 3.16. The fit to the Lorentzian lineshape is shown in red. The Q, given by the fit parameters ν_0 and Γ, is 1707. Previous efforts with this apparatus reported a first-stage amplifier Q of 1200 at 4K in a test dewar with an ATC capacitor serving at a mock trap capacitance and roughly 400 on the experiment at mK temperatures [9]. The Q reported here demonstrates a significant improvement in detection sensitivity.

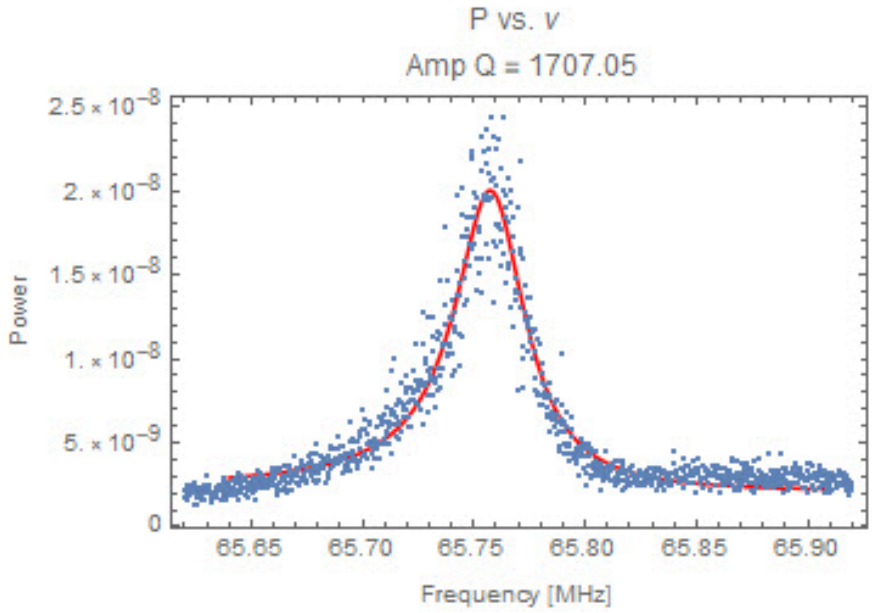

Figure 3.16: Johnson noise resonance of the first-stage, tuned-circuit amplifier at 100 mK. No electrons are present in the trap. The fit to the Lorentzian lineshape is shown in red. The Q, given by the fit parameters, is 1707.

3.6.2 Second-Stage Cryogenic Amplifier

The output signal from the first-stage amplifier travels via stainless steel micro-coaxial cable to a second-stage cryogenic amplifier, which is located at the 800 mK still stage of the dilution refrigerator as indicated in Fig. 3.10. The second-stage amplifier provides additional gain while maintaining a low noise temperature.

The previous second-stage amplifier relied on positive feedback to generate the needed gain at the expense of stability and reliability [9]. Here, a new design of a 64 MHz second-stage amplifier is reported that draws on the development of the lepton magnetic moment experiment's 200 MHz second-stage amplifier and employs negative feedback for greater stability [16]. The new second-stage amplifier schematic is shown in Fig. 3.17. Like the first-stage amplifier, the second-stage amplifier is built on a Fujitsu FHX13LG HEMT. At the input, access is made for biasing the HEMT gate as well as the first-stage amplifier HEMT drain. Matching networks at the input and output of the HEMT transform the impedances for optimum signal transmission. At the front end, the matching network matches the 50-Ohm impedance of the micro-coaxial cable from the first-stage amplifier to the 100 kΩ input impedance of the HEMT. At the output, the matching network matches the 1800 kΩ output impedance of the HEMT to the 50-Ohm impedance of the micro coaxial cable that carries the amplified signal to the room temperature for further amplification. A suppression circuit on the output works to suppress oscillations at high frequencies for stability.

The constructed second-stage amplifier is imaged in Fig. 3.18. As with the first-stage amplifier, the circuit board is machine milled on a computer numerically controlled (CNC) mill from copper-clad teflon/glass substrate. The board is soldered to

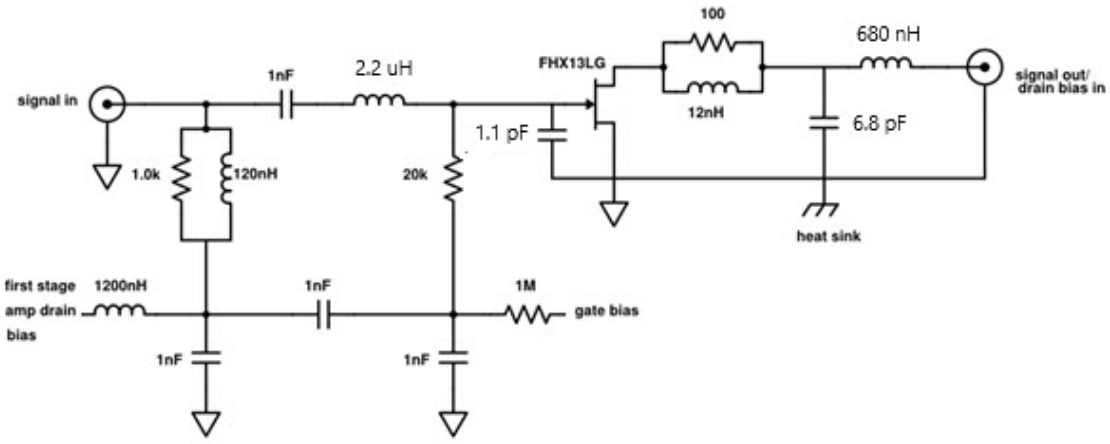

Figure 3.17: A schematic of the second-stage cryogenic amplifier.

the copper heat sink, and the source lead of the HEMT is soldered directly to the sink. The heat sink is then bolted firmly to the still plate of the dilution refrigerator for robust heat sinking. SMA connectors are soldered to the board to make for good connection to the stainless steel micro-coaxial cables that carry the signal both in and out of the amplifier. All components are surface-mount and suitable for RF operation and the cryogenic environment, and consist of thin metal film resistors, NPO ceramic capacitors, and nonmagnetic wire-wound inductors.

The amplifier is carefully tuned to avoid positive feedback that can lead to instabilities and regeneration. The strategy is the same as is employed with the first-stage amplifier. The frequency response of the output circuit is tuned slightly lower than the frequency of the input circuit, such that the HEMT sees a capacitive rather than an inductive load. Fig. 3.19 shows the reflection and gain responses as measured by a network analyzer. Clockwise, from top left, are plots of the 1) the forward reflection, 2) the reverse reflection, 3) the forward gain, and 4) the reverse gain. It is shown that the output network is tuned to the low frequency side of the input network by several

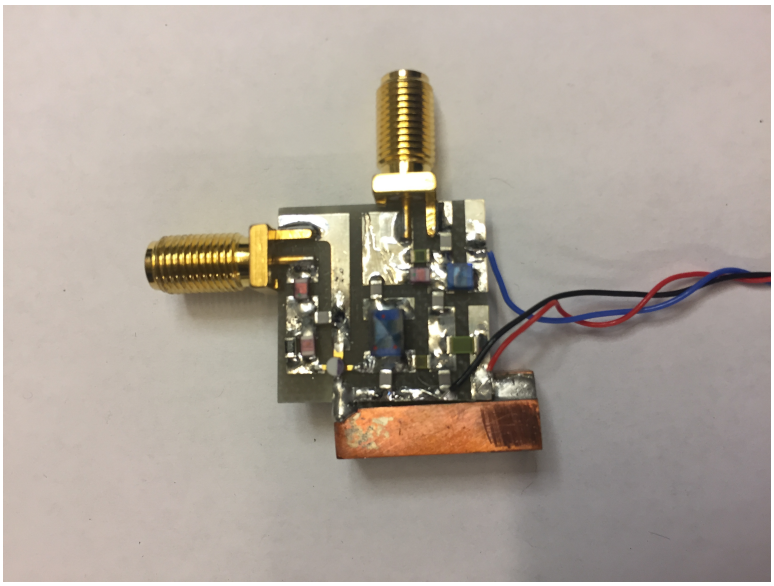

Figure 3.18: Photograph of second-stage cryogenic amplifier.

MHz.The reflection plots show good matching at the desired frequency. The reverse gain plot indicates good suppression of noise that may potentially travel from room temperature toward the trap and cause heating of the trapped electron. The forward gain plot shows good gain, with 25 dB of amplification at the desired frequency. This is a factor of two improvement in gain over the previous second-stage amplifier.

In fig. 3.20, the second-stage amplifier resonance is visible as a broader peak on which the narrower first-stage amplifier resonance rests. There are no electrons present; the resonances are driven by the thermal Johnson noise in the circuits. The plot shows adequate tuning such that the amplifiers resonances coincide sufficiently to take full advantage of the added gain.

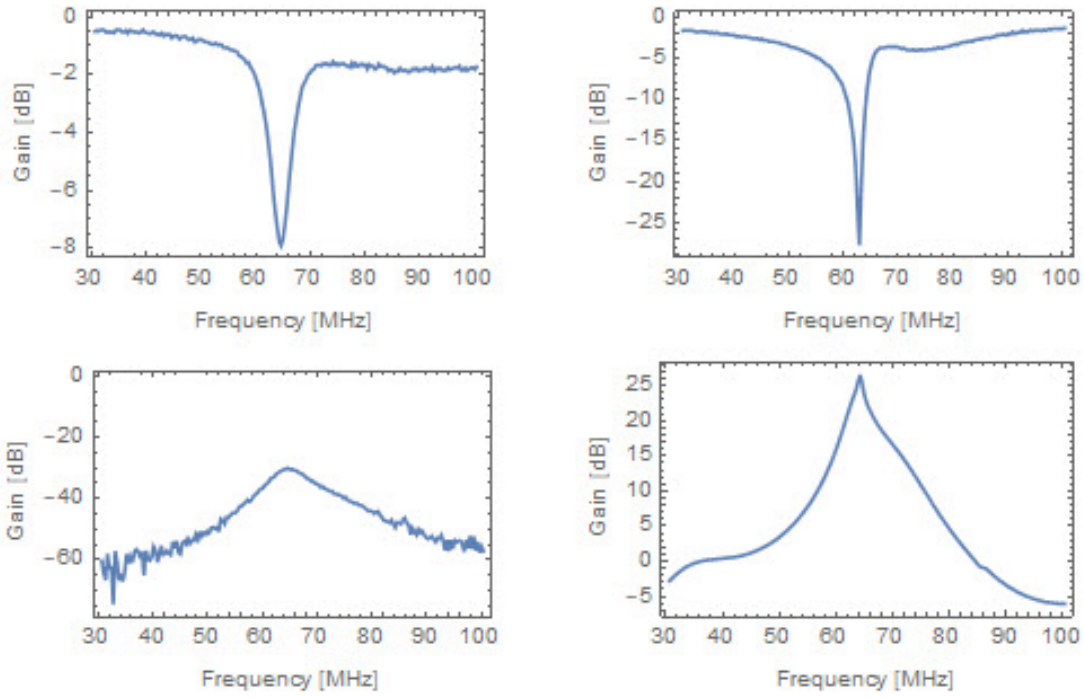

Figure 3.19: The second-stage amplifier reflection and gain responses as measured by a network analyzer. Clockwise, from top left: 1) the forward reflection, 2) the reverse reflection, 3) the forward gain, and 4) the reverse gain.

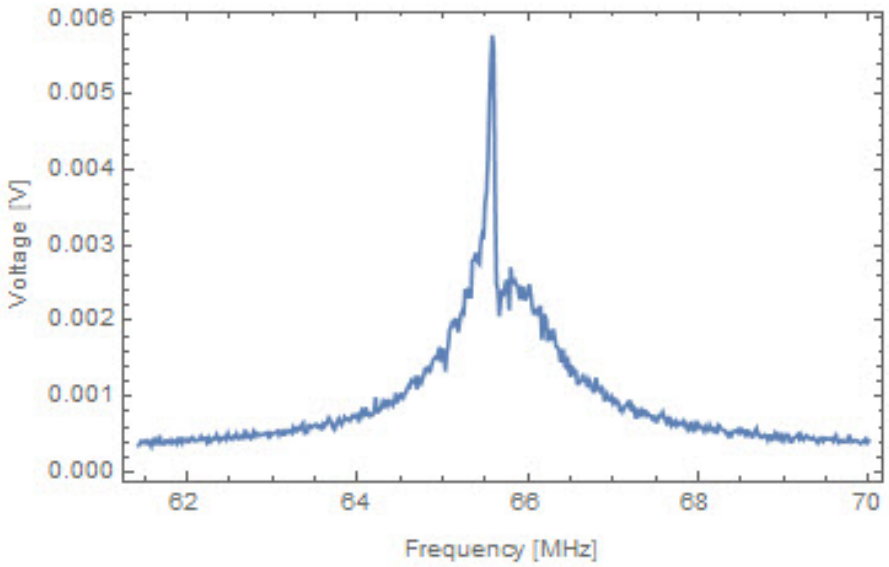

Figure 3.20: The narrower first-stage amplifier resonance visible on top of the broader second-stage amplifier resonance. No electrons are present in the trap; the resonances are driven by the thermal Johnson noise in the circuits.

3.6.3 Room temperature Amplifiers and Electronics

The signal is carried from the second-stage cryogenic amplifier via stainless steel micro-coaxial cable through the upper stages of the dilution refrigerator and to the hat at the dewar top and its room temperature hermetic feedthroughs. External to the dilution refrigerator and hat, the signal is filtered and guided through three room-temperature MITEQ amplifiers (AU-2A-0110-BNC), each with a maximum gain of 34 dB and noise figure of 1.2, and an attenuator that is varied to prevent saturation, before being directed to an Agilent 8564EC spectrum analyzer for imaging. The full detection scheme is pictured in the wiring diagram in Fig. 3.21. The spectrum analyzer is paired with a computer via GPIB connection for automated data collection and storage.

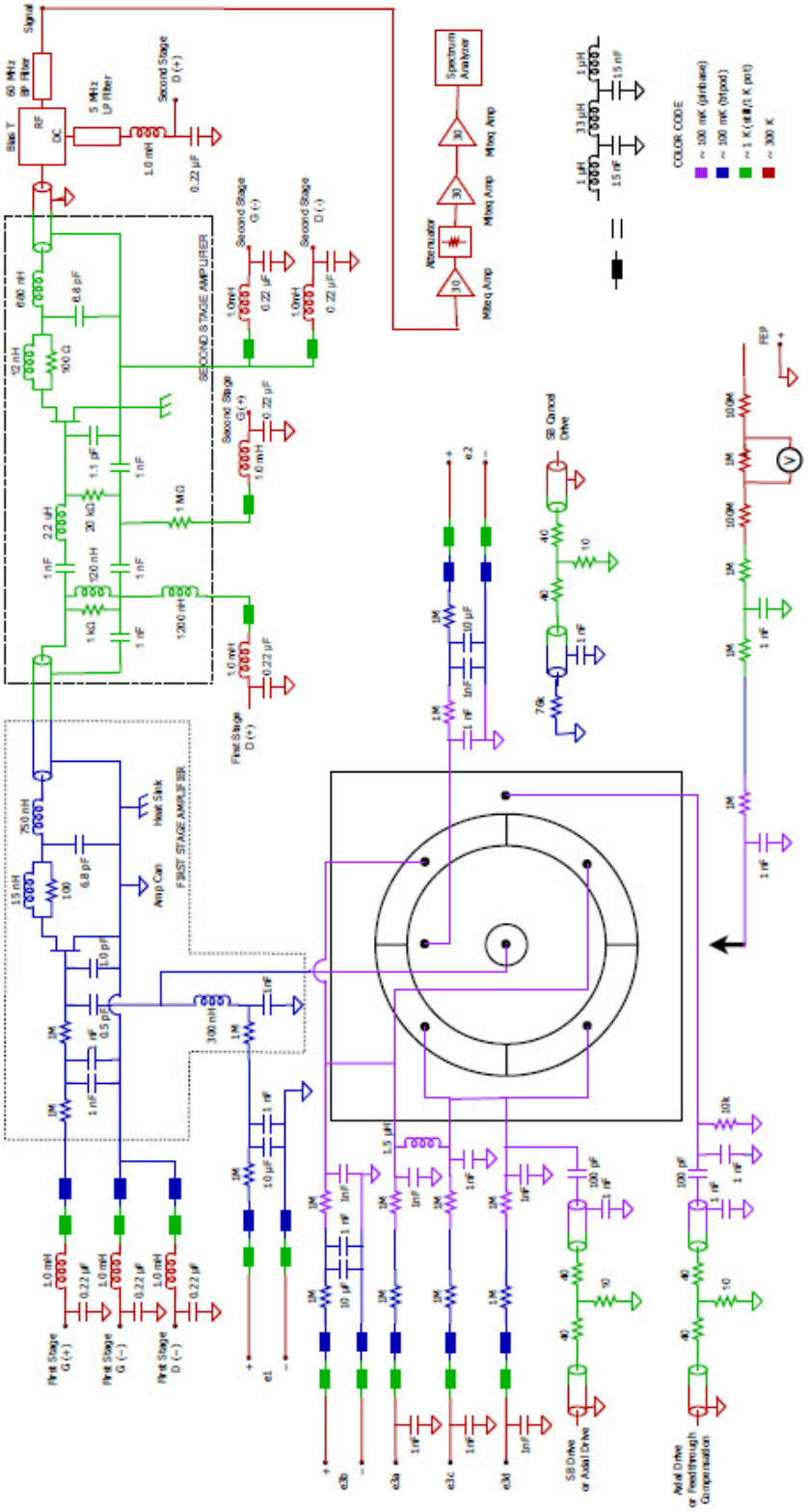

Figure 3.21: Full planar Penning trap experiment wiring diagram.

Chapter 4

Electron Loading and Detection

4.1 Electrode biasing

In preparation for loading electrons into the trap, the electrodes are biased to produce the trapping potential. Detection of a single electron requires a highly stable axial frequency; therefore, great care is taken to supply correspondingly stable bias voltages. Bias voltages for the three electrodes are supplied by high-stability Fluke 5440B calibrators, precise to within 1 μV. The voltages are carried to the electrodes via twisted wire pairs and several stages of filtering. The twisted pairs are of standard gauge until reaching the hermetically-sealed lemo connections on the room-temperature side of the dilution refrigerator. To minimize heat load, 0.003 inch diameter, low-thermally-conductive constantan wire pairs carry the bias voltages between the stages of the dilution refrigerator to the trap can pinbase. The lines pass through LC filters at both the 1K pot and mixing chamber stages. At the mixing chamber, within the tripod region, the bias lines pass through low-pass RC filters

with large 10 μF polypropylene capacitors with a time constant of 10 seconds for added stability. Finally, at the pinbase, 1 nF bypass capacitors provide an AC path to ground at the feedthrough pin to the trap can vacuum space. Within the trap can, the bias voltages travel via 3-5 mm wide, low-inductance, high-purity silver straps to each electrode contact.

Previous efforts with this apparatus [9] began with the optimized biases given in Chapter 3, then proceeded with adjustments dictated by *in situ* anharmonicity tuning (discussed in section 5.5), which take into consideration the as-built trap dimensions; that is, the laboratory trap has gaps between electrodes, finite boundaries, and imperfect electrode surfaces, and the optimized bias voltages are adjusted to accommodate these realities. This study picks up where the former study left off. Table 4.1 summarizes the final trap biases, scaled so that the electron axial frequency is $\nu_z = 65.76$ MHz, as well as the calculated values of the scaling potential, V_0, the potential minimum, z_0, and the trap depth. The potential on the $\rho = 0$ axis is shown in fig. 4.1.

V_1	28.963024 V
V_2	29.428550 V
V_3	126.083300 V
V_0	-1.07014 V
$\omega_z/2\pi$	65.76 MHz
z_0	1.57 mm
Trap depth	1 V

Table 4.1: The final trap bias voltages, scaled such that the electron axial frequency coincides with the center of the detection amplifier resonance. The voltages, supplied by high-stability Fluke calibrators, are precise to 1 μV. The potential minimum, z_0, and the trap depth are calculated.

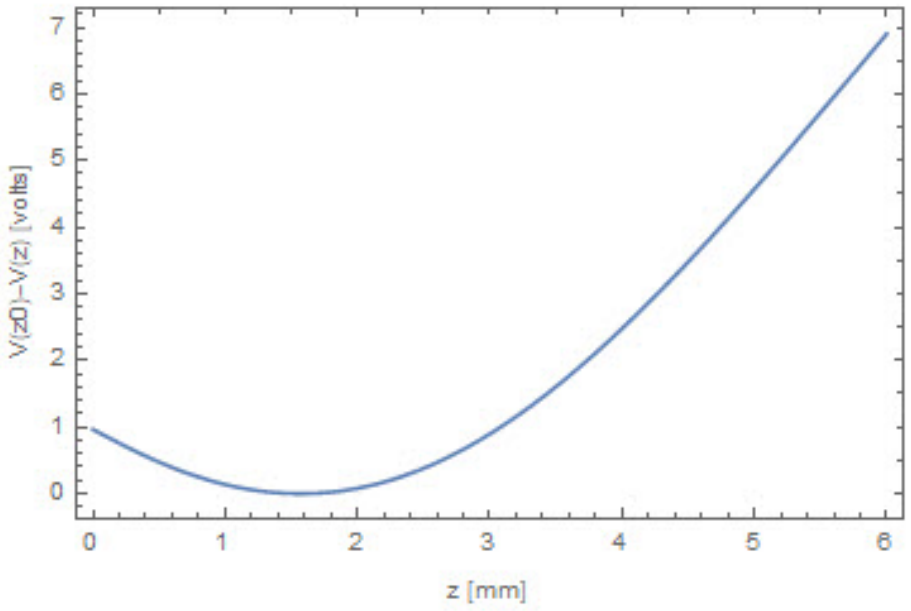

Figure 4.1: Trapping potential on axis. The trap depth is 1 V, and the potential minimum is at z_0=1.57 mm.

To adjust the axial frequency at which the electrons oscillate, the voltages are scaled together to preserve the quadrupole potential and hold the potential minimum z_0 constant.

4.2 Loading electrons: Firing the Field Emission Point

Electrons are loaded into the trapping potential by firing the field emission point (FEP). The FEP is fired by applying a high negative voltage, on the order of hundreds of volts, producing a beam of energetic electrons that follow the magnetic field lines toward the electrode plane. At the plane, the electrons collide with the surface and release adsorbed gas molecules, which are cryo-pumped to the surface during cool-down. Collisions with these residual gas molecules result in slow electrons that are

collected in the trapping potential well.

The FEP firing current is monitored as a voltage drop across a 1 MΩ resistor, shown in series with the FEP in fig. 3.21, with a Fluke 8846A precision multimeter. The firing currents, typically on the order of tens of picoamps, vary depending on the voltage applied and the sharpness of the etched tip. A representative firing curve is shown in fig. 4.2. The current in the monitoring resistor is initially large as the FEP charges, then once the FEP fires, stabilizes at a low persistent value, here ∼20 pA. The loading rate is roughly linear with time after an initial 20 seconds. For -93 V applied to the planar Penning trap FEP for 60 s, 1-3 electrons are loaded.

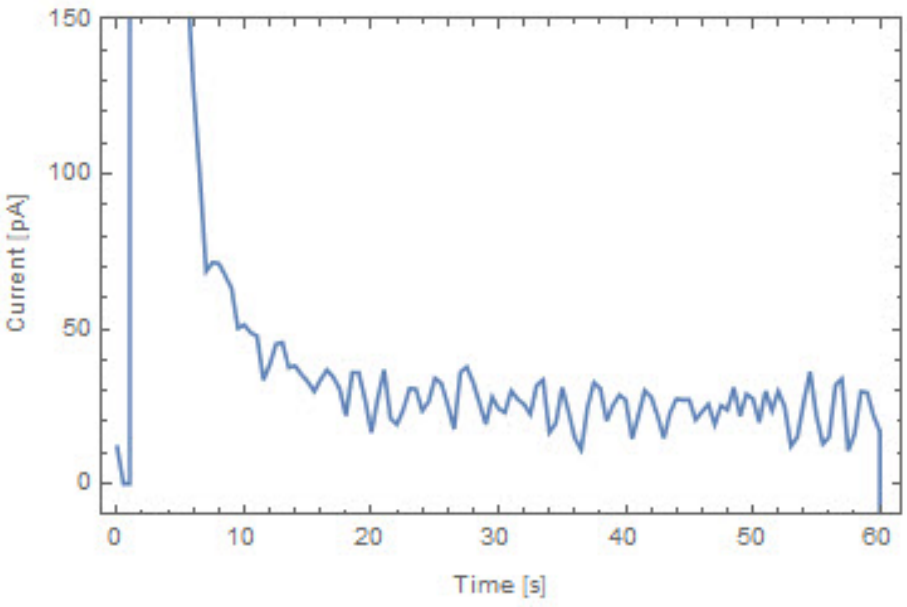

Figure 4.2: A representative FEP firing curve. The current in the monitoring resistor is initially large as the FEP charges, then once the FEP fires, stabilizes at a low persistent value, here ∼ 20 pA. For -93 V applied to the FEP for 60 s, 1-3 electrons typically load.

Between the loading of each successively smaller electron cloud, the trap is emptied by dumping the confined electrons. The dump procedure involves biasing all

three electrodes to -10 V, which creates a potential hill that ejects the electrons from the trapping region, along the magnetic field lines, and toward the grounded trap enclosure. The potential is then re-established and the trap ready for loading.

4.3 Detecting the Electron Axial Motion: Observing Dips

Once electrons are loaded into the trap, the electron axial motion is detected by employing the tuned-circuit amplifier scheme described in detail in chapter 4. The amplifier resonance in the absence of electrons is pictured in fig. 3.16, driven by thermal Johnson noise in the detection circuit resistance. When electrons are present in the trap, they short the Johnson noise, and the electron signal appears as a dip in the noise resonance at the axial frequency of the electrons, ω_z. The scheme is modeled in fig. 4.3 and discussed in detail in refs. [68] and [69]. A brief discussion is included here.

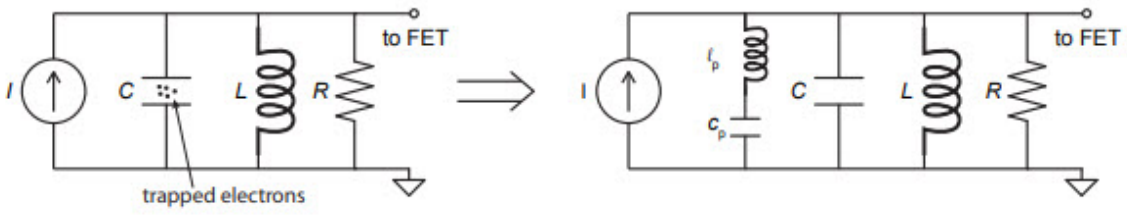

Figure 4.3: The equivalent circuit model for electrons confined in the trap and represented by an inductance, l_p, and a capacitance, c_p. The electrons are coupled to the RLC tuned-circuit of fig. 3.11 such that at $\omega = \omega_z = \sqrt{l_p c_p}$, the electrons short the thermal Johnson noise. Fig. taken from [9].

A cloud of N confined electrons are represented by an inductance, l_p, and a ca-

pacitance, c_p. The equation of motion for the center of mass of N electrons between two plates of a capacitor gives the expressions

$$l_p = \frac{m}{N}\left(\frac{2\rho_1}{qD_1}\right)^2 = \frac{R}{N\gamma_z} \tag{4.1}$$

$$c_p = \frac{N}{l_p\omega_z^2} \tag{4.2}$$

where R is the effective resistance of the tuned circuit and γ_z is the single-electron damping rate. In section 3.6.1, the power dissipated in the complex impedance of the parallel circuit when no electrons are present was shown to have a Lorentzian lineshape; for $\omega \approx \omega_{LC}$, with no electrons present, it is written as the square of the induced voltage drop

$$|V(\omega)|^2 = \frac{|V_N|^2 Q^2 (\Gamma/2)^2}{(\omega_{LC}-\omega)^2 + (\Gamma/2)^2}, \tag{4.3}$$

where $|V_N|^2 = 4k_B T(\Delta\omega)R$ is the thermal Johnson noise at temperature T, Q is the quality factor, and Γ is the full width at half maximum (FWHM) of the resonant signal. When electrons are present in the trap, the expression becomes [70]

$$|V(\omega)|^2 = \frac{|V_N|^2 \omega_{LC}^4 (\omega_z^2-\omega^2)^2}{\left[(\omega_z^2-\omega^2)(\omega_{LC}^2-\omega^2) - \omega^2\Gamma N\gamma_z\right]^2 + \omega^2\Gamma^2\left[(\omega_z^2-\omega^2) + \Gamma N\gamma_z\right]^2} \tag{4.4}$$

where again, ω_z is the electron axial frequency, which is not necessarily the same as the tuned-circuit resonant frequency, ω_{LC}, and γ_z is the single-electron damping rate. In the limit of small N, where $N\gamma_z << \Gamma$, and for the case of $\omega_z = \omega_{LC}$, the expression is reduced to

$$|V(\omega)|^2 \propto |V_N|^2\left[1 - \frac{(N\gamma_z/2)^2}{(\omega_z-\omega)^2 + (N\gamma_z/2)^2}\right] \tag{4.5}$$

near resonance. This expression describes a Lorentzian noise signal with an inverted Lorentzian "dip" at the axial frequency of the trapped electrons. The FWHM of the

dip is given by the number of electrons and the single-electron damping rate, $N\gamma_z$. Examples, imaged with a spectrum analyzer, of dips of varying widths are shown in Fig. 4.4, corresponding to clouds of varying numbers of electrons. The dip width, known as the axial linewidth, determines the number of trapped electrons, given the single-electron damping rate.

4.4 Cooling the Magnetron Motion

After loading, the electron's axial motion is readily damped, coming into thermal equilibrium with the 100 mK detection circuit. The radius of the electron's magnetron motion is initially large. For a cloud of many electrons, the magnetron radii will be distributed broadly. Each electron, in its magnetron orbit, then, will sample a different potential, due to off-axis inhomogeneities; the result is a broad range of axial frequecies and a large axial linewidth. Therefore, the next step, after loading, is to reduce the radius of the magnetron motion, moving the electrons to the central harmonic region of the trap.

As described in chapter 3, the magnetron motion is unstable. Removing energy results in an increasing radius until the confined electron is lost from the trap. However, the damping time is long, on the order of gigayears, and so the magnetron motion is treated as stable, and an electron will stay at its initial magnetron radius. To reduce the radius, then, energy must be added to the magnetron motion, moving the electron to the top of the repulsive radial potential hill. This is accomplished by sideband coupling to the axial motion [48], whereby an AC drive is applied at a frequency equal to the axial frequency plus one magnetron frequency: $\omega_{SBdrive} = \omega_z + \omega_m$. The drive

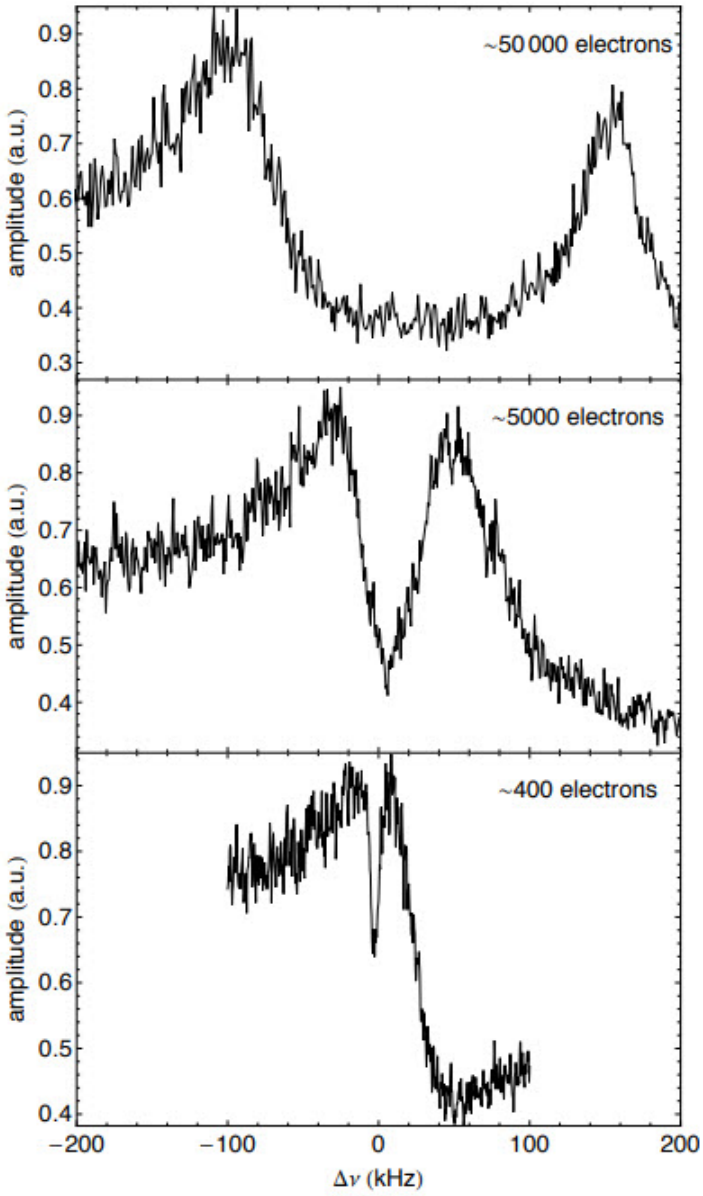

Figure 4.4: The signal of the confined electron cloud is seen as an inverted Lorentzian dip in the larger Lorentzian-shaped noise resonance. The width of each dip, determined by the fit, is given by $N\gamma_z$, the number of trapped electrons times the single-electron damping rate.

is produced using a Programmed Test Sources (PTS) 250 frequency synthesizer, and is applied to half of the third segmented electrode according to the scheme in fig. 4.5. The drive line is illustrated in the wiring diagram of fig. 3.21.

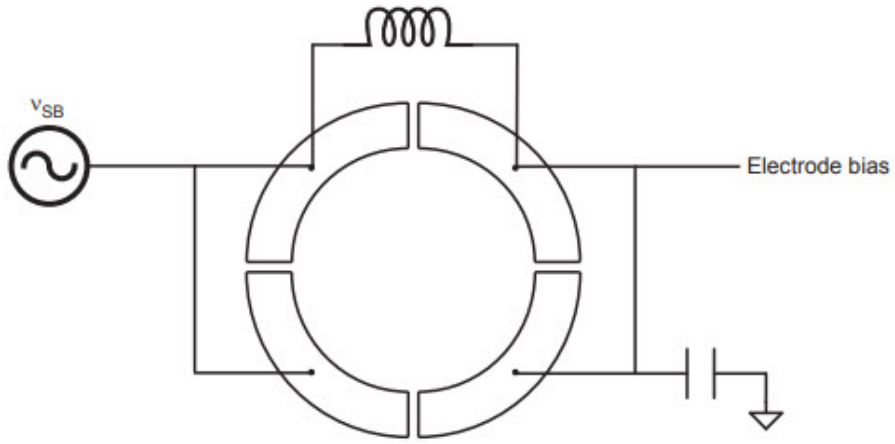

Figure 4.5: The magnetron motional sideband cooling scheme. The inductor blocks the AC drive while providing a DC path for the electrode bias voltage. Figure from [9].

The added axial energy is rapidly damped, while the energy in the magnetron motion approaches its limit and the magnetron radius is reduced. The magnetron motion is then said to be "cooled." Evidence of magnetron cooling, imaged by a spectrum analyzer, is presented in fig 4.6. A dip is shown as a response to the presence of electrons in the trap. The sideband drive, at $\nu = \nu_z + \nu_m$ is out of view to the right of the frame. On the right edge of the dip, at $\nu = \nu_{drive} - \nu_m$, a cooling peak is seen as the electrons' axial motion responds to the drive. As the electrons are cooled to the central, harmonic region of the trap, the axial linewidth is reduced and the cooling peak vanishes.

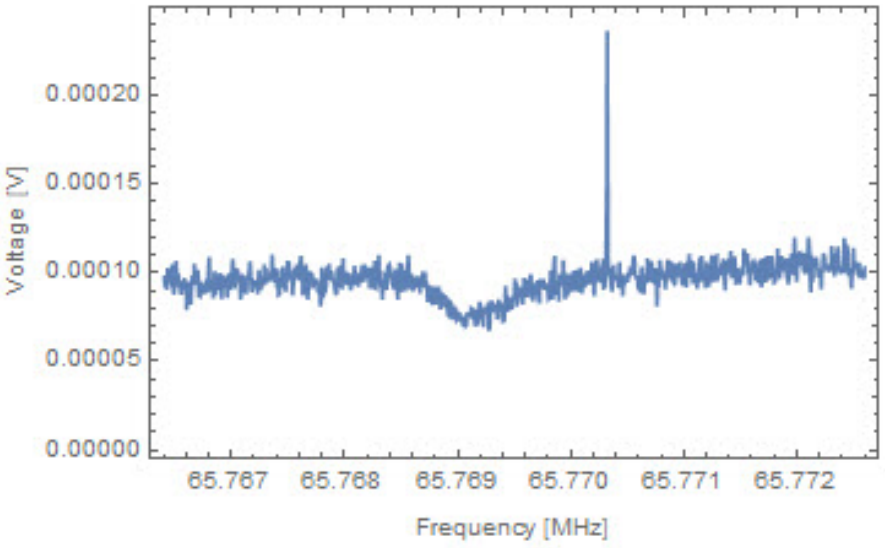

Figure 4.6: Evidence of sideband cooling of the magnetron motion is shown. The electrons initially inhabit a broad range of magnetron orbits of varying radii, resulting in a broad range of axial frequencies and an inflated axial linewidth, visible here as a dip in the noise resonance. The sideband drive, at $\nu = \nu_z + \nu_m$ is out of view to the right. A cooling peak is seen to the right edge of the dip, as the electron axial motion responds to the drive.

4.5 Tuning the Trap Anharmonicity

Arriving at an accurate measurement of the axial linewidth requires minimizing the thermal anharmonic width, $\Delta\omega_z$, such that $\Delta\omega_z << \gamma_z$, as discussed in chapter 3. The effect of anharmonicity on the observed axial linewidth is given by

$$\frac{\Delta\omega_z}{\omega_z} \approx |a_2| \frac{k_B T_z}{\frac{1}{2} m\omega_z^2 \rho_1^2}, \tag{4.6}$$

where T_z is the axial temperature and a_2 is the amplitude coefficent in the lowest-order term of the amplitude-dependent axial frequency expansion. The amplitude coefficients, a_k, are functions of the potential expansion coefficients, C_k, which are in turn functions of the trap dimensions, ρ_i, and electrode bias voltages, V_i. Though every effort has been made to eliminate anharmonicity in the trap by choosing appropriately optimized electrode dimensions and the calculated bias voltages, some anharmonicity is unavoidable. The laboratory trap is not ideal; it has gaps between its electrodes with dimensions given by the limited precision of practical machining methods, finite boundaries, and imperfect electrode surfaces. Therefore, adjustments must be made to the optimized trapping potential *in situ* to accommodate these realities. To this end, the amplitude coefficient a_2, which quantifies the thermal broadening of the axial linewidth, is tuned by adjusting the trap potential, thereby minimizing anharmonicity and the subsequent broadening that would inflate the observed axial linewidth.

Tuning of the anharmonicity requires a method for measuring its effect so that it may be minimized. Cylindrical Penning traps are designed such that the anharmonicity is tuned away by adjusting the bias voltage on the compensation electrodes only, while monitoring the effect on the shape of the axial resonance [48]. The axial reso-

nance is driven for greater signal-to-noise and, therefore, more precise anharmonicity monitoring and compensation. This same approach does not apply to the task of anharmonicity compensation in the planar Penning trap. Because of the inherent lack of reflection symmetry and the subsequent amplitude dependence of the axial frequency, driving the axial motion results in a shift of the axial frequency that makes monitoring its driven resonance shape impracticable.

In tuning the planar Penning trap anharmonicity, then, we rely on the fact that an anharmonic potential will give rise to a broader and shallower axial resonance dip than a harmonic potential will. Tuning proceeds by stepping the bias voltages, V_i, while monitoring the axial resonance dip shape. Any change in the potential minimum, z_0, will affect the single-electron linewidth and complicate our tuning efforts. Therefore, we hold z_0 constant. In addition, we hold the axial frequency, ω_z, constant and in tune with the detection amplifiers. For anharmonicity tuning purposes, then, the constraint equations for small changes are

$$\Delta\omega_z(\Delta V_1, \Delta V_2, \Delta V_3) \approx \frac{\partial\omega_z}{\partial V_1}\Delta V_1 + \frac{\partial\omega_z}{\partial V_2}\Delta V_2 + \frac{\partial\omega_z}{\partial V_3}\Delta V_3 \stackrel{!}{=} 0 \tag{4.7}$$

$$\Delta z_0(\Delta V_1, \Delta V_2, \Delta V_3) \approx \frac{\partial z_0}{\partial V_1}\Delta V_1 + \frac{\partial z_0}{\partial V_2}\Delta V_2 + \frac{\partial z_0}{\partial V_3}\Delta V_3 \stackrel{!}{=} 0. \tag{4.8}$$

With each step of ΔV_2, the partial derivatives are calculated such that the equations may be solved for ΔV_1 and ΔV_3. Previous efforts with this apparatus began with the optimized biases given in Chapter 3, then proceeded with adjustments dictated by *in situ* anharmonicity tuning [9]. These tuning results are shown in Fig. 4.7. Dip width and depth are shown as a function of the step in V_2. The new, tuned values of the applied bias voltages are found as the V_i corresponding to the dip width minimum

and dip depth maximum.

The present study picks up where the former study left off. A subsequent anharmonicity tuning study is shown in Fig. 4.8. Again, the dip width and depth are shown as a function of the step in V_2. The horizontal scale is the same, and similar steps in dip width are observed for similar steps in the potential. The dip depths are greater in the recent study, reflecting the greater signal due to improved detection electronics. The starting biasing configuration shows greater harmonicity, illustrating the effectiveness of the initial tuning. No indication is given for improving tuning.

In each instance of tuning, large electron clouds are used. In the previous instance, a dip width of $\sim$1000 Hz is achieved at narrowest width during tuning. The current instance begins at the new bias voltages given by the previous result. The cloud measures on average $\sim$750 Hz at minimum as tuning begins. Efforts to tune with smaller electron clouds were not successful, likely due to axial frequency instability, which is discussed in Chapter 5. It is shown that the axial frequency can vary over a range of nearly 200 Hz, causing intermittent broadening of the observed axial linewidth. For small electron clouds, dip widths are observed to vary from their mean value by as much as 36% for the same bias voltage setting. As the measure of the instability approaches the width of the dip we are trying to resolve, it becomes difficult to discern a tuning trend, confounding efforts to tune with small electron clouds.

Once the trap potential is tuned and the loaded electrons are sufficiently sideband cooled to the central, harmonic region, the amplified electron signal is imaged on the spectrum analyzer and recorded (see fig. 3.21). In Chapter 5, data collection and analysis is discussed in detail.

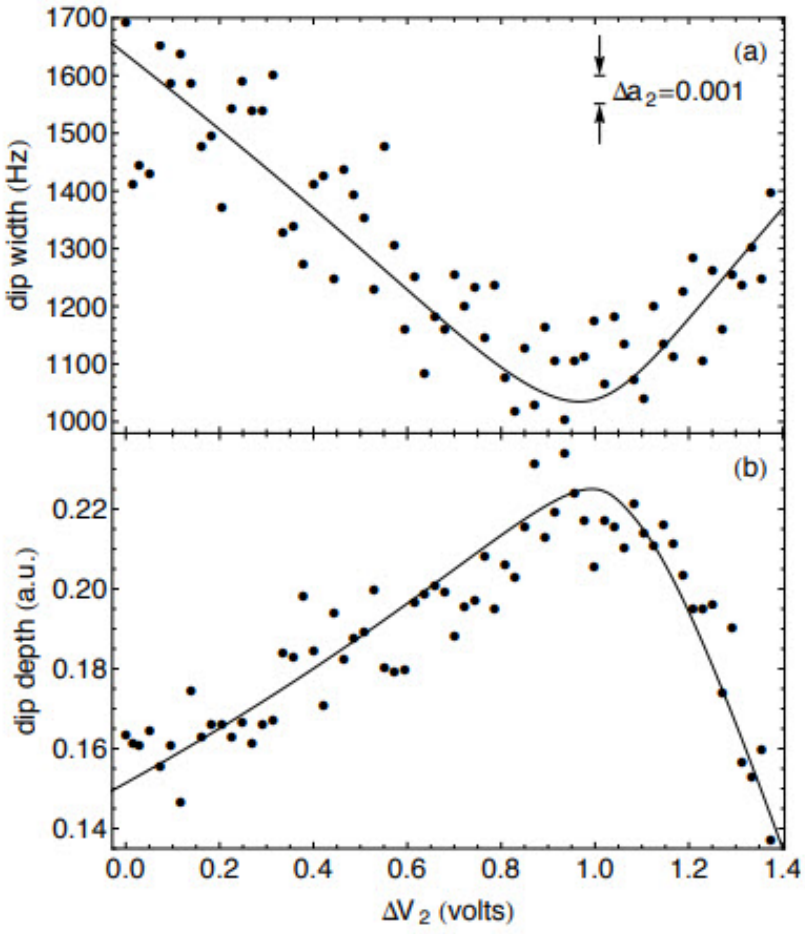

Figure 4.7: Initial planar Penning trap tuning study, from [9]. Dip width and depth are shown as a function of the step in V_2. Curves are drawn by hand to guide the eye. Initial bias voltages are given as the optimized values in chapter 3. New, tuned values are found as the V_i corresponding to the dip width minimum and dip depth maximum.

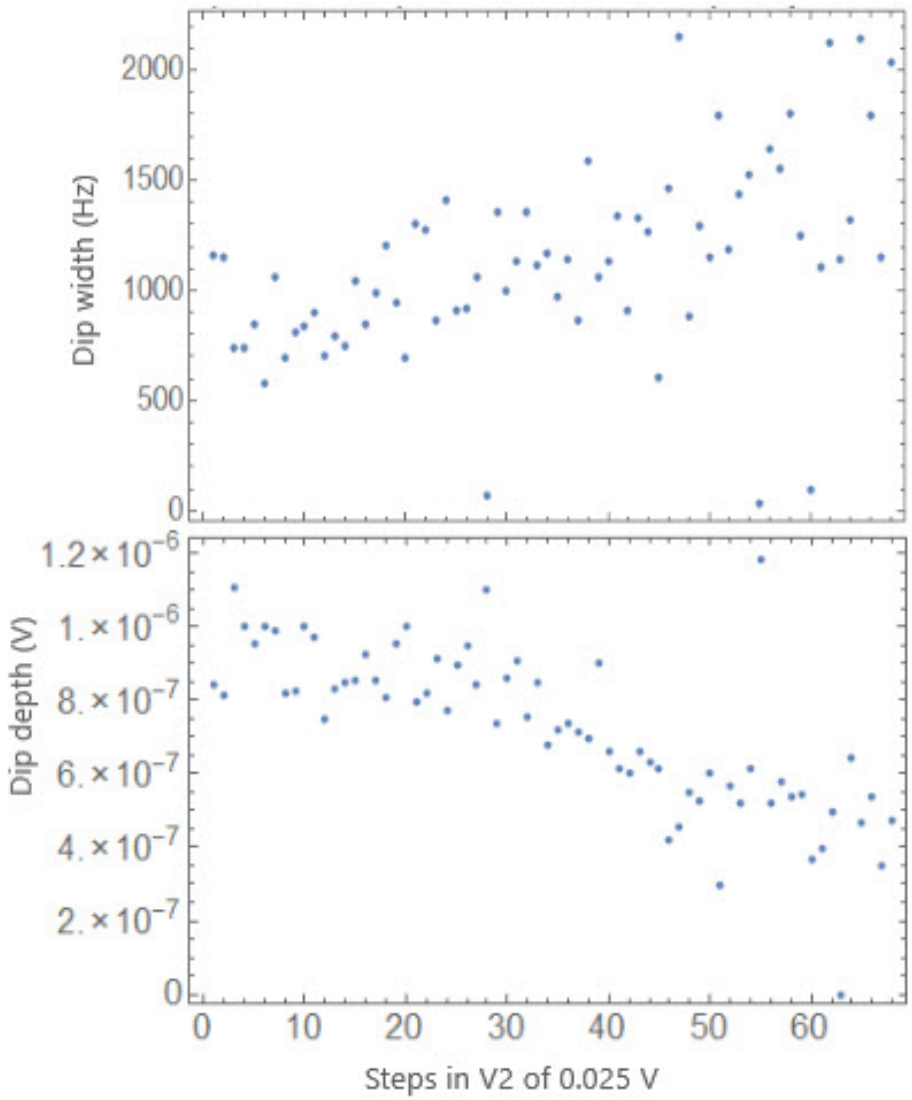

Figure 4.8: Subsequent anharmonicity tuning study, showing the effectiveness of initial tuning. The dip width and depth are shown as a function of the step in V_2. The initial biasing configuration shows greater harmonicity.

Chapter 5

Toward One Trapped Electron

The goal of the planar Penning trap experiment is to demonstrate the viability of a single-electron qubit in a planar Penning trap by trapping one electron in our optimized trap. Trapping and detecting a many-electron cloud has been achieved in our trap; the new challenge lies in loading and detecting only one electron. In our effort to demonstrate one trapped electron, we first show that for small electron clouds, measured axial linewidths are quantized by the single-particle linewidth; that is, the measured axial linewidth is given by $N\gamma_z/2\pi$ Hz, where $\gamma_z/2\pi$ is the single-electron linewidth, and N is an integer.

5.1 Calculating the Single-Electron Axial Damping Linewidth

A calculation provides the first approximation of the axial linewidth of a single electron. The linewdith is given by the trapped electron's axial damping rate and is

expressed by Eq. 3.3:

$$\gamma_z = \left(\frac{eD_1}{2\rho_1}\right)^2 \frac{R}{m} = \left(\frac{eD_1}{2\rho_1}\right)^2 \frac{Q}{m\omega_z C}. \tag{5.1}$$

As discussed in Chapter 2, the D_1 coefficient describes the coupling between the damping and detection electrode and the trapped electron. For detection on the center electrode (see fig. 2.14), D_1 is given by Eq. 2.34,

$$D_1 = C_{11} = \frac{-2}{\left[(z_0/\rho_1)^2 + 1\right]^{3/2}}, \tag{5.2}$$

and is dependent on the radius of the central electrode, ρ_1, and the distance between the electrode and the potential minimum, z_0. The quantities relavent to the calculation are summarized in Table 5.1.

ρ_1	1.05 ± 0.02 mm
z_0	1.570 ± 0.004 mm
D_1	-0.34 ± 0.01
Q	1707.50 ± 0.02
C	19.7 ± 0.3 pF
f	65.7569 MHz $\pm$5 Hz
$\frac{\gamma_z}{2\pi}$	26 ± 3 Hz

Table 5.1: Calculation of the single-electron linewidth. The quantities ρ_1, C, f, and Q are measured. The values of z_0 and D_1, which depends on z_0, are calculated.

The center electrode radius, ρ_1, is measured with a compound microscope and CCD camera. The uncertainty arises from identifying the electrode edge by eye. The value of z_0 is not readily measured, but is calculated given the trapping potentials and the measured electrode radii. D_1 is then found given ρ_1 and z_0.

The tuned-circuit amplifier Q is found by fitting a spectrum analyzer trace of the amplifier resonance to a Lorentzian lineshape, as is reported in Chapter 3. The uncertainty in the Q is then given by the uncertainty in the fit.

Contributions to the capacitance are 1) the capacitance between the central detection electrode and the adjacent, RF grounded electrode, 2) the capacitance of the long silver strap lead from the electrode to the feedthrough pin inside the trap can, 3) the distributed capacitance of the windings of the inductor coil of the tuned-circuit amplifier, and 4) the stray capacitance associated with the components of the amplifier circuit. The trap and lead capacitance is measured by the amount of capacitance that must be added during amplifier testing on the bench to bring the amplifier resonance to 65.76 MHz, and is found to be 13.0 ± 0.1 pF. The distributed capacitance of coil and circuit is calculated to be 6.7 ± 0.2 pF. It is found by first measuring the inductance L, then given the relationship $2\pi f = 1/\sqrt{LC}$, calculating the capacitance needed to attain an amplifier resonant frequency of 65.76 MHz, and finally subtracting the contribution to the capacitance due to the trap and lead, which is already measured. The total capacitance is then 19.7 ± 0.3 pF.

The frequency is the axial frequency of the trapped electron, found by fitting the dip spectrum to an inverse Lorentzian lineshape. We thus estimate that the single-electron linewidth, $\gamma_z/2\pi$, is 26 ± 3 Hz.

5.2 Data Collection

It is practical to begin data collection by first loading and trapping large electron clouds and then progressing to smaller clouds. Larger clouds, with measured axial

linewidths of hundreds of hertz, qre easily resolved after magnetron cooling as a dip in the noise spectrum on the spectrum analyzer. Smaller electron clouds are achieved by emptying the trap and loading again, firing the FEP at a decreased voltage or length of time. The center frequency of the smaller cloud's resultant dip shifts to lower frequencies, while the dip feature grows narrower and more challenging to find in the amplifier noise spectrum. The previous, larger dip then serves as a reference point for finding the narrower dip at a lower frequency, at which point the electrode voltages are scaled to shift the observed narrower dip back to the center of the amplifier resonance. The dip is then measured, and the process is repeated.

Upon reaching particle cloud sizes with linewidths that correspond roughly to fifteen trapped electrons or less, data are collected in a systematic fashion. For each loaded and cooled electron cloud, the dip spectrum is recorded by the spectrum analyzer for multiple averaging times, ranging from 0.25 seconds to 75 seconds, which correspond to 1 to 300 averages. For each averaging time, spectra are recorded in succession for 375 seconds. The spectrum analyzer is reset between each averaging event, such that each recorded spectrum represents a unique set of data points given by voltage versus frequency in a cataloged text file. The resolution bandwith (RBW) and video bandwith (VBW) are held constant at 10 Hz each. For each electron cloud, then, roughly 60 minutes of data are accumulated, representing, on average, several thousand spectra.

5.3 Data Analysis

For each electron cloud, the data is imported into Mathematica, where each dip spectrum is fitted to an inverse Lorentzian lineshape and the relevant parameters of dip width (FWHM), center frequency, amplitude, and noise background level, along with their respective uncertainties, are calculated and stored to file. A typical dip spectrum is shown in Fig. 5.1, and its width and uncertainty are reported.

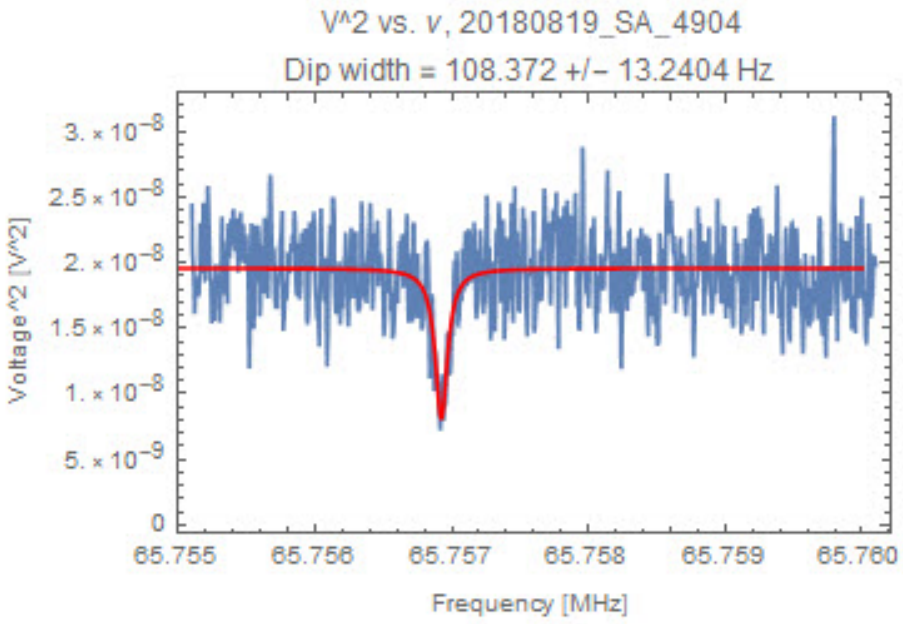

Figure 5.1: A typical dip spectrum, recorded after 50 averages. The dip is fitted to an inverse Lorentzian lineshape, as shown in red, and the dip's FWHM is reported.

A final, mean measurement of the axial linewidth associated with an electron cloud results from averaging successive spectrum measurements. However, first a spectrum analyzer averaging time must be chosen that allows for optimal resolution while introducing the least amount of noise. While longer averaging times result in better signal-to-noise and easier detection, shorter averaging times prevent broadening

of the dip feature due to frequency instabilities during averaging. Fig. 5.2 illustrates the broadening effect of frequency instabilities. The measured linewidth is shown to increase with an increase in averaging time. A reliable measurement thus requires a balance of these two factors. We therefore choose the shortest averaging time that will provide the signal-to-noise for effective detection.

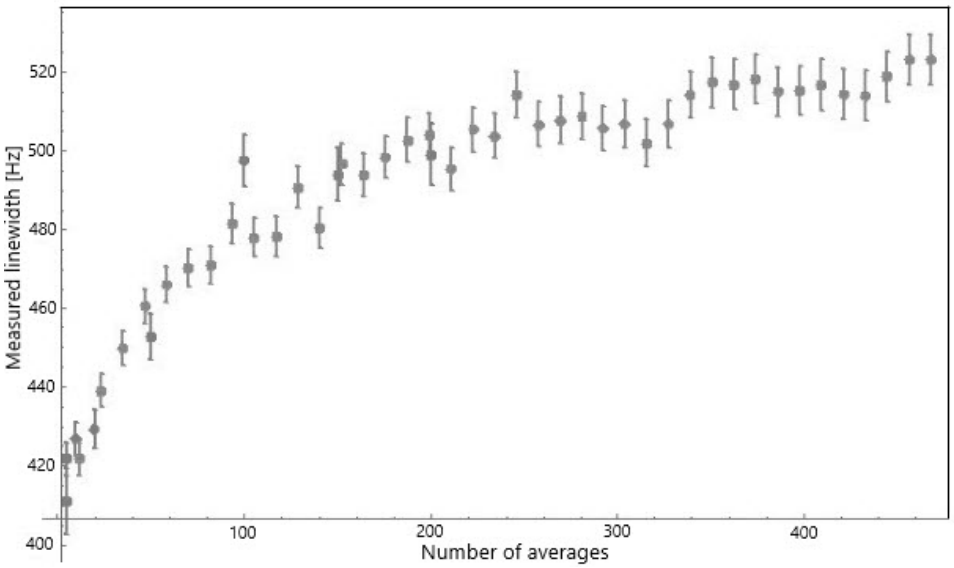

Figure 5.2: The measured linewidth of a single cloud of trapped electrons is shown to increase with increased averaging time. At large numbers of averages, the linewidth approaches a value that sets a limit on the frueqency instability.

5.3.1 Calculating the Allan Deviation

The Allan deviation, as a measure of frequency stability, provides an understanding of noise within the spectrum signal over time. The Allan deviation is the square root of the Allan variance, which is given as the variance formed by the average of the squared differences between successive values of the center frequency of the dip taken

over various measuring intervals. For N measurements of frequency, f_i, and averaging period τ, the Allan deviation is given by

$$\sigma_y(\tau) = \sqrt{\frac{\sum_{i=1}^{N-1}(f_{i+1} - f_i)^2}{2(N-1)}}. \tag{5.3}$$

The Allan deviation provides a measure of the variability of the dip center frequency as it is found by averaging spectra for different measurement times. It also allows for a way to differentiate between different types of signal variation. Fig.5.3 shows an Allan deviation plot for a representative cloud in the conventional log-log form. Because of frequency instability broadening observed for long averaging times, we focus on averaging times less than 100. A small Allan deviation is characteristic of good stability. Downward sloping regions, as from 20 to 50 averages, indicate short-time-scale oscillatory drift. Upward sloping regions suggest a long-time-scale drift. In the interest of maximizing frequency stability, 50 averages is chosen as a measurement time.

5.3.2 Data and Analysis

The measured axial linewidth as a function of run number for our repersentative cloud is show in Fig.5.4. Each data point represents the width of 50 averaged dip spectra, for a spectrum analyzer averaging time of 12.5 seconds. The mean axial linewidth is 154 Hz. The measured linewidth varies from the mean by as much as 36% over the time of the data run (6 minutes, 15 seconds), with no discernible trend.

The measured electron axial frequency as a function of run number over the same period of time is shown in Fig. 5.5. The axial frequency is measured as the center

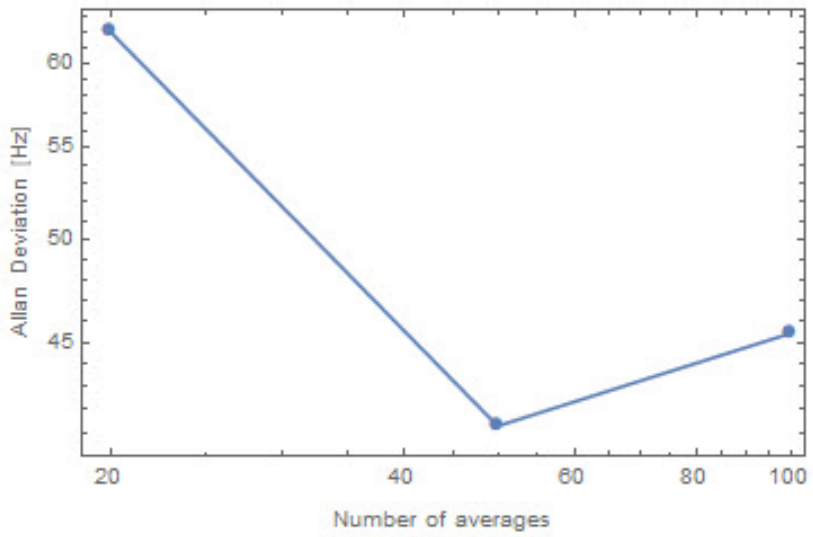

Figure 5.3: A representative Allan deviation plot. Because of frequency instability broadening for long averaging times, we focus on averaging times less than 100.

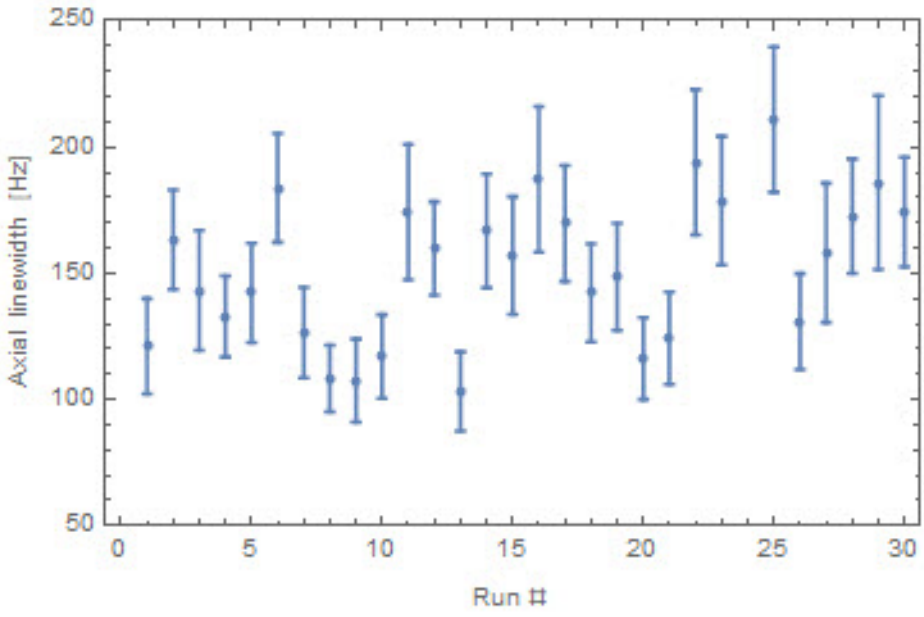

Figure 5.4: Measured axial linewidth as a function of run number for a representative electron cloud, loaded at an FEP firing voltage of -93 V for 120 seconds. Each data point represents the width of 50 averaged dip spectra, for a spectrum analyzer averaging time of 12.5 seconds. The mean axial linewidth is 154 Hz.

frequency of the dip in the noise spectrum. It is observed that the axial frequency varies during the run time over a range of nearly 200 Hz, a range that is greater by nearly an order of magnitude than the single-electron linewidth to be measured. The frequency drift shows no trend. This instability in the measured axial frequency of the electron cloud contributes to the large variation in measured linewidths.

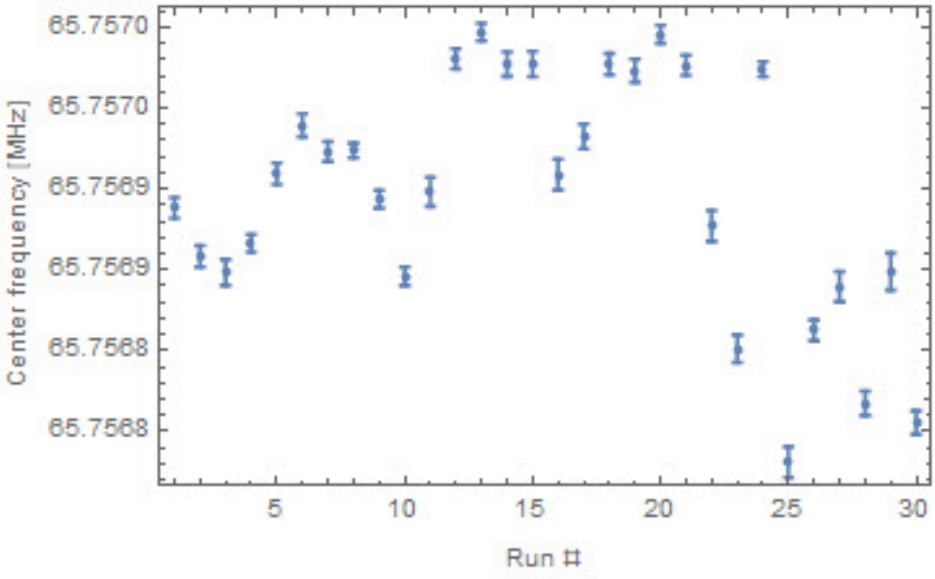

Figure 5.5: Measured axial frequency as a function of run number. The axial frequency is measured as the center frequency of the dip in the noise spectrum.

While a mean linewidth can be calculated from the measured widths reported, the mean width overstates the width that would be measured if the axial frequency were stable. We present a model whereby fluctuations in the axial frequency contribute to a broadening of the axial linewidth. There is no mechanism that would result in a narrowing of the linewidth. We therefore include in our final data set the narrowest observed linewidths with at least two consecutive repetitions. The final data set is summarized in Table 5.2. In each case, the reported linewidth is found as a sim-

ple average of the narrowest consecutive widths, and the uncertainties are found by propagation.

Run #	Measured linewidth [Hz]
1	103.4 ± 20.3
2	108.0 ± 10.5
3	101.2 ± 15.6
4	109.9 ± 16.5
5	131.0 ± 15.9
6	262.9 ± 16.0
7	298.6 ± 10.1
8	85.9 ± 9.6
9	273.9 ± 18.5
10	233.2 ± 15.0
11	373.0 ± 23.9
12	107.7 ± 7.3
13	236.9 ± 16.0
14	51.2 ± 6.8

Table 5.2: The final data set. The measured electron cloud axial linewidth is given by the FWHM of the Lorentzian fit to the dip spectrum.

The measured linewidths for each electron cloud may be plotted as a function of the number of electrons per cloud, where the slope of the linear fit gives the single-electron linewidth. The calculated single-electron linewidth may be used to find the number of electrons per cloud; however, the calculation is only a first approximation. Alternatively, a single-electron linewidth is assumed, a line fit to the resultant data, and R-squared calculated as a goodness of fit. We then compare the goodness-of-fit for each assumed single-particle value to find the value that best respresents the data.

R-squared as a function of the assumed single-electron linewidth is plotted in Fig 5.6. A maximum is observed at 27 Hz, consistent with the calculated width of 26 ± 3 Hz

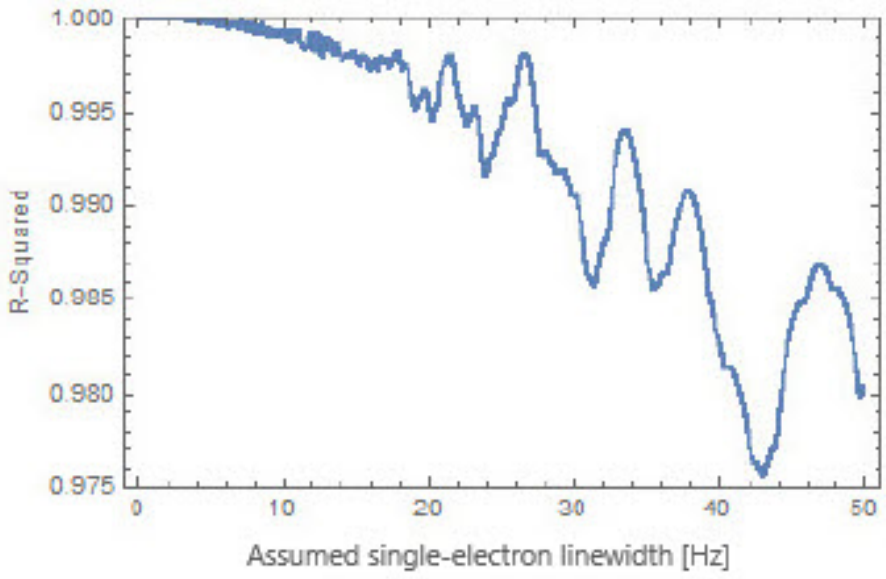

Figure 5.6: R-squared as a function of the assumed single-electron axial linewidth. A maximum of 0.99806 is observed at 27 Hz, consistent with the calculated width of 26 ± 3 Hz found in Section 5.1.

found in Section 5.1. R-squared tends toward unity for small widths, as expected; a width of 1 Hz will fit the data perfectly. The data is plotted as a function of run number, as shown in Fig. 5.7, with lines drawn at multiples of 27 Hz to illustrate quantization.

Finally, electron cloud axial linewidth, $N\gamma_z/2\pi$, is plotted as a function of the number of electrons per cloud, N, as shown in Fig. 5.8. The best-fit line is drawn with a slope of 27 Hz, corresponding to the single-electron linewidth given by R-squared. The dotted lines deliniate the region consistent with the calculated single-electron linewidth found in Section 5.1.

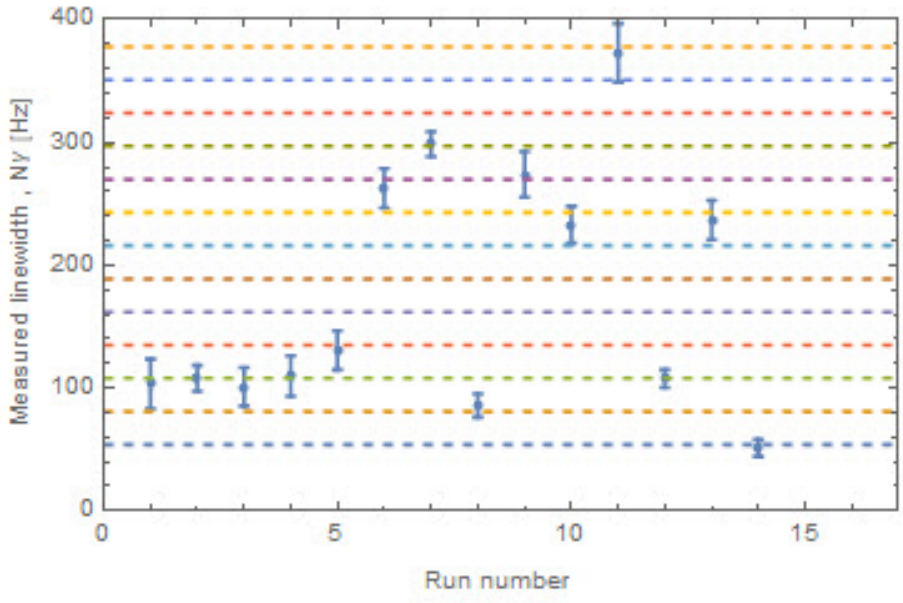

Figure 5.7: Measured axial linewidth as a function of run number for small electron clouds. Dotted lines are drawn to show quantization by the single-electron linewidth.

5.4 Discussion

Quantization by the single-electron axial linewidth is observed, with the smallest cloud achieved being that of two electrons. All efforts to load a smaller cloud were not successful. While this outcome falls short of the one electron result we seek, it shows a marked improvement over previous efforts at Mainz and Ulm. The result, substantially fewer than the minimum of 100-1000 electrons trapped at Mainz and Ulm, demonstrates significant progress.

Previous efforts in our laboratory with this apparatus reported a dip spectrum with a width consistent with the calculated single-electron width [9]. However, no data was reported showing consecutive measurements with similar widths. Frequency instability "within a few hundred Hz over several minutes" was observed, consistent

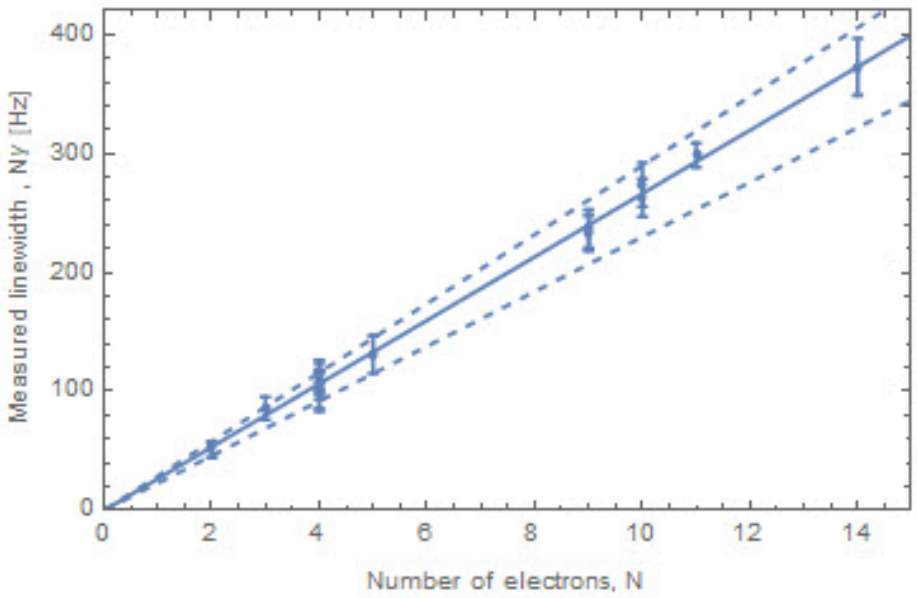

Figure 5.8: Measured electron cloud axial linewidth as a function of the number of electrons per cloud. The best-fit line is shown with a slope of 27 Hz, corresponding to the single-electron axial linewidth as given by R-squared. The dotted lines deliniate the region consistent with the calculated single-electron axial linewidth of 26 ± 3 Hz, indicating good agreement. Quantization by the single-electron axial linewidth is observed.

with the 200 Hz variation observed in the current study. Two suggestions were made to improve stability and sensitivity: further tuning, and improved detection electronics. The detection electronics were rebuilt and modified, and their improvement was demonstrated in Chapter 3. Further tuning, with smaller electron clouds, was not achieved, due to the same frequency instabilities observed previously.

Insufficient anharmonicity tuning likely contributes to the frequency instabilities we observe. However, a number of other factors can contribute to instability in the frequency of the axial motion.

We investigated electrode bias instabilities as a possible cause. The high-stability Fluke 5440B calibrators that bias the electrodes were found to be accurate to the reported value of 1 μV. Additionally, the electrode biases are filtered at the mixing chamber through low-pass RC filters with a 10 second time constant for added stability. A variation in the central electrode bias of 1 μV could shift the axial frequency by 10 Hz, but this is far from the $\sim$ 200 Hz variations we observe.

Another possible source of anharmonic effects is insufficient sideband cooling of the magnetron motion. The purpose of cooling the magnetron motion of the confined electrons is to move them to the central, optimally-harmonic and well-characterized part of the trap. An electron in a large magnetron orbit will sample a more anharmonic field. Every effort was taken to ensure adequate cooling of the magnetron motion. The sideband drive was tuned sufficiently high to observe an axial excitation peak, and cooling was considered complete when the excitation peak vanished and the electron dip narrowed. Adequate sideband cooling of the magnetron motion was observed.

An additional concern is noise from the outside environment, carried into the experiment via electrical lines for biasing, driving, and grounding. Since previous experiments with this apparatus in 2011, a 20 dB cold attenuator was installed on the sideband drive line to inhibit room-temperature Johnson noise and a potential source of magnetron heating. Additional noise suppression improvements to DC biasing lines, RF drive and detection lines, and grounding lines may further reduce noise and alleviate potential sources of instability.

Another possible source of frequency instability is anharmonicity due to patch potentials. The electrodes are plated with gold to resist surface reactions with adsorbed elements that promote surface potential structure. Additionally, the electrode gap height-to-depth aspect ratio was designed and measured to be greater than one to provide adequate screening of charges on the insulating surfaces of the substrate between gaps. Still, the electrode plane is not featureless, and the possibility of patch potentials cannot be ruled out. The electrostatic potential near even a gold surface can vary up to a milli-Volt due to patch structure and can fluctuate in time [56, 71]. In a planar trap, the electron is 1.57 mm away from the electrode, compared with $\sim$0.5 cm in a cylindrical trap, and so patch potential effects may more strongly impact stability.

One improvement to contend with possible patch potential structure is better electrode surface preparation. The mirror-like, featureless surfaces attained on cylindrical electrodes require polishing pastes and slurries. These substances readily accumulate in the electrode gaps and are difficult to dislodge, so we forwent this step, assuming that a 1 μm surface roughness was sufficient. Polishing to a finer roughness may

impact stability, and overcoming the difficulty in dealing with polishing pastes and slurries merits further exploration. Additionally, it has recently been observed in our laboratory, that patch potential effects may diminish over several days, leading to greater stability over time. Our current studies were carried out in tandem with the lepton magnetic moment experiment, and with tight scheduling, we did not extend our observation of the frequency instability over many days. This also warrants greater exploration.

5.5 Conclusion

The goal of the current study is to demonstrate the viability of a single-electron Penning trap qubit by trapping one electron in our optimized planar trap. Critical to this task is minimizing the anharmonicity in the trapping potential that crippled efforts at Mainz and Ulm. A judicious choice of electrode geometry and bias potentials, as described in Chapter 2, was the first necessary step. To contend with anharmonicity due to higher-order contributions and fabrication imperfections, an *in situ* anharmonicity compensation scheme was proposed.

As progress toward our goal, we show that for small electron clouds, measured axial linewidths are quantized by the single-particle linewidth, with the smallest cloud achieved being that of two electrons. All efforts to measure a smaller linewidth were not successful and were limited by axial frequency instabilities. While this outcome falls short of the one electron result we seek, it shows a marked improvement over previous efforts at Mainz and Ulm. The result, substantially fewer than the minimum of 100-1000 electrons trapped at Mainz and Ulm, demonstrates significant progress.

Chapter 6

Antihydrogen Apparatus

6.1 Introduction

This chapter presents the initial design and development of the second-generation ATRAP apparatus. This work was completed during the years 1999 to 2003, in the lead-up to and aftermath of our laboratory's first production of cold antihydrogen atoms in 2002.

The ATRAP collaboration's goal is to produce and study cold antihydrogen atoms. It grew out of the successes of the TRAP collaboration, which developed the methods for capturing and cooling antiprotons [72,73] on its way to a comparison of the charge-to-mass ratio of the proton and antiproton to a precision of 9 parts in 10^{11} [74].

With the first-generation ATRAP apparatus, our group successfully demonstrated the capture of 5.3 MeV antiprotons from CERN's Antiproton Decelerator (AD) [12], the subsequent positron cooling of the captured antiprotons [13], and the production of cold antihydrogen atoms [14], reporting the first measured distribution of antihy-

drogen states [15]. I undertook the development and fabrication of new detection electronics. Based on new designs [16], the HEMT-based first and second-stage cryogenic amplifiers provided for greater stability and detection sensitivity. Additionally, I built electronics for high-speed voltage switching to enable antiproton capture. I also fabricated new high-stability voltage supplies, developed with Jim MacArthur, for Penning trap electrode biasing.

In the wake of the achievements of this first-generation experiment, I undertook the design and development of a new apparatus that would allow for new capabilities. New open-access Penning traps were designed to increase trap volume, making way for improved particle capture rates and improved particle capacity for increased antihydrogen production. The new apparatus was designed to accommodate an Ioffe trap to confine the neutral antihydrogen atoms for study. Laser access was built into the design to allow for precision spectroscopy experiments. Efforts were made with every design decision to improve on materials and methods for robust operation and ease of use.

6.2 Motivation

The ultimate goal of the ATRAP experiment is to test physics' fundamental theories by conducting precision measurements with trapped antihydrogen atoms. All Lorentz-invariant, local quantum field theories, including the Standard Model of particle physics and quantum electrodynamics, are invariant under combined charge-parity-time (CPT) transformations. Any observed violation of CPT invariance would require new physics beyond our present models.

A consequence of CPT invariance is the requirement that particles and their antiparticles exhibit the same mass, magnitude of charge, and magnetic moment. The TRAP collaboration's comparison of the charge-to-mass ratio of the proton and antiproton to a precision of 9 parts in 10^{11} [74] was the most stringent test of CPT symmetry with baryons for many years. Currently underway in our laboratory is an experiment with the goal of comparing the magnetic moments of the electron and positron for the most stringent test of CPT symmetry with leptons [63].

A further consequence of CPT invariance is that hydrogen and antihydrogen exhibit identical energy structure. Precision spectroscopy of trapped antihydrogen atoms, compared to similar studies with ordinary hydrogen, could yield the most precise test of CPT symmetry in a lepton-baryon system. A comparison of the 1S-2S transition is especially attractive, with proposed measurements expected to an accuracy of 5 parts in 10^{16} [10]. Currently, the best measurement of this transition in hydrogen is accurate to 4.2 parts in 10^{15} [75]. A measurement with antihydrogen to similar accuracy would mark significant progress in testing CPT invariance. A comparison of CPT symmetry tests in various particle systems is shown in Fig. 6.1.

Gravitation studies with cold trapped antihydrogen atoms have also been proposed, which would test the validity of the weak equivalence principle [11, 77].

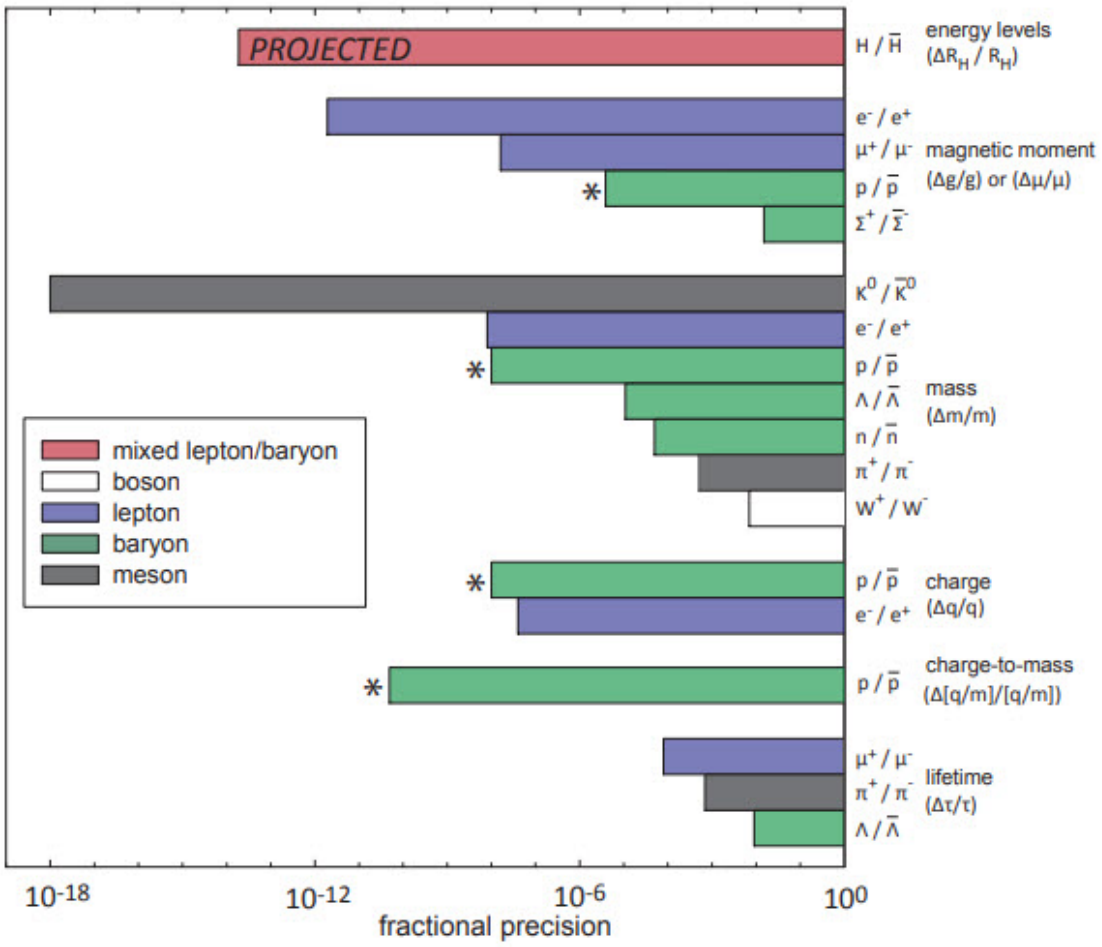

Figure 6.1: A summary of CPT symmetry tests in various particle systems, from [76]. An asterisk denotes studies performed by our laboratory.

6.3 Overview of the First-Generation ATRAP Experiment

An overview of the first-generation ATRAP experiment is given to provide context for the second-generation apparatus and to motivate the design changes. A detailed discussion of the experiment and the first-generation apparatus can be found in ref.s [78–81]. My contributions to this earlier experiment informed my later work on the second-generation design and on the redesign of the planar Penning trap detection electronics.

To produce antihydrogen atoms, antiprotons and positrons are confined in nested open-access Penning traps of the type described in Chapter 2. To access low-energy antiprotons, the ATRAP collaboration carries out its studies at the Antiproton Decelerator (AD) at the European high-energy particle physics laboratory CERN. Antiprotons produced in high-energy, fixed-target collisions are guided to the AD at 3.57 GeV/c, where they undergo a systematic process of stochastic cooling, radio-frequency deceleration, and electron cooling, resulting in a beam of 5.3 MeV antiprotons that delivers 30 million particles in 80 ns pulses every 108 s. The AD antiproton ring is illustrated in Fig. 6.2, and the ATRAP beamline is indicated.

Magnets in the beamline guide the beam, bending it upward toward the ATRAP apparatus, as shown in Fig. 6.3. As the antiprotons approach, they travel through a parallel plate avalanche counter(PPAC) [82], which monitors the position and intensity of the beam for steering and focusing purposes. They then travel through an energy tuning cell filled with a variable mixture of sulfur hexaflourine and helium. By

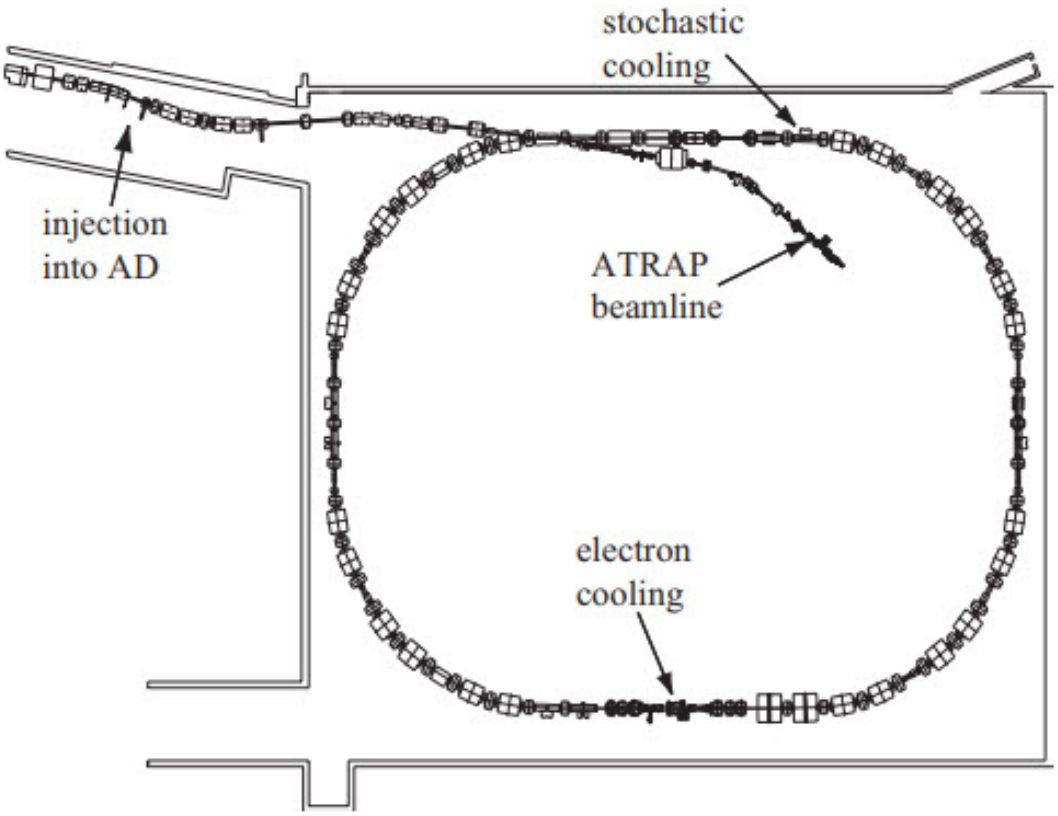

Figure 6.2: The Antiproton Decelerator (AD) ring. Cooling regions and the ATRAP beamline are indicated.

controlling the relative amounts of the gases, the energy of the antiprotons are tuned through collisional energy loss.

Finally, the antiprotons traverse a 10 μm thick titanium window, enter the trap vacuum space, and pass through a 125 μm thick beryllium degrader before reaching the trapping fields created by the Penning trap electrodes and the 6 T superconducting solenoid magnet. At each barrier, energy is lost, such that the 5.3 MeV antiprotons that exit the AD arrive at the trapping region of the ATRAP apparatus with energies low enough ($<$ 3 keV) to be captured.

A drawing of the first-generation experiment's Penning traps are shown in Fig. 6.4. The lower stack of gold-plated, copper electrodes separated by macor spacers that composes the nested Penning trap serves a number of purposes: (1) antiproton capture, (2) antiproton cooling by interactions with trapped electrons, and finally (3) antihydrogen production. The upper stack is dedicated to positron accumulation. Between the upper and lower stacks is a rotating electrode, a ball valve that can be opened to transfer positrons to the antihydrogen production region.

6.3.1 Antiproton Capture

A detail drawing of the antiproton capture region is illustrated in Fig. 6.5, and the capture scheme is described. The electrode stack is rotated in the drawing to illustrate the potential structure of the capture scheme. Antiprotons enter the Penning trap stack with a range of energies. The high-voltage electrode at the top of the stack is biased to -3 kV; therefore, those antiprotons with energies less than 3 keV are reflected back toward the degrader. Those at energies greater strike the ball valve

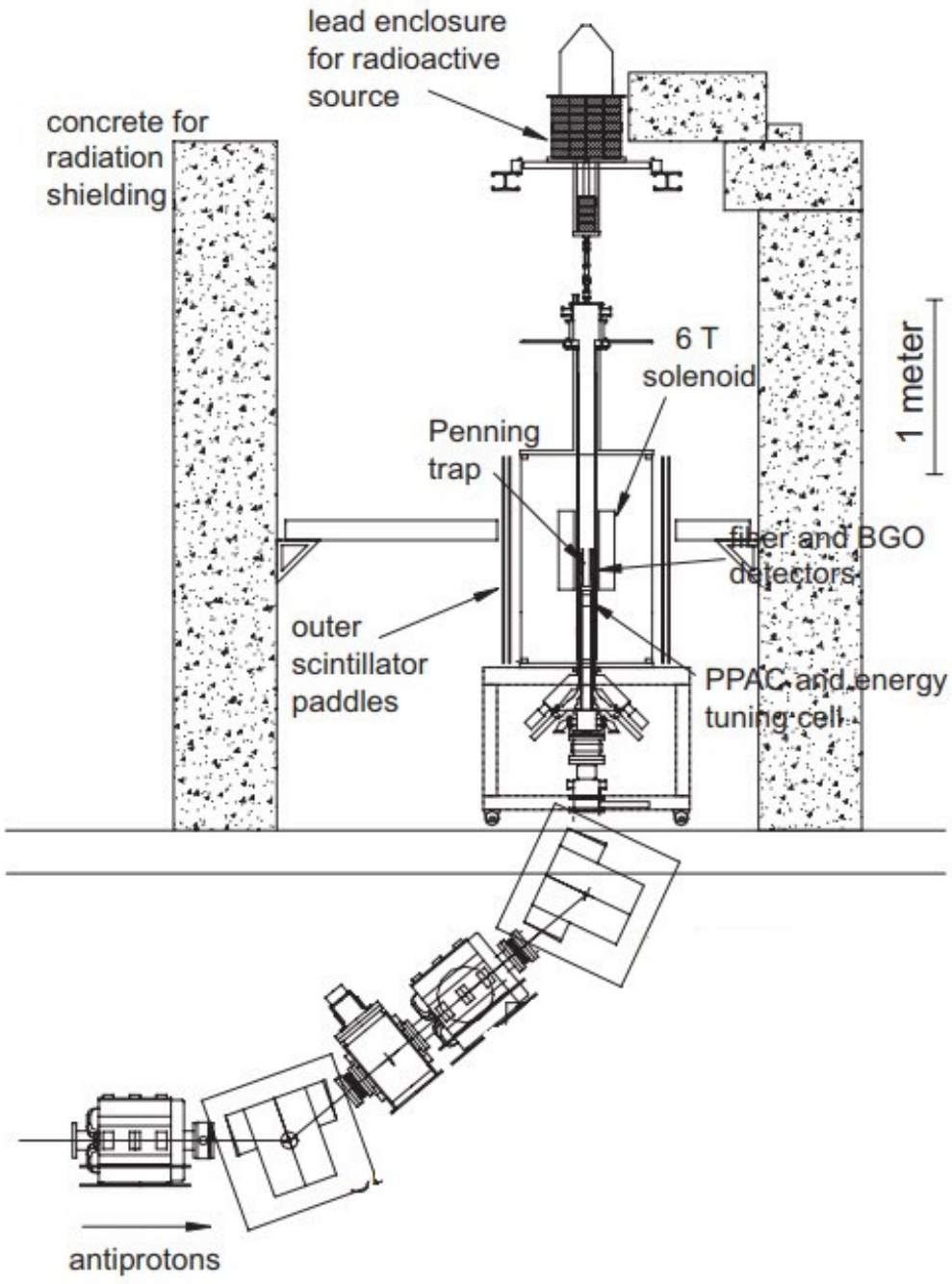

Figure 6.3: An overview of the first-generation ATRAP apparatus in its zone at the Antiproton Decelerator (AD). The antiproton beam is bent to enter the trapping apparatus from below.

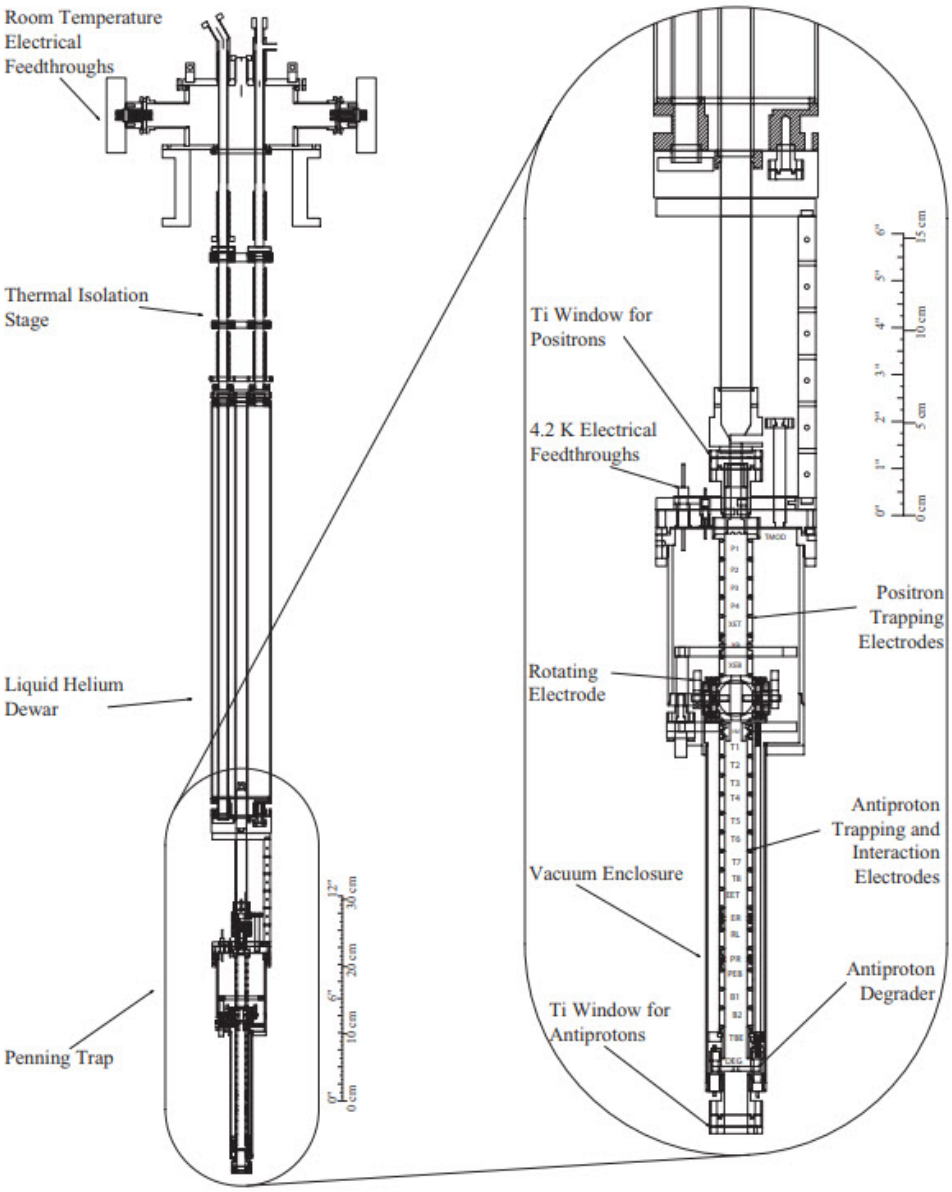

Figure 6.4: A drawing of the first-generation ATRAP Penning traps for particle capture and antihydrogen production, from [78].

and annihilate. A high-speed, high-voltage switch biases the degrader to -3 kV in ~ 50 ns, before the antiprotons complete their round trip, creating a potential well for capture.

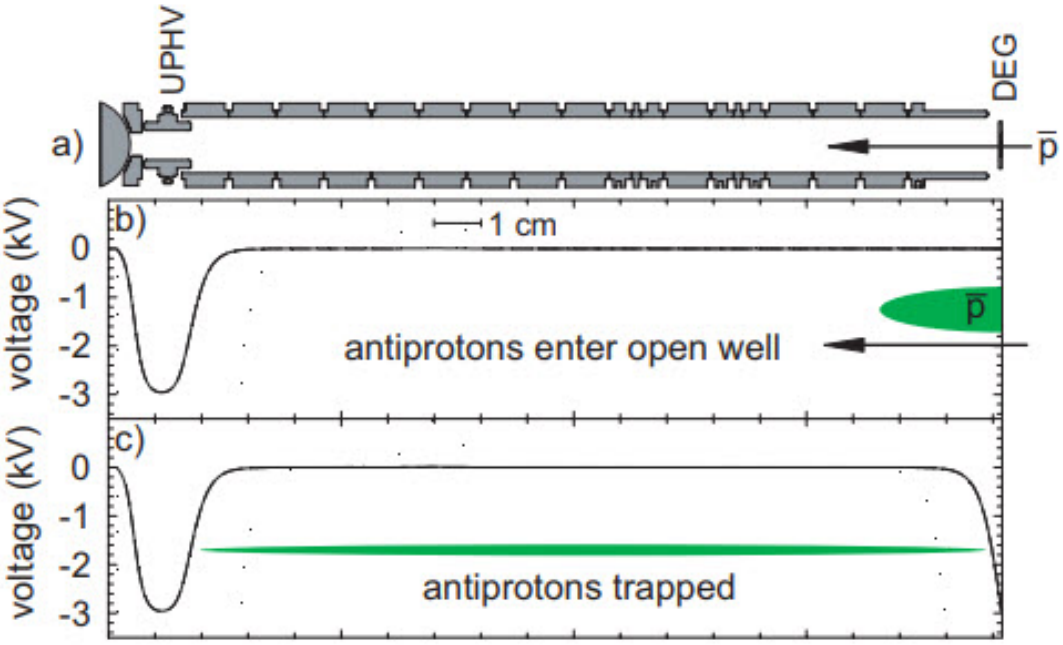

Figure 6.5: A detail drawing of the antiproton capture region of the first-generation ATRAP apparatus and a description of the capture scheme, from [79].

Capture efficiency is determined by the initial energy of the antiprotons, the voltage applied to the high-voltage electrode and degrader, and the relative timing of antiproton entry and degrader voltage switching. The capture rates and these dependencies have been studied in detail and are reported in refs. [12, 78, 79]. Roughly 20,000 antiprotons are trapped per pulse in this way.

The total number of captured antiprotons and their energy distribution is measured by ramping the degrader potential to 0 V while monitoring antiproton annihila-

tion on the degrader with the surrounding detectors shown in Fig.6.3. The detectors register the charged pions created during annihilation. The number of trapped antiprotons as a function of the high voltage well depth is shown in Fig. 6.6. Note that the trapping efficiency quickly saturates. This is explained by assuming that antiprotons emerging from the degrader with larger axial energies also have larger radial energy, and therefore a larger cyclotron radius in the magnetic field of the trap. Antiprotons at large enough radii, will strike the electrodes and annihilate, eluding capture. A trap with a larger electrode radius should achieve a trapping efficiency that remains linear up to higher trapping voltages.

This observation motivates electrode design for the second-generation apparatus. As will be seen, the Penning trap solenoid is increased in diameter to make room for new capabilities, and consequently, the magnetic field is reduced in magnitude. To maintain and improve upon antiproton capture rates, larger diameter electrodes are used in the capture region.

6.3.2 Electron Cooling Antiprotons

Antiprotons captured in the fashion describe above are still relatively energetic at around 1 keV and must be cooled in order to facilitate the interactions that produce antihydrogen. Cooling is achieved by collisional energy transfer with simultaneously trapped electrons [83].

The scheme is described in Fig. 6.7. Prior to antiproton capture, electrons are introduced by a field emission point (FEP), as described in Chapter 3, that is embedded in the rotating ball valve. Their cyclotron motion cools by the emission of synchrotron

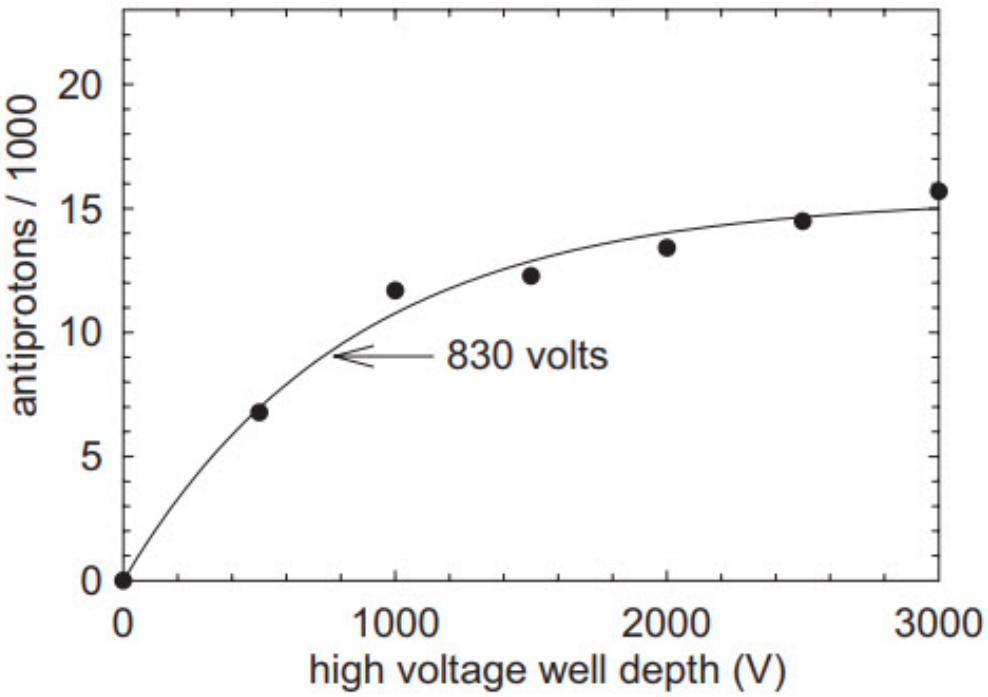

Figure 6.6: Captured antiprotons as a function of the high voltage well depth, from [78].

radiation, and their axial motion is cooled by collisional coupling to the cyclotron motion. Roughly 3 million electrons are loaded in to a 12 V well. The antiprotons collide with the electrons as they oscillate in the long potential well. Through Coulomb collisions, antiproton axial energy is transferred to the cyclotron motion, which is then cooled radiatively, until the antiprotons reach thermal equilibrium with the electrons at 4.2 K, the temperature of the thermally linked liquid helium reservoir. Note that antiprotons at large cyclotron orbits, away from the center of the trap and outside the $\sim$ 4 mm radius of the electron cloud, are not cooled. The process is complete in $\sim$ 50 s, and the electrons are ejected by opening the small potential well for 100 ns, time for the lighter electrons to exit, leaving the heavier cold antiprotons behind. During cooling, antiproton loss is monitored and compared to losses without cooling. No appreciable loss is shown due to electron cooling [79].

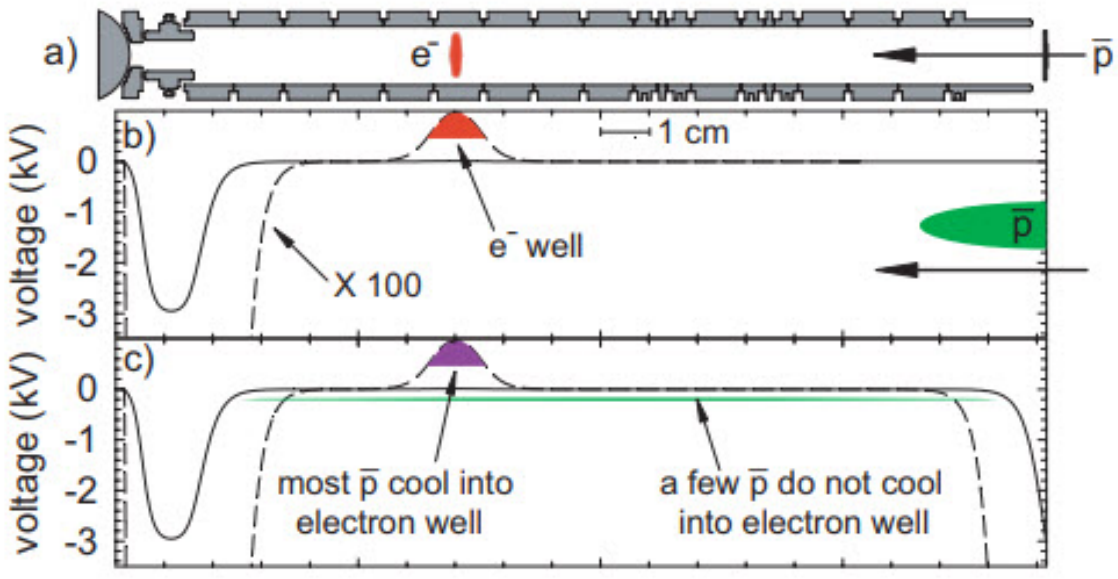

Figure 6.7: A scheme for electron cooling of antiprotons, from [79].

6.3.3 Stacking Cold Antiprotons

Antihydrogen production requires substantial numbers of cold antiprotons. To achieve a larger number than the 20,000 antiprotons captured and cooled by the methods above, stacking of successive beam pulses is needed. To stack antiprotons, once the electron cooling of one pulse is complete (85 seconds), the degrader potential is ramped to 0 V, releasing the uncooled antiprotons, and readying the trap for a subsequent pulse.

The number of antiprotons captured as a function of stacked pulse number is shown in Fig. 6.8. The result is shown to be linear in the number of pulses, suggesting that as many particles may be accumulated as time allows. The efficiency is shown in the lower graph. About 20% of the antiprotons captured are not cooled and expelled from the trap between pulses. About 10% are lost during electron cooling. More than 60% of the captured antiprotons are cooled and available for antihydrogen production. Up to 0.4 million antiprotons have been accumulated from 32 successive pulses from the AD [12].

6.3.4 Positron Loading

Positrons are accumulated for antihydrogen production by the field ionization of highly magnetized Rydberg positronium, a method developed in our laboratory for precision measurements with antimatter at cryogenic temperatures [80, 84, 85]. The method is illustrated in Fig. 6.9. The electrode stack for positron accumulation, as imaged in Fig. 6.4, is shown rotated to illustrate the potentials.

Positrons emitted from a ^{22}Na source with a range of energies up to 545 keV travel

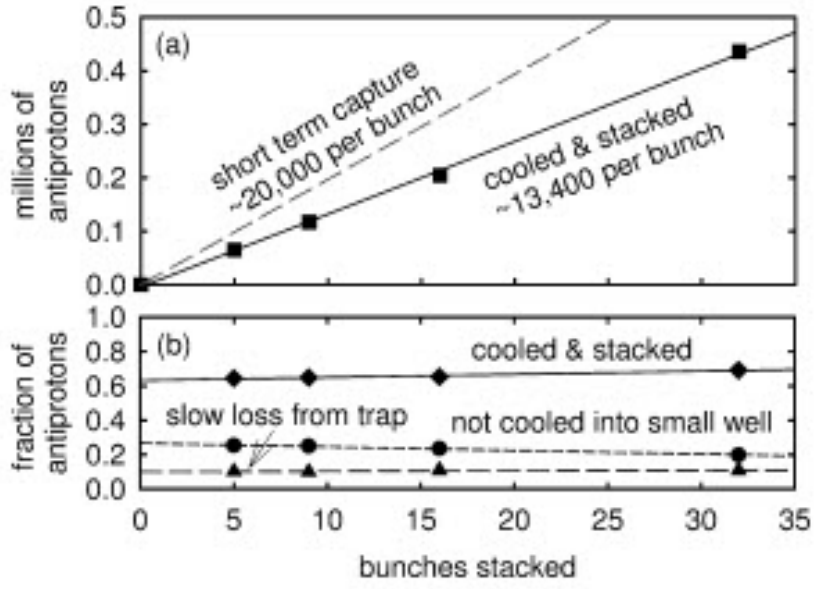

Figure 6.8: Stacking antiprotons from successive pulses from the AD, from [12].

through a 10 μm thick titanium window and into the trap vacuum space. A 2 μm thick single crystal tungsten foil transmission moderator (TMOD) is suspended by tungsten wires at the top of the electrode stack, and a thick 2 mm tungsten crystal reflection moderator (RMOD) is added at the bottom of the stack, embedded in the rotating ball valve, as shown. Both are heat treated by standard techniques to improve efficiency [86]. Of the energetic positrons that pass through TMOD, $\sim 0.05\%$ exit with an energy of ~ 2 eV. These slow positrons can pick up a secondary electron, forming highly-excited Rydberg positronium. The potentials on the electrodes in the accumulation stack are biased such that the positronium atom is ionized as it traverses the stack, guided by the magnetic field, and the positron is collected in the potential well, while the excess energy is carried away by the electron.

Most of the energetic positrons from the source pass through TMOD and continue

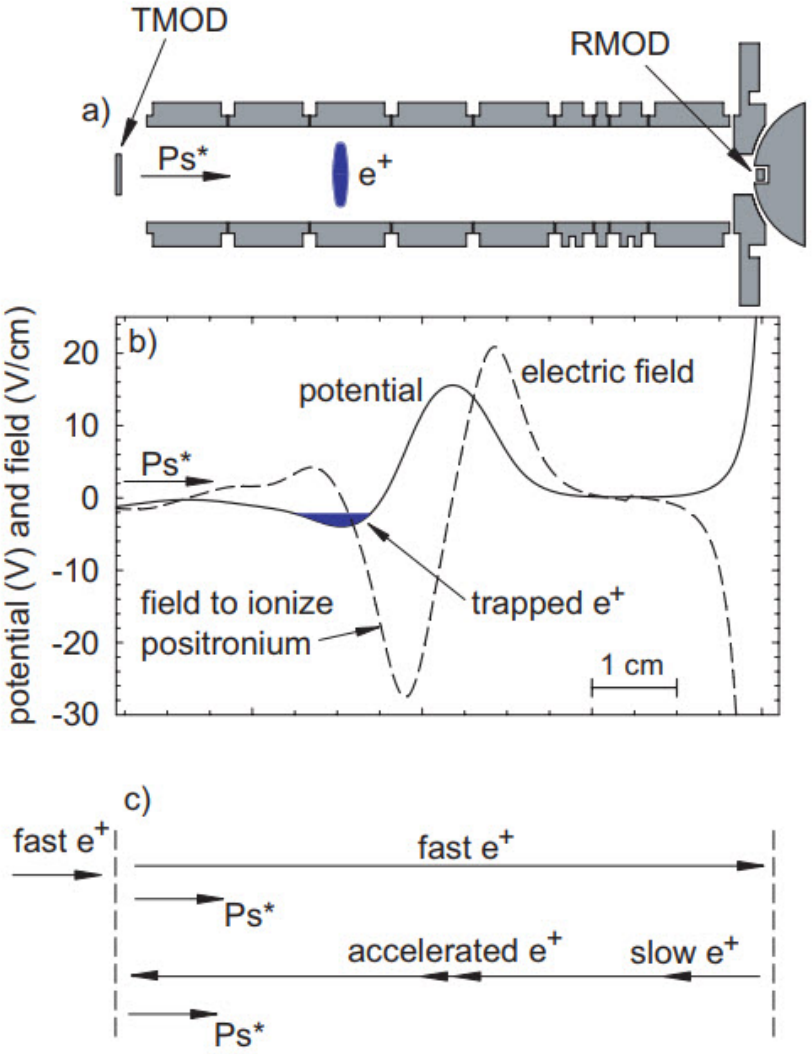

Figure 6.9: The positron loading scheme, from [79].

through the stack, reaching RMOD. Roughly 0.25% of these are reflected as slow positrons, carried back to TMOD by the large potential, diffuse a short distance into TMOD, and reflect again to pick up an electron and form Rydberg positronium as described before. The accumulation rates are dependent on the voltages applied to TMOD and RMOD, as illustrated in Fig. 6.10. Adjusting the voltage on TMOD tunes the positronium production and subsequent accumulation rate. The addition of RMOD to the scheme increases the accumulation rate by a factor of ~ 2.5. Normalized to the source strength, the maximum rate observed is 1.4 $\times 10^4$ positrons per hour per mCi. For antihydrogen production, up to 1.6 $\times 10^6$ positrons are loaded [14].

6.3.5 Antihydrogen Production

With antiprotons and positrons confined, antihydrogen production may proceed. A nested Penning trap is used to confine both the negatively charged antiprotons and the positively charged positrons in the same trap volume for interaction. A simple nested Penning trap is illustrated in Fig. 6.11. The electrodes are biased such that the positrons are confined in a potential well that is nested within the potential well that confines the antiprotons.

The first production of antihydrogen in our first-generation apparatus occurred during the positron cooling of antiprotons in a nested Penning trap. Positron cooling of antiprotons was first reported in 2001 [13]. The cooling mechanism is the same as that for the electron cooling of antiprotons described above. The antiprotons transfer energy to the positrons during Coulomb collisions, and the positrons then quickly cool by synchrotron radiation. However, simulataneously manipulating oppositely

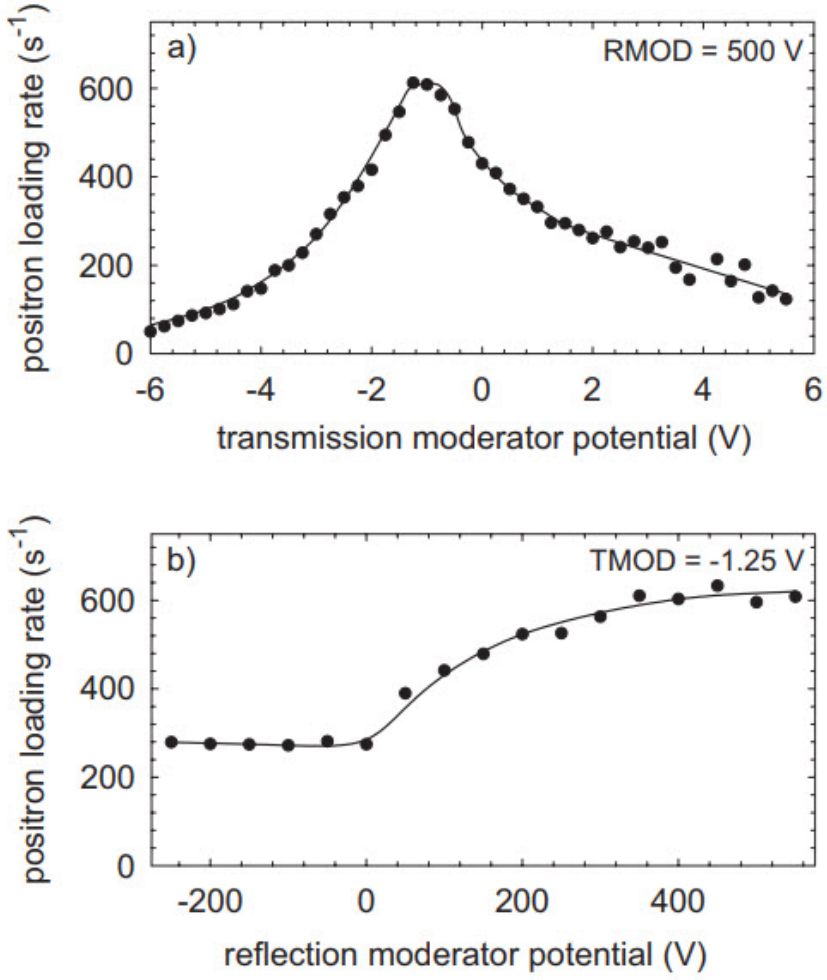

Figure 6.10: Positron loading rate as a fuction of the voltage applied to TMOD and RMOD.

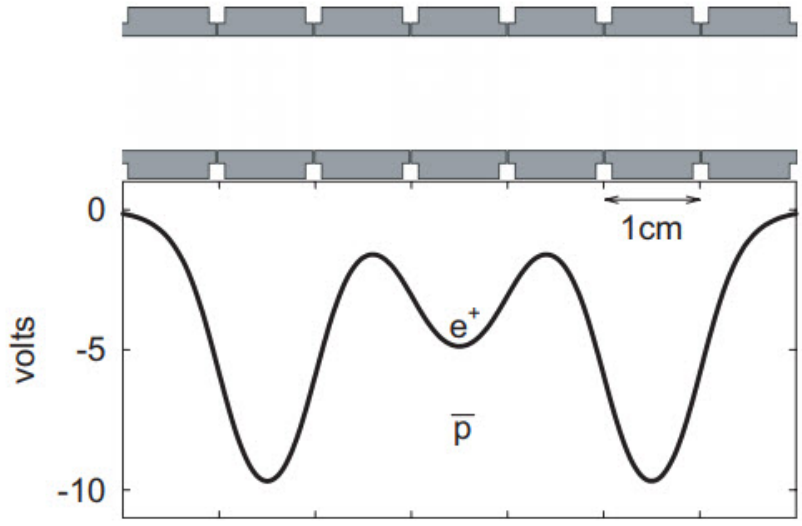

Figure 6.11: The nested Penning trap scheme. Oppositely charged antiprotons and positrons are trapped in the same volume for interaction.

charged particles presents a challenge.

The scheme is described in Fig. 6.12. A potential well containing cold electron-cooled antiprotons is adiabatically elevated. The antiprotons are then launched into the nested trap and the electrons expelled as the potential is pulsed from that indicated by a solid line to the dashed line and then back to solid again. The launch and release process takes 1.5 μs. The antiprotons and positrons interact for two minutes, and the energy distribution of the trapped antiprotons is analyzed by slowly lowering the potential while monitoring annihilation products with the surrounding scintillating detectors. The experiment is conducted both with and without positrons present, and the results are shown in Fig.s 6.12(a) and 6.12(b). It is shown that most of the antiprotons have cooled to the same level as the positrons. The antiprotons that do not cool are presumed to be at large cyclotron orbits and therefore do not interact with the cold positrons.

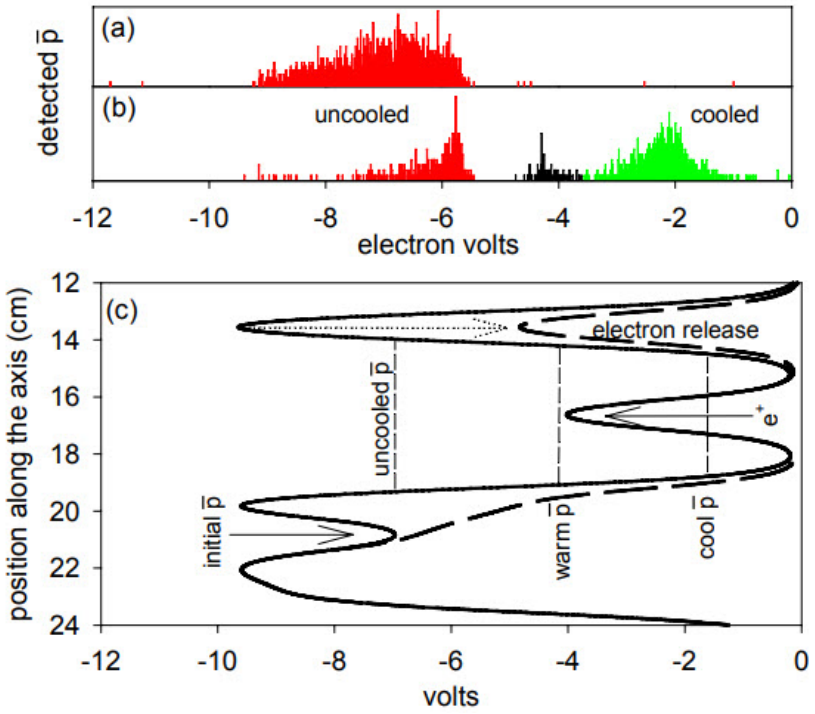

Figure 6.12: A nested Penning trap scheme for the positron cooling of antiprotons.

It is possible that antihydrogen atoms were formed during this first demonstration of positron cooling of antiprotons. The dominant antihydrogen formation process is three-body recombination [87]. Three-body recombination is given by the process

$$\bar{p} + e^+ + e^+ \rightarrow \bar{H} + e^+, \tag{6.1}$$

where an antiproton interacts with two positrons. The extra positron carries away the excess energy as the antiatom bound state is formed. We expect this process to dominate due to its high calculated rate compared to other processes. For 10^4 antiprotons and a positron density of $10^7/cm^3$ at 4 K, the antihydrogen production rate via three-body recombination is $6 \times 10^6 s^{-1}$ [87]. While the production rate is high, antihydrogen atoms formed by this process are weakly bound. Highly-excited Rydberg antihydrogen atoms would be ionized in the trapping fields. However, further collisions with confined positrons may lead to sufficient de-excitation such that the atoms survive the trapping fields [88].

Following on this success, a new scheme was developed that intentionally uses field ionization followed by antiproton capture to detect antihydrogen atoms produced during the positron cooling of antiprotons [14] and results reported in 2002. The scheme is illustrated in Fig. 6.13. As before, antiprotons must be given enough energy to overcome the electric potential confining the positrons in order to enter the positron region for antihydrogen production. The antiprotons are therefore launched into the nested Penning Trap by pulsing the solid to the dashed potential. The antiprotons travel through the positrons and lose energy via Coulomb collisions, as before.

It is expected that antihydrogen forms most efficiently when its constituents have

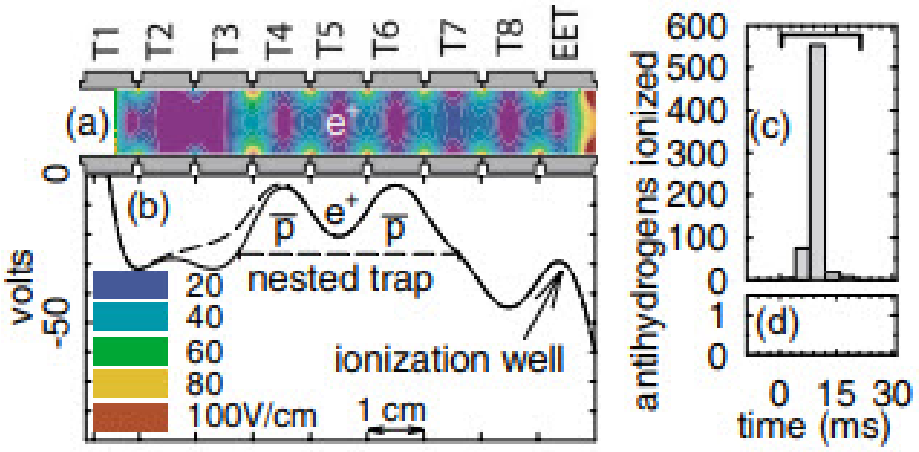

Figure 6.13: The detection of antihydrogen atoms by field ionization.

low relative velocities. A neutral antihydrogen atom is no longer confined by the nested Penning trap, and is free to move in the initial direction of antiproton. An antihydrogen atom in a highly-excited state as we expect that moves through the field-ionization well will be ionized by the electric field and its antiproton will be confined to the well. The potentials are carefully constructed so that antiprotons in the nested well cannot reach the ionization well. Therefore, any detected antiprotons in the ionization well are a result of antihydrogen formation. The trapped antiprotons are counted once the nested trap is emptied by ramping down the ionization well voltage. The antiprotons strike the electrodes and annihilate, producing pions that are detected in the surrounding scintillating detectors. There is no background. As is shown, 657 ionized antihydrogen atoms were captured. The number captured increases as the number of confined positrons increases. None are captured by repeating the experiment without positrons present. At the time this result was published [14], this was more than the total number of antihydrogen atoms that had been observed in all other experiments.

A rough estimate of the antihydrogen states is deduced given that the ionization events are for atoms that will ionize in electric fields between 35 and 95 V/cm. It is estimated that the antihydrogen atoms formed have binding energies corresponding to n=43 to n=55 [14], consistent with what is expected for a three-body recombination process.

Quickly following on this success, additional experiments were performed where the antiprotons are resonantly driven repeatedly through the trapped positrons to improve on the efficiency of antihydrogen production [15]. A distribution of the antihydrogen states were reported for the first time, measured by varying the ionizing fields. Again, the rate of production and large-n states suggest a three-body recombination process.

In the wake of these significant achievements, a second-generation apparatus was designed and development begun to expand the capabilities of its predecessor.

6.4 An Apparatus with New Capabilities

The second-generation ATRAP apparatus was designed to expand on the first-generation's capabilities. The experimental goals that drove its design were (1) the trapping of neutral antihydrogen atoms, (2) improved particle loading efficiency for increased production of antihydrogen, and (3) laser spectroscopy studies of trapped antihydrogen atoms. Efforts were made with every design decision to improve on materials and methods for robust operation and ease of use.

As with the planar Penning trap apparatus, the design and fabrication of a new ATRAP apparatus drew on our laboratory's previous experience with materials and

methods suitable to the cryogenic, UHV, and high-magnetic-field environment, and to the RF methods used to detect and manipulate particles.

6.4.1 Overview of the Apparatus

An assembly drawing of the proposed apparatus is shown in Fig. 6.14 and provides an overview of the second-generation ATRAP experiment. A three-dimensional drawing of the apparatus, as built, is shown in Fig. 6.15. The chief goal of the second-generation experiment was the trapping of the neutral antihydrogen atoms observed to be produced during the positron cooling of antiprotons. The necessary room for a Ioffe neutral atom trap that could be superimposed on the recombination region of the Penning trap drove all early design decisions.

To this end, a new magnet and cryogenic insert was commissioned with a 20 inch bore, providing a dramatic increase in volume over the 4 inch bore of the first-generation apparatus. A two-stage pulse tube cools the insert's intermediate layer to $<$77 K and the inner layer to 4 K. The superconducting solenoid, with a maximum field of 3 T, was designed to be homogeneous to one part in 10^4 at center. The Penning traps at the heart of the experiment are cooled by thermal contact with a liquid helium reservoir to 4 K. Above the reservoir are thermal isolation stages, separating the cryogenic parts of the apparatus from the room temperature "hat" at magnet dewar top, where all electrical connections are made via hermetic feedthroughs. Scintillating paddles and fiber detectors surround the magnet dewar for detection of annihilation events, as described in the previous section.

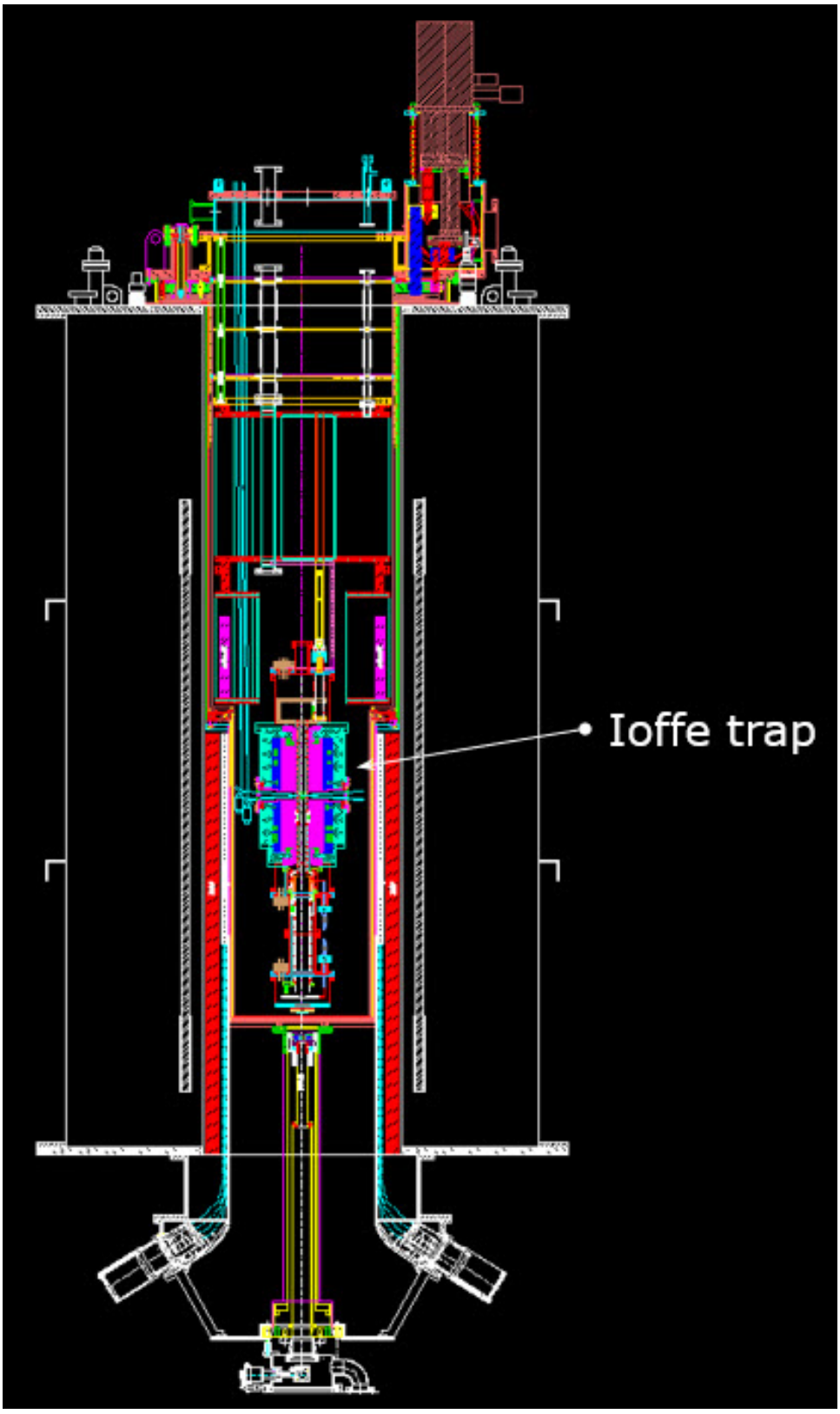

Figure 6.14: An overview of the second-generation ATRAP apparatus.

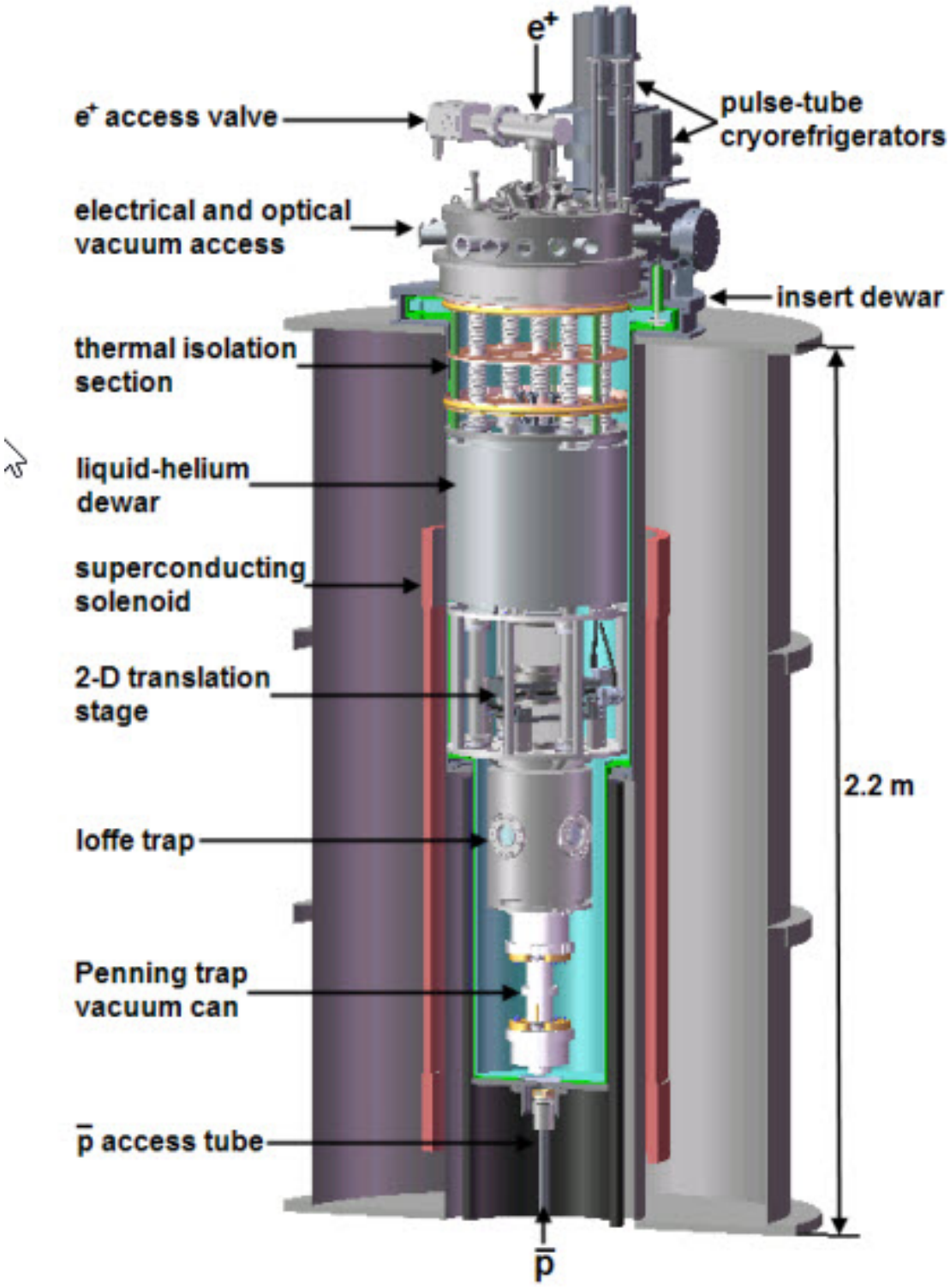

Figure 6.15: An overview of the second-generation ATRAP apparatus.

6.4.2 Particle Loading and Antihydrogen Production

The production rate of antihydrogen atoms formed in states strongly bound enough to survive the Penning trap fields and become trapped in a superimposed Ioffe trap is expected to be small. The rates increase with increased confinement of the antiatom constituents. The new apparatus is designed to allow for an increase in the rate of both antiproton capture and positron accumulation.

The additional space allows for a full redesign of the Penning trap, with dedicated stacks for antiproton capture, positron accumulation, and antihydrogen recombination. The proposed Penning trap is imaged in Fig. 6.16. The first-generation Penning trap is shown for comparison.

Design innovations include (1) the off-axis loading of positrons, allowing laser access on axis to the recombination region of the trap, (2) larger diameter electrodes for greater antiproton capture rates and greater particle storage capacity, and (3) a dedicated region for antihydrogen recombination with room for a superimposed neutral atom Ioffe trap.

A detail drawing of the proposed antiproton trapping region is shown in Fig. 6.17. The capture scheme remains the same as that described for the first-generation experiment in the previous section, and high voltage feedthroughs are shown for biasing the HV electrode and degrader to produce the deep capture well.

The electrodes are increased in diameter by a factor of 3. As discussed, and illustrated in Fig. 6.6, the antiproton trapping efficiency as a function of the high voltage well depth quickly saturates. This was explained by assuming that antiprotons emerging from the degrader with larger axial energies also have larger radial energy,

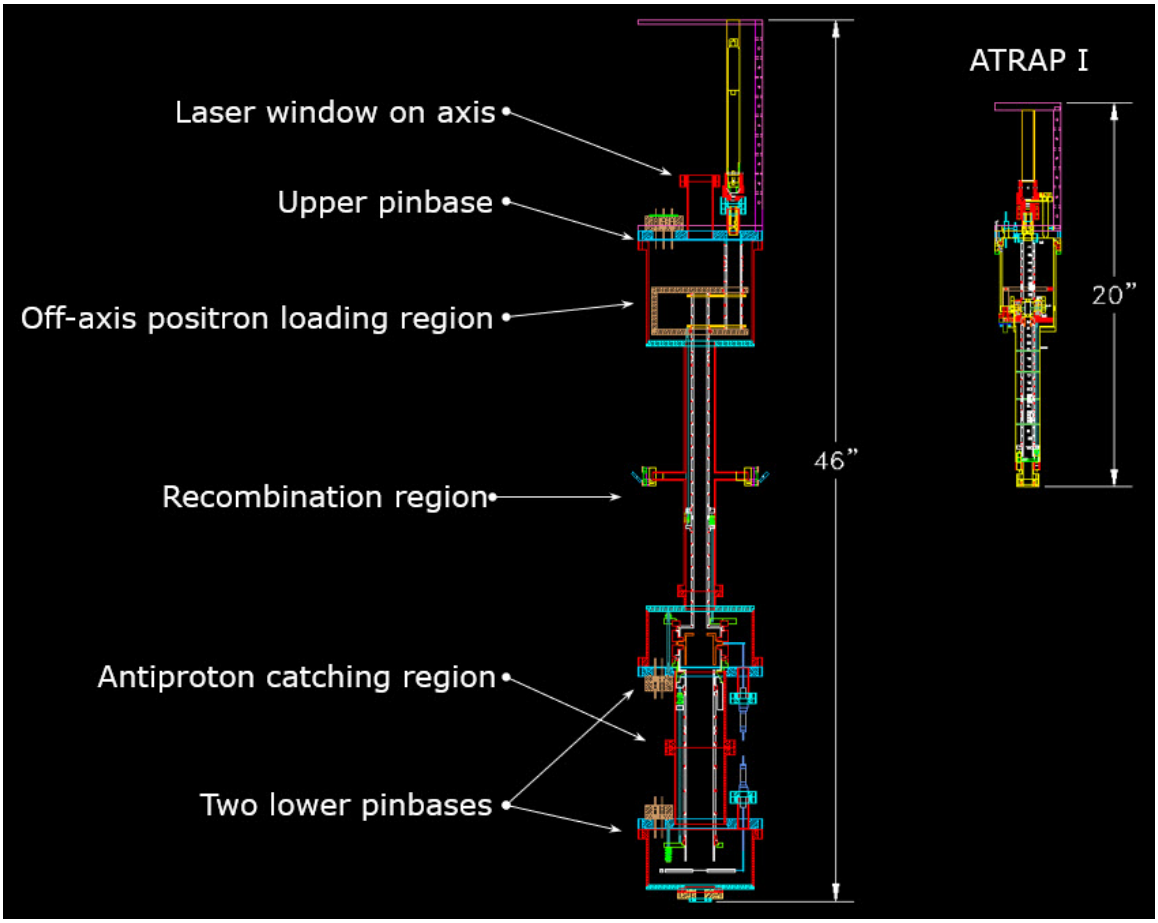

Figure 6.16: A comparison of the first and second generation Penning traps.

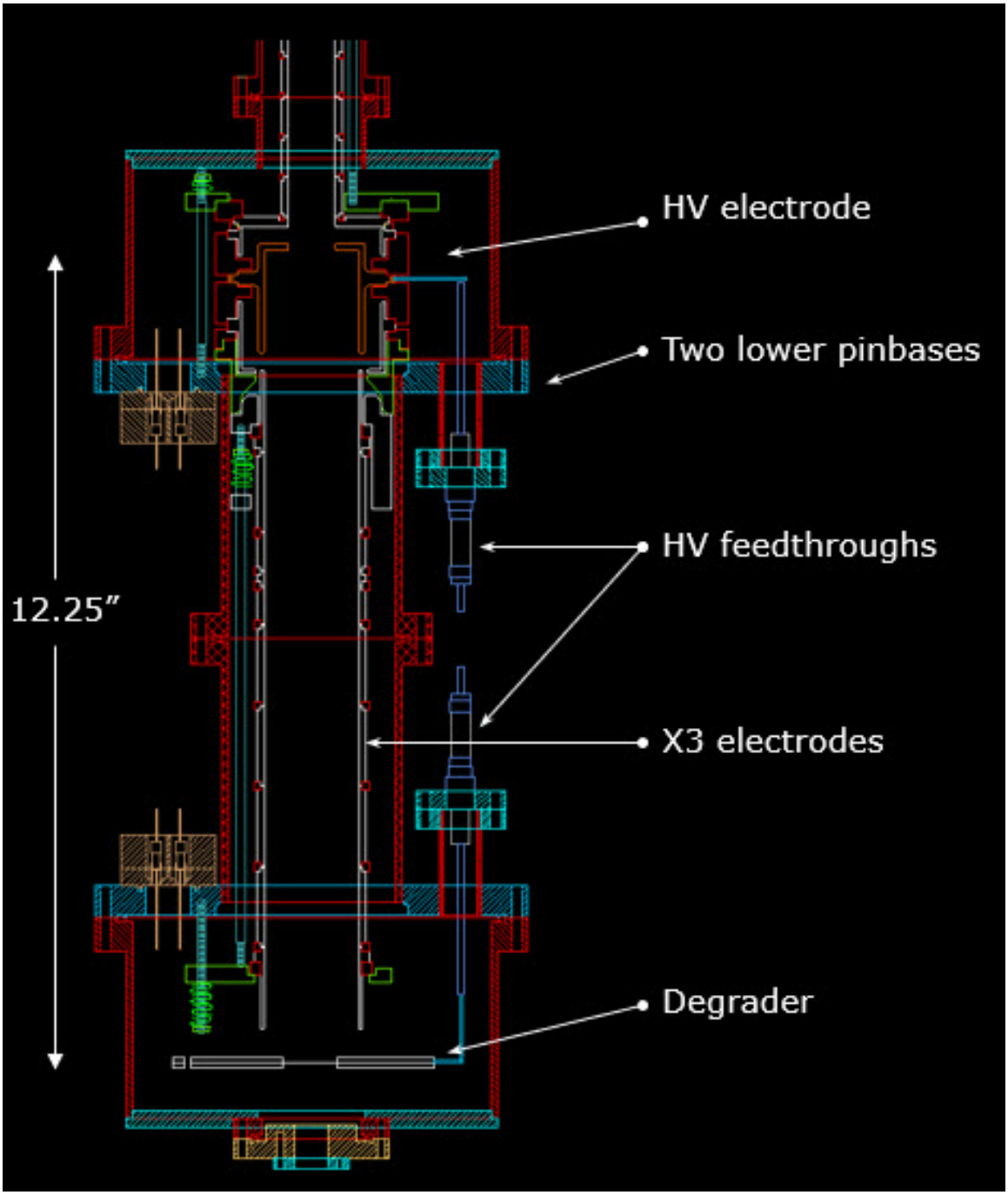

Figure 6.17: The proposed antiproton trapping region. Larger diameter electrodes allow for capture of antiprotons at larger cyclotron orbits. Larger volume allows for increased capacity.

and therefore a larger cyclotron radius in the magnetic field of the trap. Antiprotons at large enough radii will strike the electrodes and annihilate, eluding capture. At the same magnetic field strength, a trap with a larger electrode radius should achieve a trapping efficiency that remains linear up to higher trapping voltages. However, the larger diameter solenoid produces a 3 T field at maximum, compared to the 6 T field of the first-generation experiment, and is operated at ~ 1 T to allow for an adequate Ioffe trap depth, as will be discussed.

The choice of electrode diameter was driven by these tradeoffs. The parameters relevant to Ioffe trap design are shown as a function of the electrode radius in Fig. 6.18. The electrode radius is stated as relative to that of the first-generation electrodes. While trap volume increases rapidly with increased electrode radius, the trap depth sees a moderate rise and the cloud density quickly falls.

The advantage to having dedicated regions for antiproton capture, positron accumulation, and recombination is that we can choose different size electrodes for each region. The larger 3X electrodes (a radius 3 times that of previous trap) are chosen in the antiproton capture region so as to provide capture for antiprotons in larger cyclotron orbits and maintain capture efficiency. In subsequent designs, a field-boosting solenoid is added to the antiproton capture region to improve upon capture efficiency, as is seen in Fig. 6.15.

In the recombination region, 1.5X electrodes are chosen to mediate the tradeoff between Ioffe trap depth and density. The same size is chosen for the positron accummution region for simplicity. A detail drawing of the proposed positron loading region is shown in Fig. 6.19. The region, as drawn, describes positron accumulation

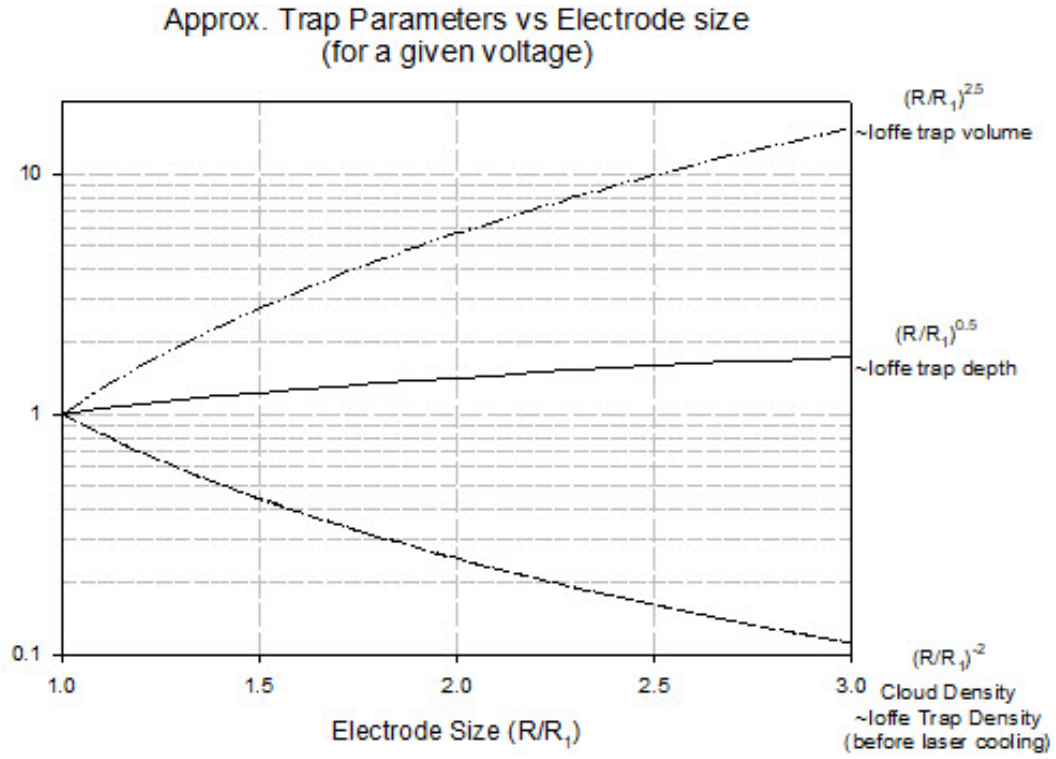

Figure 6.18: Trap parameters vary with electrode size.

by the field ionization of Rydberg positronium, the same method used in the previous experiment, as detailed in Section 6.3.4. The ^{2}2Na source is drawn, suspended above the off-axis accumulation stack. A transmission moderator at the top of the stack and a reflection moderator at the bottom facilitate the production of Rydberg positronium that is subsequently ionized, leaving slow positrons to be accumulated. Off-axis accumulation allows for laser access on axis for laser-cooling and spectroscopy studies of trapped antihydrogen atoms. A translation stage transports the accumulated positrons to the axis for transfer to the recombination region.

The proposed addition of a superconducting solenoid in this region is needed to maintain or improve upon the accumulation rate. The magnetic field dependence of the positron accumulation rate has been explored [78] and is shown in Fig. 6.20. The loading rate increases as the magnetic field strength to the power of 2.42. This is due to the stronger guidance of the positrons along magnetic field lines in the stronger magnetic field. The lower magnetic field in the new apparatus would lead to a diminished accumulation rate. Increased rates should be seen by boosting the field strength in the accumulation region.

While positron capture by the method of ionization of Rydberg positronium is attractive for its simplicity and compatibility with our experiment's ultrahigh-vacuum environment, its accumulation rate is low. Therefore, other methods for accumulating positrons with greater efficiency are explored.

An additional method for accumulating large numbers of positrons in a Penning trap is buffer gas loading, as used by the ATHENA collaboration, where collisions with a background gas are used to trap moderated positrons [89]. ATHENA, in

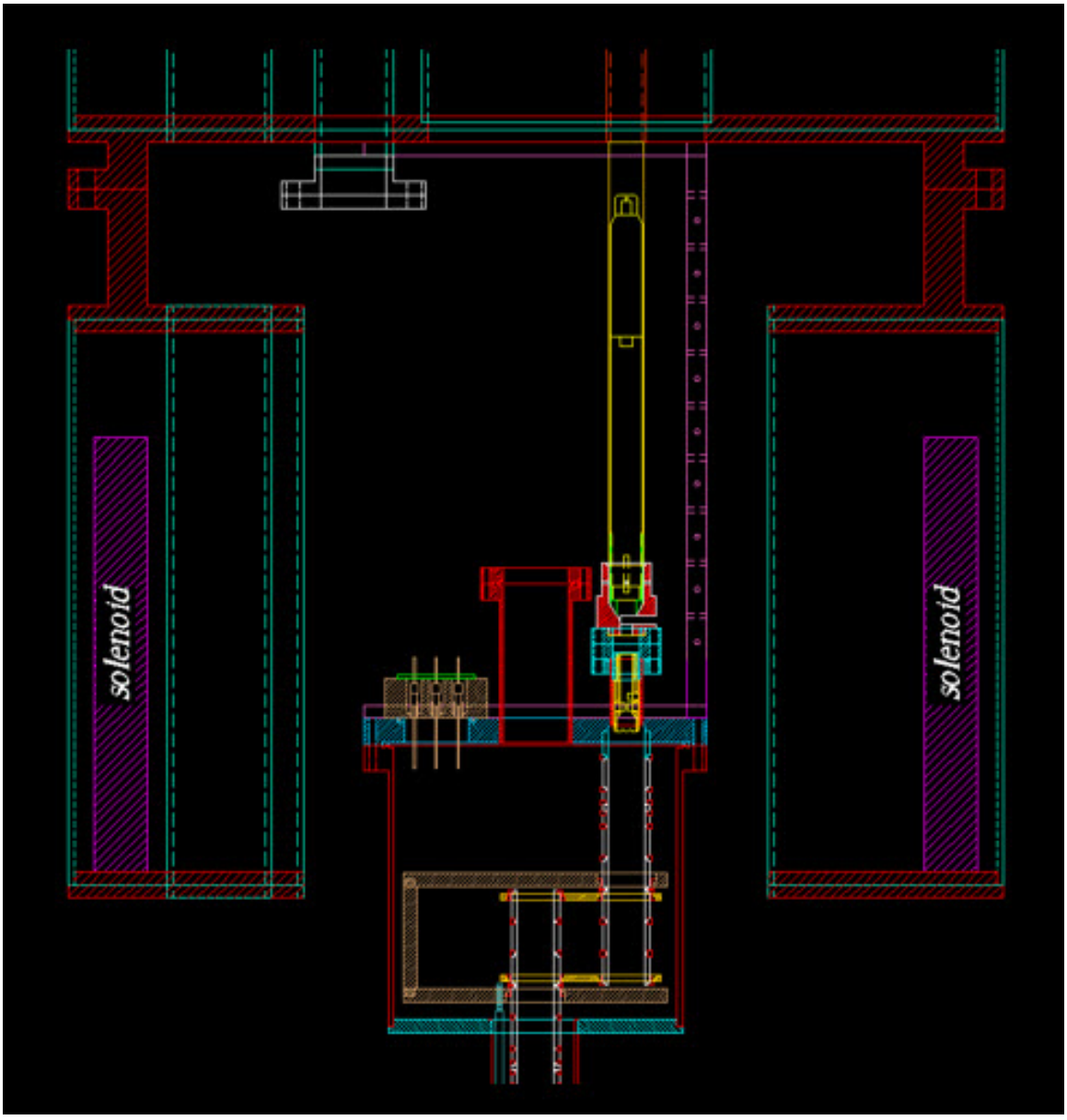

Figure 6.19: The positron loading region.

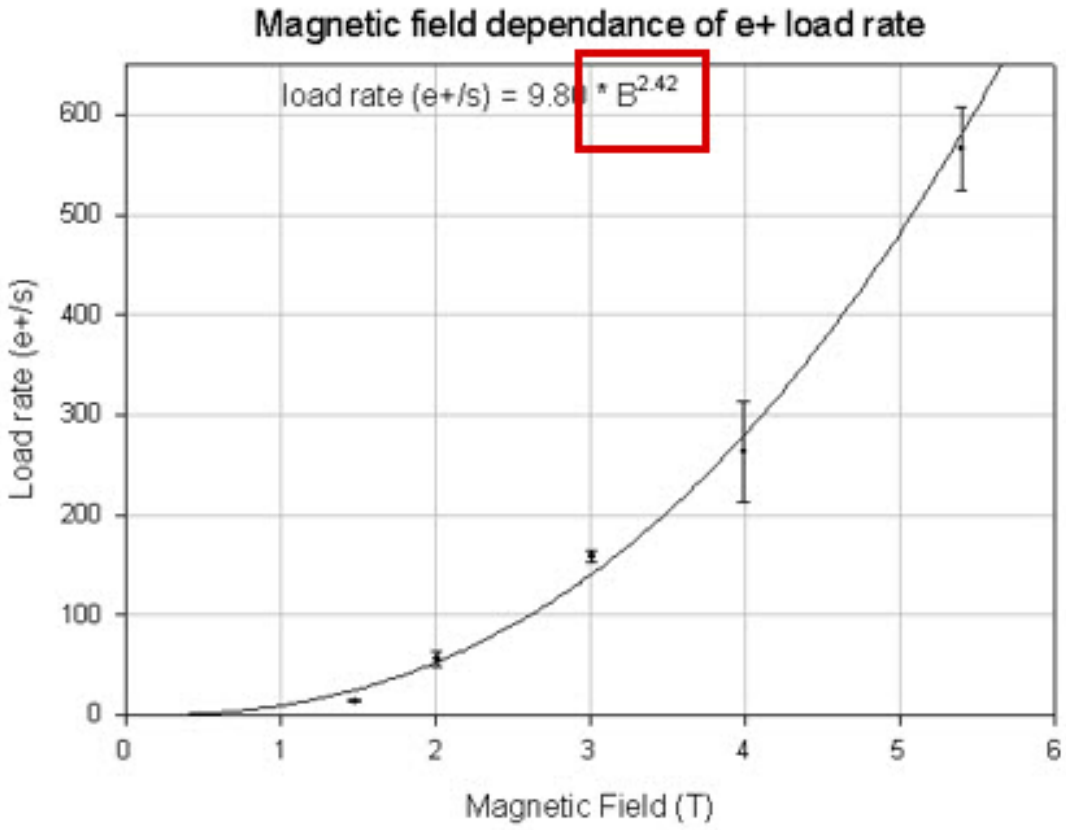

Figure 6.20: The magnetic field dependence of the positron accumulation rate.

their first report of antihydrogen production, states an accumulation of 150 million positrons in 5 minutes by this method [90]. However, the required buffer gas results in poor vacuum and a one hour antiproton lifetime. Implementing and improving on this scheme within the current apparatus, even with the new space allowed, presents a difficult design challenge, and the tradeoffs in vacuum and antiparticle lifetimes are unsatsifactory [78].

The current experiment solves this problem by accumulating the positrons in a separate apparatus and then transfering them to the combined Penning-Ioffe trap apparatus for antihydrogen production. The Positron Accumulator uses the buffer-gas cooling of moderated positrons from a 20 mCi source to accumulate positrons at the rate of 2.4×10^4 positrons per second per mCi [91]. As many as 4 billion positrons have been accumulated in the high-vacuum Penning-Ioffe trap apparatus, using electrons to cool the positrons during capture, a number 3 times larger than that achieved in any other trap.

6.4.3 Combined Penning-Ioffe Trap

An initial design of a neutral atom Ioffe trap was undertaken. Superimposed on the Penning trap recombination region, it allows for the neutral antihydrogen atoms produced to be trapped and stored for study. The Ioffe trap creates a magnetic quadrupole potential that confines the neutral atom by interaction with its magnetic moment [92, 93]. The potential energy of a neutral atom with magnetic moment $\vec{\mu}$ is given by $U = -\vec{\mu} \cdot \vec{B}$. The antiatoms formed are in highly-excited Rydberg states, as discussed, and so can have large magnetic moments. The trap depth to be maximized

is given in units of temperature for a hydrogen atom in the ground state as

$$U(T) = \frac{\mu_B}{k_B}\Delta B = (0.67K/T)\Delta B, \tag{6.2}$$

where k_B is the Boltzmann constant and μ_B is the Bohr magneton.

The magnetostatic quadrupole potential is created by the configuration of currents shown in Fig. 6.21. The currents in the four bars act to confine the atoms radially, while the the current loops, provide axial confinement. The inital design is shown in Fig. 6.22. The bar currents are given by four racetrack-shaped coils, shown in dark green on the purple form. The current loops are given by pinch coils, shown on the blue form. Following this work, a similar design was subsequently developed and studied in detail [94]. The design predicted a trap depth of 375 mK in the 1 T background field with 80 A in the pinch coils and 69 A in the racetrack coils. The first trapping of antihydrogen atoms with a quadrupole Ioffe trap was reported by our group in 2008 [94–96].

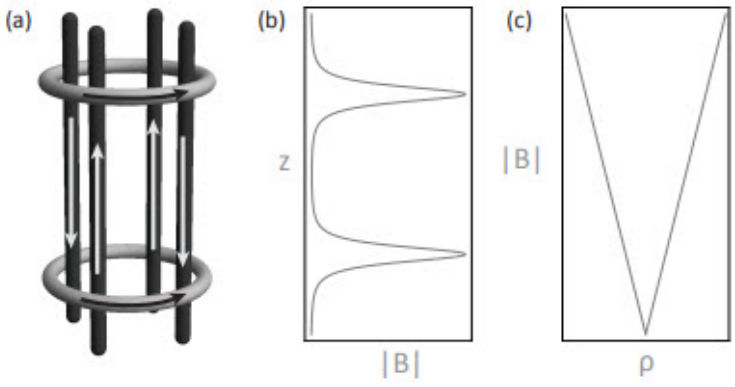

Figure 6.21: (a) The currents needed to form a quadrupole Ioffe trap. (b) The field magnetude on axis. (c) The radial field magnitude at the center of the trap.

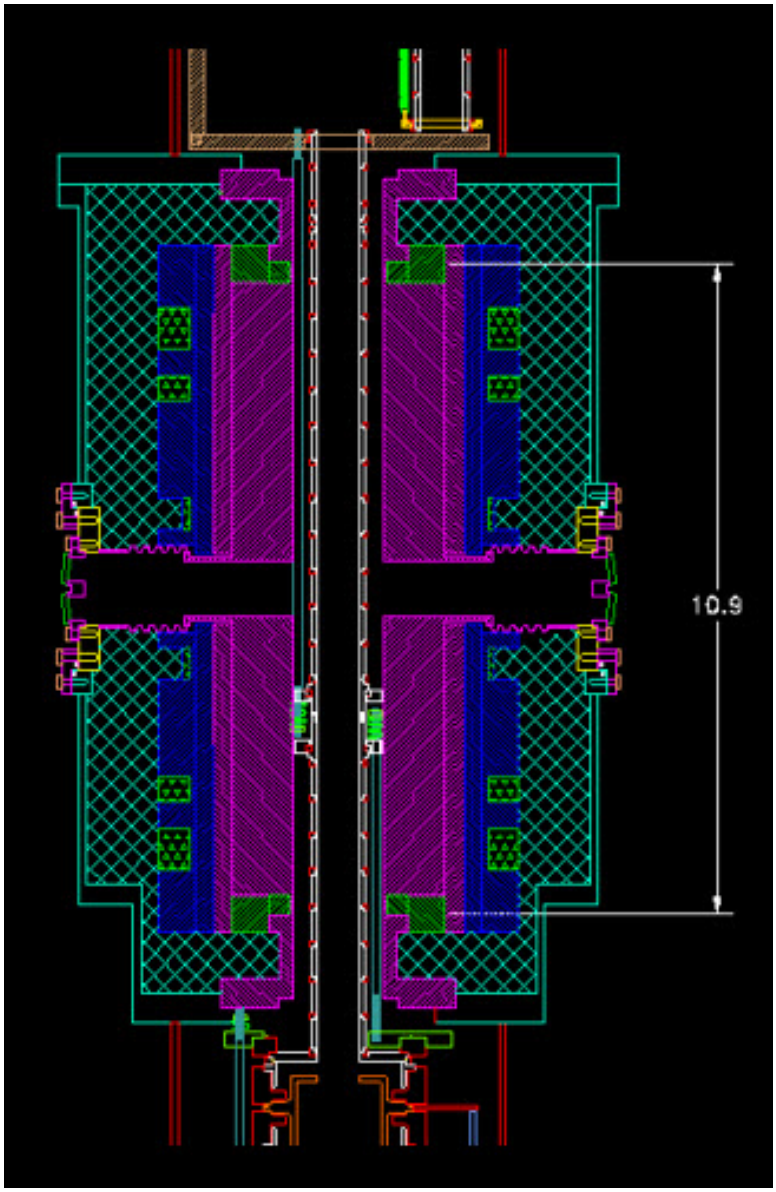

Figure 6.22: Initial design of Ioffe trap for neutral antihydrogen atom trapping.

6.4.4 Laser Access for Spectroscopy Studies

Important to future studies with trapped antihydrogen atoms is access to the recombination region of the combined Penning-Ioffe trap for lasers for cooling and spectroscopy studies. The room temperature hat with its laser access ports is imaged in the drawing of Fig. 6.23 and the photograph of Fig. 6.24. A central axis laser access port is shown as well as 8 outer ports for radial access to the recombination region. Tapped holes directly on the hat surface allow for mounting of related optics components. The hat was built and tested in house of stainless steel with commercially available Conflat and KF ports for electrical access to the cryogenic apparatus. The top flanges are build to be removable and interchangeable with additional flanges for maximum versatility.

Early assembly is shown in Fig. 6.25. Hat, isolation stage, and liquid helium dewar are shown. The completion and extension of these designs led to an apparatus that allowed for the first antihydrogen production within a Penning-Ioffe trap, reported in 2008 [95,96].

6.4.5 Conclusion

Studies with cold antimatter carried out with the first-generation ATRAP apparatus, demonstrated the capture of 5.3 MeV antiprotons from CERN's Antiproton Decelerator (AD) [12], the subsequent positron cooling of the captured antiprotons [13], and the production of cold antihydrogen atoms [14], reporting the first measured distribution of antihydrogen states [15]. In addition to supporting these efforts, I undertook the early design and development of a second-generation apparatus that

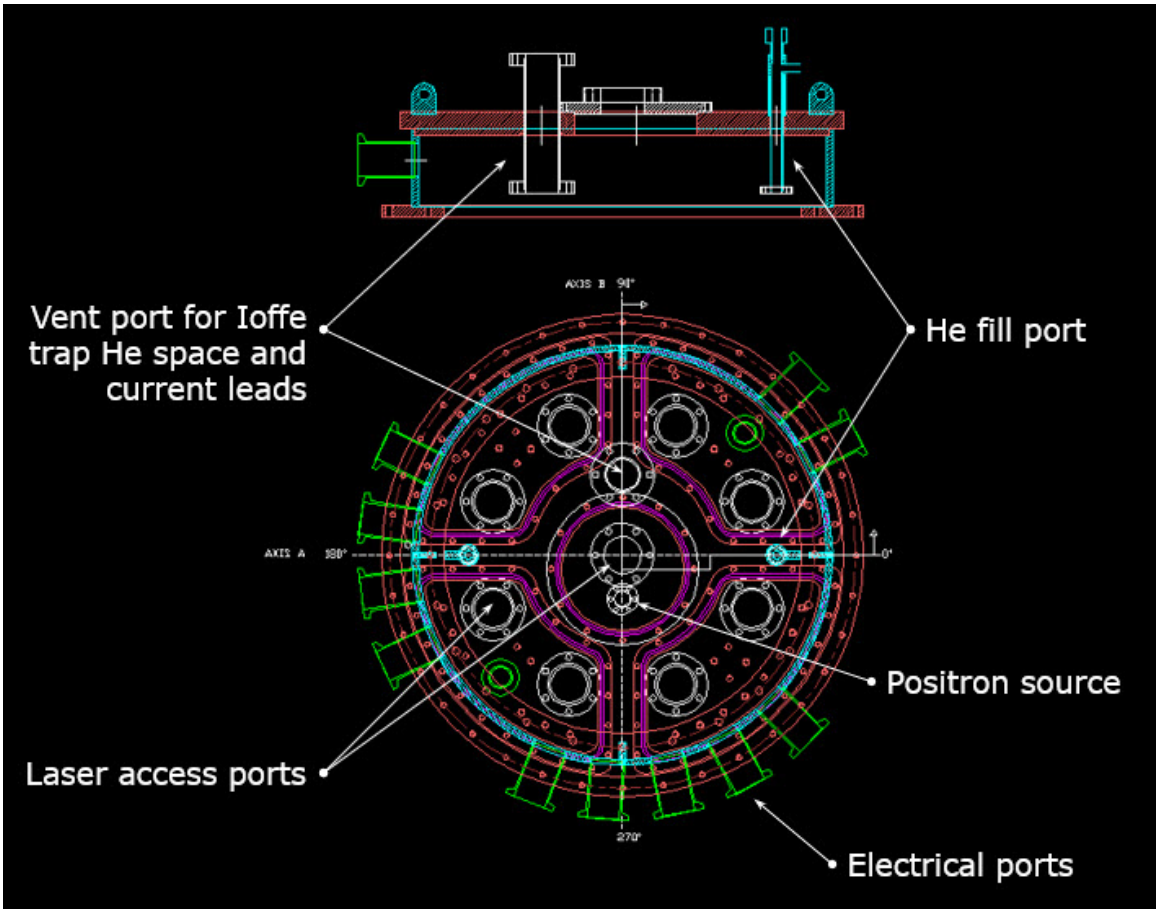

Figure 6.23: Drawing of the second-generation apparatus "hat." Ports are shown for laser access and electrical feedthrough. Top flanges are build to be removable and interchangeable with additional flanges for maximum versatility.

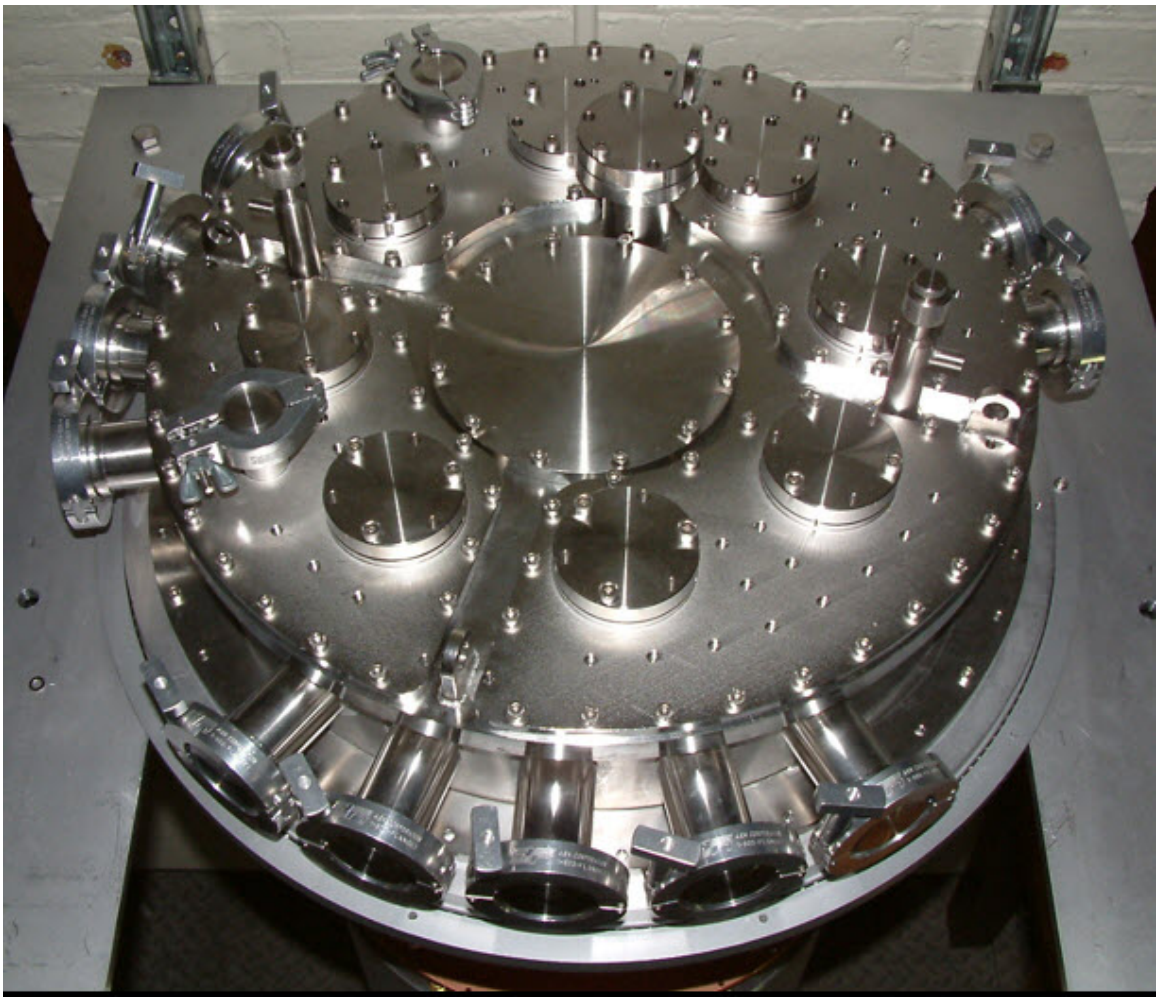

Figure 6.24: Photograph of second-generation apparatus "hat," with feedthrough and window access for electrical connections and lasers.

Figure 6.25: Early assembly of second-stage apparatus is shown.

would extend our capabilities and make possible the trapping and study of the neutral antihydrogen atoms produced. This chapter reports progress toward that goal. The completion and extension of these designs led to an apparatus that allowed for the first antihydrogen production within a Penning-Ioffe trap, reported in 2008 [94–96].

Bibliography

[1] G. Ciaramicoli, F. Galve, I. Marzoli, and P. Tombesi, Phys. Rev. A **72**, 042323 (2005).

[2] B. Odom, Ph.D. thesis, Harvard University, 2004.

[3] J. Goldman and G. Gabrielse, Phys. Rev. A **81**, 052335 (2010).

[4] S. Peil and G. Gabrielse, Phys. Rev. Lett. **83**, 1287 (1999).

[5] S. Stahl, F. Galve, J. Alonso, S. Djekic, W. Quint, T. Valenzuela, J. Verdú, M. Vogel, and G. Werth, The European Physical Journal D - Atomic, Molecular, Optical and Plasma Physics **32**, 139 (2005).

[6] I Marzoli, P Tombesi, G Ciaramicoli, G Werth, P Bushev, S Stahl, F Schmidt-Kaler, M Hellwig, C Henkel, G Marx, I Jex, E Stachowska, G Szawiola, and A Walaszyk, Journal of Physics B: Atomic, Molecular and Optical Physics **42**, 154010 (2009).

[7] P Bushev, Stefan Stahl, Riccardo Natali, G Marx, Ewa Stachowska, G Werth, M Hellwig, and F Schmidt-Kaler, European Physical Journal D **50**, 97 (2008).

[8] J. Goldman and G. Gabrielse, Hyperfine Interact **199**, 279 (2011).

[9] J. Goldman, Ph.D. thesis, Harvard University, 2011.

[10] G. Gabrielse, J.N. Tan, N.S. Bowden, P. Oxley, C.H. Storry, M. Wessels, A. Speck, J. Estrada, P. Yesley, D. Grzonka, W. Oelert, G. Schepers, T. Sefzick, and J. Walz, in *Proceedings of the Second Meeting on CPT and Lorentz Symmetry*, edited by V. Alan Kostelecky (World Scientific Publishing Co Pte. Ltd., ADDRESS, 2002).

[11] G. Gabrielse, Hyperfine Interactions **44**, 349 (1988).

[12] G. Gabrielse, N.S. Bowden, P. Oxley, A. Speck, C.H. Storry, J.N. Tan, M. Wessels, D. Grzonka, W. Oelert, G. Schepers, T. Sefzick, J. Walz, H. Pittner, T.W. Hansch, and E.A. Hessels, Phys. Lett. B. **548**, 140 (2002).

[13] G. Gabrielse, J. Estrada, J.N. Tan, P. Yesley, N.S. Bowden, P. Oxley, T. Roach, C.H. Storry, M. Wessels, J. Tan, D. Grzonka, W. Oelert, G. Schepers, T. Sefzick, W. Bruenlich, M. Carngelli, H. Fuhrmann, R. King, R. Ursin, H. Zmeskal, H. Kalinowsky, and C. Wesdorp, Phys. Lett. B. **507**, 1 (2001).

[14] G. Gabrielse, N.S. Bowden, P. Oxley, A. Speck, C.H. Storry, J.N. Tan, M. Wessels, D. Grzonka, W. Oelert, G. Schepers, T. Sefzick, J. Walz, H. Pittner, T.W. Hansch, and E.A. Hessels, Phys. Rev. Lett. **89**, 213401 (2002).

[15] G. Gabrielse, N.S. Bowden, P. Oxley, A. Speck, C.H. Storry, J.N. Tan, M. Wessels, D. Grzonka, W. Oelert, G. Schepers, T. Sefzick, J. Walz, H. Pittner, T.W. Hansch, and E.A. Hessels, Phys. Rev. Lett. **89**, 233401 (2002).

[16] B. D'Urso, Ph.D. thesis, Harvard University, 2003.

[17] Paul Benioff, Journal of Statistical Physics **22**, 563 (1980).

[18] Richard P. Feynman, International Journal of Theoretical Physics **21**, 467 (1982).

[19] D. Deutsch, Proc. Royal Soc. London **A400**, 97 (1985).

[20] D. Deutsch, Proc. Royal Soc. London **A425**, 73 (1989).

[21] P. Shor, SIAM Review **41**, 303 (1999).

[22] I. M. Georgescu, S. Ashhab, and Franco Nori, Rev. Mod. Phys. **86**, 153 (2014).

[23] David P. Divincenzo, Fortschritte der Physik **48**, 771 (2000).

[24] Iulia Buluta, Sahel Ashhab, and Franco Nori, Reports on Progress in Physics **74**, (2011).

[25] T. D. Ladd, F. Jelezko, R. Laflamme, Y. Nakamura, C. Monroe, and J. L. O'brien, Nature **464**, (2010).

[26] J.C.F Matthews, A Politi, A.B Stefanov, and J.L O'Brien, Nature Photonics **3**, 346 (2009).

[27] Stefan Kuhr, National Science Review **3**, 170 (2016).

[28] J Benhelm, G. Kirchmair, C.F. Roos, and R. Blatt, Nature Physics **4**, 463 (2008).

[29] C A Ryan, M Laforest, and R Laflamme, New Journal of Physics **11**, 013034 (2009).

[30] Chao Song, Kai Xu, Wuxin Liu, Chui-ping Yang, Shi-Biao Zheng, Hui Deng, Qiwei Xie, Keqiang Huang, Qiujiang Guo, Libo Zhang, Pengfei Zhang, Da Xu, Dongning Zheng, Xiaobo Zhu, H. Wang, Y.-A. Chen, C.-Y. Lu, Siyuan Han, and Jian-Wei Pan, Phys. Rev. Lett. **119**, 180511 (2017).

[31] Zhiguang Yan, Yu-Ran Zhang, Ming Gong, Yulin Wu, Yarui Zheng, Shaowei Li, Can Wang, Futian Liang, Jin Lin, Yu Xu, Cheng Guo, Lihua Sun, Cheng-Zhi Peng, Keyu Xia, Hui Deng, Hao Rong, J. Q. You, Franco Nori, Heng Fan, Xiaobo Zhu, and Jian-Wei Pan, Science **364**, 753 (2019).

[32] David T. Press, Thaddeus D. Ladd, Bingyang Zhang, and Yoshihisa Yamamoto, Nature **456**, 218 (2008).

[33] P. Neumann, N. Mizuochi, F. Rempp, P. Hemmer, H. Watanabe, S. Yamasaki, V. Jacques, T. Gaebel, F. Jelezko, and J. Wrachtrup, Science **320**, 1326 (2008).

[34] Hannes Bernien, Sylvain Schwartz, Alexander Keesling, Harry Levine, Ahmed Omran, Hannes Pichler, Soonwon Choi, Alexander S. Zibrov, Manuel Endres, Markus Greiner, Vladan Vuletić, and Mikhail D. Lukin, Nature **551**, (2017).

[35] Thomas Monz, Philipp Schindler, Julio T. Barreiro, Michael Chwalla, Daniel Nigg, William A. Coish, Maximilian Harlander, Wolfgang Hänsel, Markus Hennrich, and Rainer Blatt, Phys. Rev. Lett. **106**, 130506 (2011).

[36] R. Islam, C. Senko, W. C. Campbell, S. Korenblit, J. Smith, A. Lee, E. E. Edwards, C.-C. J. Wang, J. K. Freericks, and C. Monroe, Science **340**, 583 (2013).

[37] Stefano Mancini, Ana M. Martins, and Paolo Tombesi, Phys. Rev. A **61**, 012303 (1999).

[38] G. Ciaramicoli, I. Marzoli, and P. Tombesi, Phys. Rev. A **63**, 052307 (2001).

[39] G. Ciaramicoli, I. Marzoli, and P. Tombesi, Phys. Rev. Lett. **91**, 017901 (2003).

[40] G. Ciaramicoli, I. Marzoli, and P. Tombesi, Phys. Rev. A **70**, 032301 (2004).

[41] G. CIARAMICOLI, I. MARZOLI, and P. TOMBESI, International Journal of Modern Physics B **20**, 1699 (2006).

[42] G. Gabrielse and F.C. MacKintosh, Int. J. Mass Spectroscopy and Ion Processes **57**, 1 (1984).

[43] D. Hanneke, S. Fogwell, and G. Gabrielse, Phys. Rev. Lett. **100**, 120801 (2008).

[44] L. Lamata, D. Porras, J. I. Cirac, J. Goldman, and G. Gabrielse, Phys. Rev. A **81**, 022301 (2010).

[45] D. Hanneke, Ph.D. thesis, Harvard University, 2007.

[46] F. Galve, P. Fernández, and G. Werth, The European Physical Journal D - Atomic, Molecular, Optical and Plasma Physics **40**, 201 (2006).

[47] Fernando Galve and Guenter Werth, Hyperfine Interactions **174**, 41 (2007).

[48] L.S. Brown and G. Gabrielse, Reviews of Modern Physics **58**, 233 (1986).

[49] G. Gabrielse, Phys. Rev. A **27**, 2277 (1983).

[50] G. Gabrielse, Phys. Rev. A **29**, 462 (1984).

[51] J. Tan and G. Gabrielse, Appl. Phys. Lett. **55**, 2144 (1989).

[52] H. Dehmelt, R.S. Van Dyck, P.B. Schwinberg, and G. Gabrielse, Bull. Am. Phys. Soc. **24**, 675 (1979).

[53] G. Gabrielse, L. haarsma, and S.L. Rolston, Intl. J. of Mass Spec. and Ion Proc. **88**, 319 (1989).

[54] G. Gabrielse, X. Fei, K. Helmerson, S.L. Rolston, R.L. Tjoelker, T.A. Trainor, H. Kalinowsky, J. Haas, and W. Kells, Phys. Rev. Lett. **57**, 2504 (1986).

[55] J. DiSciacca, M. Marshall, K. Marable, G. Gabrielse, S. Ettenauer, E. Tardiff, R. Kalra, D.W. Fitzakerley, M.C. George, E.A. Hessels, C.H. Story, M. Weel, D. Grzonka, W. Oelert, and T. Sefzick, Phys. Rev. Lett. **110**, 130801 (2013).

[56] Jaroslaw Labaziewicz, Yufei Ge, David R. Leibrandt, Shannon X. Wang, Ruth Shewmon, and Isaac L. Chuang, Phys. Rev. Lett. **101**, 180602 (2008).

[57] L. Deslauriers, S. Olmschenk, D. Stick, W. K. Hensinger, J. Sterk, and C. Monroe, Physical Review Letters **97**, (2006).

[58] D.J. Wineland, Phil Ekstrom, and H G. Dehmelt, Physical Review Letters **31**, 1279 (1973).

[59] T.W. Darling J.B. Camp and R.E. Brown, J. Appl. Phys. **69**, 7126 (1991).

[60] Sunchana P. Pucic, IEEE Instrumentation and Measurement Technology Conference 114 (1993).

[61] J.W. Ekin, *Experimental Techniques for Low-Temperature Measurements* (Oxford University Press, Oxford, 2006).

[62] Wei Tse Chang, Ing-Shouh Hwang, Mu-Tung Chang, Chun-Yueh Lin, Wei-Hao Hsu, and Jin-Long Hou, The Review of scientific instruments **83**, 083704 (2012).

[63] E. Novitski, Ph.D. thesis, Harvard University, 2017.

[64] Fei X. Orozco L.A. Tjoelker R.L. Haas J. Kalinowsky H. Trainor T.A. Gabrielse, G. and W. Kells, Phys. Rev. Lett. **65**, 1317 (1990).

[65] G Gabrielse and J Tan, Journal of Applied Physics **63**, 5143 (1988).

[66] M. Fogwell Hoogerheide, Ph.D. thesis, Harvard University, 2013.

[67] W.W. Macalpine and R.O. Schildknecht, Proc. IRE **47**, 2099 (1959).

[68] D J. Wineland and H G. Dehmelt, Journal of Applied Physics **46**, 919 (1975).

[69] J. Tan, Ph.D. thesis, Harvard University, 2007.

[70] L. Haarsma, Ph.D. thesis, Harvard University, 1994.

[71] J.B. Camp, T.W. Darling, and R.E. Brown, J. Appl. Phys. **69**, 7126 (1991).

[72] G. Gabrielse, X. Fei, K. Helmerson, S.L. Rolston, R. Tjoelker, and T.A. Trainor, Phys. Rev. Lett. **57**, 2504 (1986).

[73] G. Gabrielse, X. Fei, L.A. Orozco, R. Tjoelker, J. Haas, H. Kalinowsky, T.A. Trainor, and W. Kells, Phys. Rev. Lett. **63**, 1360 (1989).

[74] G. Gabrielse, A. Khabbaz, D.S. Hall, C. Heimann, H. Kalinowsky, and W. Jhe, Phys. Rev. Lett. **82**, 3198 (1999).

[75] Christian G. Parthey, Arthur Matveev, Janis Alnis, Birgitta Bernhardt, Axel Beyer, Ronald Holzwarth, Aliaksei Maistrou, Randolf Pohl, Katharina Predehl, Thomas Udem, Tobias Wilken, Nikolai Kolachevsky, Michel Abgrall, Daniele Rovera, Christophe Salomon, Philippe Laurent, and Theodor W. Hänsch, Phys. Rev. Lett. **107**, 203001 (2011).

[76] R. Kalra, Ph.D. thesis, Harvard University, 2014.

[77] N. Beverini, V. Lagomarsino, G. Manuzio, F. Scuri, and G. Torelli, Hyperfine Interactions **44**, 357 (1989).

[78] N. Bowden, Ph.D. thesis, Harvard University, 2003.

[79] P. Oxley, Ph.D. thesis, Harvard University, 2003.

[80] J. Estrada, Ph.D. thesis, Massachusetts Institute of Technology, 2002.

[81] P. Yesley, Ph.D. thesis, Harvard University, 2001.

[82] H. Stelzer, Nuclear Instruments and Methods **133**, 409 (1976).

[83] S.L. Rolston and G. Gabrielse, Hyperfine Interactions **44**, 233 (1989).

[84] G. Gabrielse, D. S. Hall, T. Roach, P. Yesley, A. Khabbaz, J. Estrada, C. Heimann, and H. Kalinowsky, Physics Letters B **455**, 311 (1999).

[85] J. Estrada, T. Roach, J. N. Tan, P. Yesley, and G. Gabrielse, Phys. Rev. Lett. **84**, 859 (2000).

[86] R. G. Musket, W. McLean, C. A. Colmenares, D. M. Makowiecki, and W. J. Siekhaus, Applied Surface Science **10**, 143 (1982).

[87] G. Gabrielse, S. L. Rolston, L. Haarsma, and W. Kells, Physics Letters, Section A: General, Atomic and Solid State Physics **129**, 38 (1988).

[88] P. O. Fedichev, Physics Letters A **226**, 289 (1997).

[89] D. P. van der Werf, L. V. Jørgensen, T. L. Watson, M. Charlton, M. J. T. Collier, M. Doser, and R. Funakoshi, Applied Surface Science **194**, 312 (2002).

[90] C. et al. Amoretti, Nature **419**, 456 (2002).

[91] D. W. Fitzakerley, M. C. George, E. A. Hessels, T. D G Skinner, C. H. Storry, M. Weel, G. Gabrielse, C. D. Hamley, N. Jones, K. Marable, E. Tardiff, D. Grzonka, W. Oelert, and M. Zielinski, Journal of Physics B: Atomic, Molecular and Optical Physics **49**, (2016).

[92] Alan L. Migdall, John V. Prodan, William D. Phillips, Thomas H. Bergeman, and Harold J. Metcalf, Phys. Rev. Lett. **54**, 2596 (1985).

[93] T. Bergeman, Gidon Erez, and Harold J. Metcalf, Phys. Rev. A **35**, 1535 (1987).

[94] P. Larochelle, Ph.D. thesis, Harvard University, 2009.

[95] G. Gabrielse, P. Larochelle, D. Le Sage, B. Levitt, W. S. Kolthammer, R. McConnell, P. Richerme, J. Wrubel, A. Speck, M. C. George, D. Grzonka, W. Oelert, T. Sefzick, Z. Zhang, A. Carew, D. Comeau, E. A. Hessels, C. H. Storry, M. Weel, and J. Walz, Phys. Rev. Lett. **100**, 113001 (2008).

[96] D. Le Sage, Ph.D. thesis, Harvard University, 2008.